Eduardo García Rivera

UPC **CTTC**

Modelling and Experimental Validation of Water Vapor Absorption by Falling Films of LiBr Aqueous Solution Under Wave Regimes Conditions and Presence of Non-Absorbable Gases

DOCTORAL THESIS

Centro Tecnológico de Transferencia de Calor
Departamento de Máquinas y Motores Térmicos
Universidad Politécnica de Catalunya

Eduardo García Rivera
Doctoral Thesis

UPC – Marzo, 2015

Modelling and Experimental Validation of Water Vapor Absorption by Falling Films of LiBr Aqueous Solution Under Wave Regimes Conditions and Presence of Non-Absorbable Gases

Eduardo García Rivera

TESIS DOCTORAL

presentada al

Departamento de Máquinas y Motores Térmicos
E.T.S.E.I.A.T.
Universidad Politécnica de Catalunya

para la obtención del grado de

Doctor Ingeniero Industrial

Terrassa, Marzo, 2015

Modelling and Experimental Validation of Water Vapor Absorption by Falling Films of LiBr Aqueous Solution Under Wave Regimes Conditions and Presence of Non-Absorbable Gases

Eduardo García Rivera

Directores de la Tesis

Dr. Jesús Castro González
Dr. Assensi Oliva Llena

Tribunal Calificador

Dr. JOSÉ MANUEL PINAZO OJER
Universidad Politécnica de Valencia

Dr. CARLES OLIET CASASAYAS
Universidad Politécnica de Cataluña

Dr. MARIA MANUELA PRIETO GONZÁLEZ
Escuela Politécnica de Ingeniería de Gijón

Modelling and Experimental Validation of Water Vapor Absorption by Falling Films of LiBr Aqueous Solution Under Wave Regimes Conditions and Presence of Non-Absorbable Gases

Contents

A Fátima Elisa, mi esposa y entrañable compañera.
Gracias por tu paciencia, comprensión y amor incondicional.
Me harían falta esta y muchas otras vidas para agradecerte
por todo el amor que me has brindado..... Te amo.

A mis padres que con su amor y enseñanza me
educaron en la virtud para ser un hombre de bien

Agradecimientos

Mi más sincero agradecimiento a las siguientes personas:

Al Doctor Jesús Castro, director de esta Tesis, y a quien considero un referente en el campo de la refrigeración por absorción. Su orientación, rigor e intuición científica fueron determinantes para lograr los objetivos de este trabajo.

Al Doctor Assensi Oliva, que siempre me brindo el apoyo necesario para desarrollar mis funciones durante mi doctorado.

A Manuel Ordoño, por todo su apoyo referente al diseño, construcción y puesta en marcha de la unidad experimental.

A Joan Farnós, compañero y colega en el campo de la refrigeración por absorción. Siempre entusiasta y con buen humor fue una agradable compañía durante las largas horas de trabajo experimental.

Al Doctor Carlos D. Pérez y al Doctor Carles Oliet, por sus valiosos comentarios y observaciones que me ayudaron a mejorar este manuscrito.

Resumen

La situación energética global presenta varias dificultades para la comunidad científica y la población mundial en general. Los principales aspectos a destacar son los siguientes: i) el aumento del precio de la energía (principalmente es obtenida de los combustibles fósiles); ii) la emisiónes de gases de efecto invernadero; iii) la emisión de refrigerantes halogenados existentes en los equipos de refrigeración y bombas de calor. Los factores mencionados anteriormente contribuyen al calentamiento global y el deterioro de la capa de ozono.

Por estas razones es necesario buscar alternativas para la reduccion del gasto energetico y sus consecuentes emisiones de gases. En el caso concreto de la producción de frío, se ha observado un aumento en la demanda de aire acondicionado, sobre todo en países desarrollados, lo cual genera problemas importantes en las horas de máxima sobrecarga, aumentando el coste de la electricidad y perturbando el balance energético de dichos países (2002/91/CE).

Es por eso que la refrigeración por absorción asistida con energía solar ha ido adquiriendo cada vez un mayor interés y desarrollo desde un punto de vista tanto económico como ambiental. Aunque en la actualidad existen una gran variedad de sistemas de absorción en el mercado, la gran mayoría son de gran capacidad. En realidad existe poco desarrollo relacionado a los sistemas compactos o de media capacidad. Los sistemas de pequeña capacidad ofrecen algunas dificultades (enfriamiento por aire, compacidad, etc) que sólo pueden ser afrontadas a un bajo coste con las herramientas de diseño adecuadas.

El diseño y dimensionamiento de un sistema de refrigeración está condicionado en mayor medida por el absorbedor, es por eso que este trabajo se centra especialmente en el proceso de absorción en película descendente con la mezcla $LiBr - H_2O$ en bancos de tubos verticales, que es la configuración mas común en absorbedores compactos enfriados por aire. Actualmente existe poca literatura especializada para el desarrollo de herramientas de diseño y modelos matemáticos adecuados que ayuden a la descripción de la fenomenología de absorción de película descendente. Por estas razones expuestas, a continuación enumeramos los objetivos de esta tesis:

1. El estudio de los distintos mecanismos que participan durante la absorción de vapor de H_2O en la películas descendente verticales usando la mezcla $LiBr - H_2O$: i) transferencia simultanea de calor y masa; ii) regimen ondulado en la superficie libre de la pelicula; iii) influencia de gases incondensables en el desempeño del absorbedor.

2. El desarrollo de herramientas numéricas de cálculo rápido que describan los más preciso posible (dentro de sus limitantes) el comportamiento de la absorción de en películas descendentes bajo las características descritas en el punto anterior.

3. El desarrollo de una unidad experimental lo suficientemente versátil que nos permita evaluar el desempeño del proceso de absorción a diferentes condiciones de presión, regímenes de flujo, temperatura, concentración, etc. De esta forma se obtiene un amplio rango de datos experimentales.

4. La validación de los modelos matemáticos a través de la comparación con los datos experimentales obtenidos en el punto anterior.

Abstract

The global energy situation presents several challenges to the global scientific community and the world population. The main points to highlight are the following: i) the increase of the price of energy (which mainly is obtained from fossil fuels); ii) the emission of greenhouse gases; iii) the emission of halogenated refrigerants that are used in cooling systems and heat pumps. The facts mentioned below contribute to global warming and the deterioration of the ozone layer.

For these reasons it is necessary to find alternatives for the reduction of energy expenditure and its consequent gas emissions. In the specific case of cooling production, there has been an increase in demand for air conditioning, mainly in the developed countries. This fact creates important problems in the peak load times which causes the increasing in the cost of electricity and also disrupting the energy balance in those countries.

That is why solar absorption refrigeration driven by solar energy has been acquiring more interest and development from a standpoint of both economic and environmental. Although, nowadays there are many absorption systems in the market, the vast majority are large capacity systems. Actually there is little development related to compact or medium capacity systems. Small capacity systems offer some difficulties (air cooling, compactness, etc) that can only be faced in a low cost with suitable tools of design.

The design and dimensioning of a cooling system is further conditioned by the absorber, that is why this work is particularly focused on the absorption process in vertical falling film absorbers with the mixture $LiBr - H_2O$. Vertical absorbers is the more appropriate configuration for the air-cooled absorption machines. Currently there is little literature related of the development of design tools and appropriate mathematical models that provides successful description of the phenomenology of vertical absorption in falling film. For such reason, the objectives of this thesis are listed below:

1. The study of the different mechanisms involved during vapor absorption of H_2O in the vertical falling films using $LiBr - H_2O$: i) simultaneous heat and mass transfer; ii) wavy regime at the free surface of the film; iii) the influence of non-absorbable gases in the performance of the absorber.

2. The development of quick calculation numerical tools which describe the most accurate possible (within their limitations) the behavior of absorption in falling films with the characteristics described in above.

3. The development of an experimental unit versatile enough to allow us to evaluate the performance absorption process at different conditions of pressure, flow

rates, temperature, concentration, etc. In this way it is possible to obtain a wide range of experimental data.

4. The validation of mathematical models by comparison with experimental data obtained in the above point.

Chapter 1

Introduction

1.1 Background

The global energy situation exhibits some challenges: the increasing scarcity of energy resources, green house effect caused by CO_2 emissions, ozone depletion etc. The demand of cooling is increasing rapidly over the world, specially in developed countries. Furthermore, this growth causes an important rise in electricity demand, being the peaks reached in hot summer days. The consequences of such peak demands are a dangerous instability of electricity grids [1]. Other aspect refers to the global environmental situation, such as the so called greenhouse effect caused by CO_2 emission from the combustion of fossil fuels. Since the beginning of the last century, average global temperature has risen by about $0.6K$ according to the Intergovernmental Panel on Climate Change (IPCC) [2]. It is also warned that the temperature may further increase by $1.4 - 4.5K$ until 2100 [2]. Due to all this circumstances and the unsustainable energetic situation, it is necessary to call for a sustainable development of energy production.

In the case technology of heating and cooling production, it represents the 49% of the energy consumption [3]. To terms to the cooling production, the vapor compression cooling systems are the most popular way and dominates the market sector. However, the absorption technology has received special attention because it can employ natural refrigerants (water, ammonia, methanol, etc.), and can be thermally driven by wasted heat, solar or geothermal energy, and hence support to reduce the fossil fuel consumption. For this reason, the absorption systems are seen as one of the most convenient ways of reducing the emissions of greenhouse gases such as CO_2.

Absorption refrigeration is a thermal driven technology, the main heat powered sources are solar energy and wasted heat. The use of thermally-driven operated refrigeration systems help to reduce problems related to global environmental (reduction of CO_2 emissions).

According to the temperature range of application, absorption chillers can vary

both their design and working fluid. Along this chapter we will discuss the different configurations, according to drive heat source and working fluids that are used in typical absorption chillers. Specifically this manuscript focuses in absorption phenomena using $H_2O - LiBr$ as working fluid and falling film absorber configuration.

1.2 Heat Powered Cooling Systems Technologies

A thermally-driven cooling system replaces the electric power from a compression system by a source of heat. Therefore there is a change in the details of the technology necessary to provide the heat delivery function. This section does not pretend to be exhaustive, only the most important technologies are mentioned:

- Absorption.- In absorption cycles, the heat is delivered with a minimum of input work by using a thermochemical compressor, which is composed by a set of heat exchangers (in the single effect configuration): absorber, generator and a solution heat exchanger. See Fig. 1.1. The rest of the components are: the condenser and the evaporator (separated by an expansion valve). The principle of operation of absorption technology is the affinity of a substance in vapor phase (refrigerant) to be absorbed by other in liquid phase (absorbent). This work is focused in absorption technology. Further information is given in the next section.

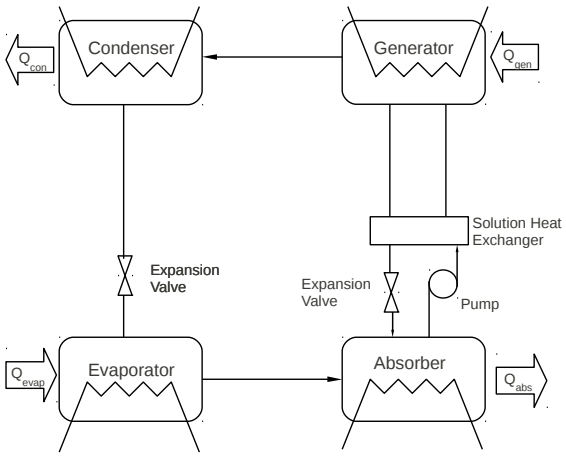

Figure 1.1: Schematic description of a single-effect absorption cycle.

- Desiccant cooling.- This technique consists in conditioning the air first by removing its moisture by means of a desiccant material (See Fig. 1.2). Typically, air that is dried by desiccants is subsequently cooled by an air conditioner or an evaporative cooler. The desiccant materials, which absorb moisture, are dried, or are regenerated, by adding heat supplied by natural gas combustion, wasted heat, or the sun. A desiccant system can be combined with a conventional air conditioning system in which the desiccant removes humidity and the air conditioner cools the air temperature.

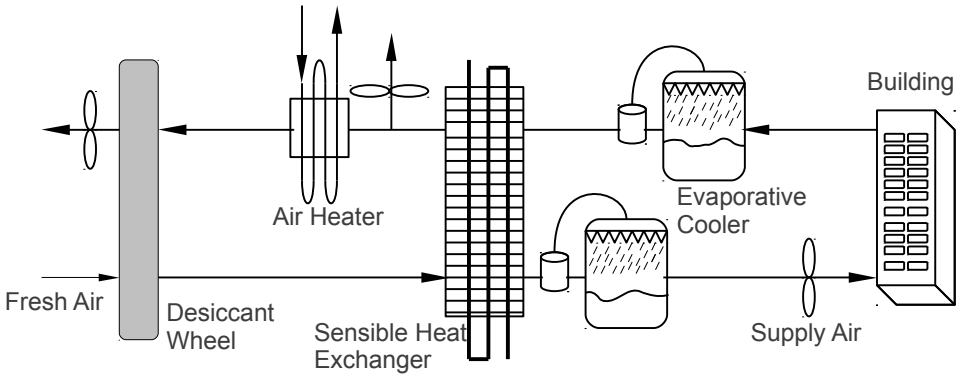

Figure 1.2: Schematic description of a desiccant cooling system

- Adsorption.- Adsorption technology has many similarities to absorption, the main difference lies in that absorbable substance accumulates in the surface rather than in the absorbent bulk (liquid or solid), forming a mono-molecular layer. Usually, in the case of adsorption chillers the absorbable substance is a solid, therefore the adsorption chillers are performed with intermittent cycles. The main applications are ice making and air conditioning. Fig. 1.3 shows the basic cycle of adsorption refrigeration. During the desorption process, the adsorbent is heated and the valve 1 is opened while the valve 2 is closed, then the refrigerant is condensed and the heat is released to the environment. The heat necessary for desorption process can be supplied with a low temperature heat source. After the desorption process, the adsorber is connected to the evaporator via the valve 2. Then the adsorption process generates the cooling effect in the evaporator due to the evaporation of refrigerant. This is the basic intermittent adsorption refrigeration system.

  For a continuous system, two reactors and two condenser/evaporators are needed,

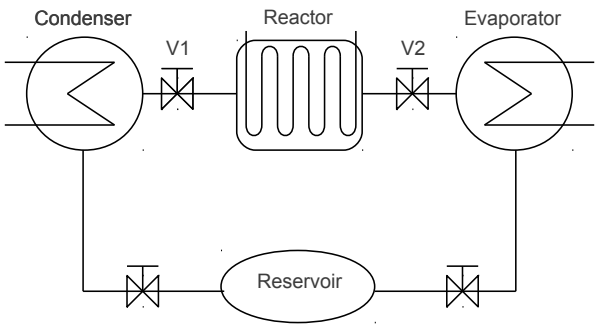

Figure 1.3: Schematic description of a basic intermittent adsorption cycle

as illustrated in Fig. 1.4. Thus, at least four valves should be employed in an adsorption chiller. Both reactors could be connected each other with a valve to achieve mass recovery and a significant improvement of the COP.

- Rankine cycle.-The Rankine cycle is a cycle that converts heat into work. Its main components are the boiler, steam turbine, condenser and feed pump. The mechanical work produced in the turbine is used in a compressor of a vapor compression cycle Fig. 1.5.

- Ejector cooling.- The ejector is thermally driven compressor. In the ejector cycle, the refrigerant at low pressure (e.g. water) is driven by thermal energy, then the refrigerant is condensed, pumped and the kinetic energy transformed in pressure in the ejector. The Fig. 1.6 shows a schematic of the essential elements in an ejector system. The waste heat would be utilized to convert water to super heated steam. The ejector refrigeration cycle has the distinct advantage of being environmentally friendly when water is used as the working fluid, although other refrigerants can be used in this kind of cycles. The ejector refrigeration cycle (as well as absorption cycle) requires very low amount of mechanical work.

1.3 Main Heat Sources of Absorption Chillers

Due to that one of the main advantages of absorption technology is that is a heat driven refrigeration system, the typical heat sources for commercial absorption chillers are listed below,

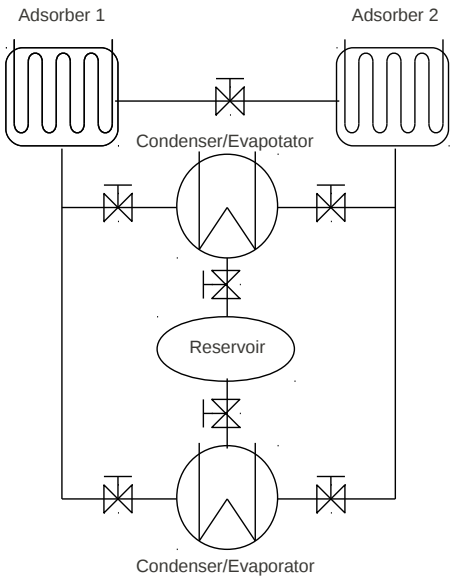

Figure 1.4: Schematic description of a continuous adsorption cycle

- Solar energy.- The solar cooling technologies have been received a great interest in recent years, Other factor that promotes the development of solar cooling is the coincidence between availability of solar irradiation and peaks of cooling demand [4]. The solar cooling technology is environmentally friendly and contributes to a significant decrease of the CO_2 emissions. Currently, most of the solar cooling systems installed used are hot water driven $LiBr-H_2O$ absorption chillers [5].

- Waste Heat.- Most of industrial processes uses a lot of thermal energy by burning fossil fuels to produce steam or heat for the purpose. After the processes, heat is rejected to the surrounding as waste. This waste heat can be converted to a useful refrigeration by using thermally driven refrigeration system, such as an absorption refrigeration cycle [6]. Inside this category there are also the combined cooling, heating and power systems (CCHP). The main potential application of sorption refrigeration for CCHP systems is in public buildings, such as hospitals, hotels, office buildings and food stores [7]. A typical CCHP system is comprised of a gas turbine, generator,heat recovery steam generator (HRSG), and an absorption chiller. Is then in the HRSG where the heat source

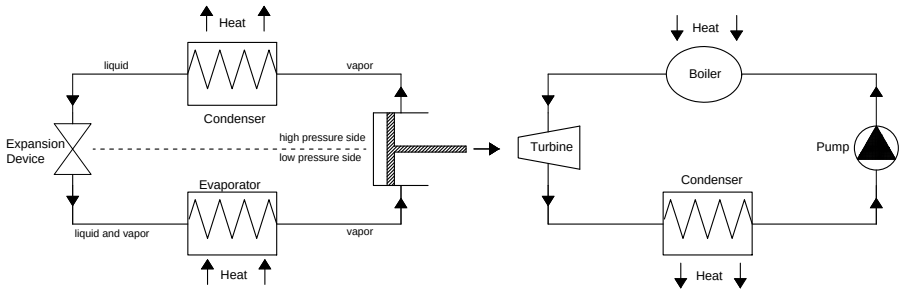

Figure 1.5: Schematic description of a Rankine cycle

is obtained, and it can be steam or hot water.

- Gas.- Gas-Fired Absorption chillers are usually double-effect cycles when they use $H_2O/LiBr$ as working fluid. There are commercial prototypes in marketplace with the main application of providing chilled water for air-conditioning. In the case of $NH_3 - H_2O$ cycles, the gas fired ones can be, single, double effect or GAX cycle configuration. They can be both, direct or indirect fired, the latest offers the possibility of using alternative thermal energy technologies such as advanced concentrating collectors in high beam irradiance areas[8]. Typically, they may be used for refrigeration at temperatures below 0° C [9].

1.4 Principle of Operation of Absorption Refrigeration

The early steps of absorption cooling production dates back to the 1700's. It was known that ice could be produced by an evaporation of pure water from a vessel contained within an evacuated container in the presence of sulfuric acid (1810). The major problems of this system were corrosion and leakage of air into the vacuum vessel [6]. But was Faraday who established the scientific fundamentals of absorption refrigeration in 1823.

Absorption systems have the capacity of converting heat at a given temperature to heat of another temperature without the necessity of any use of intermediate work.

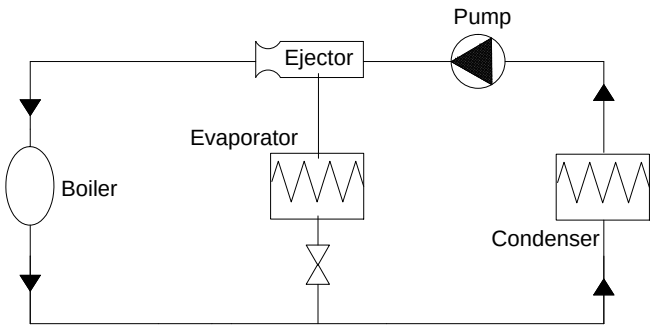

Figure 1.6: Schematic description of an ejector cooling cycle

The working fluid in an absorption refrigeration system is a binary solution consisting of refrigerant and absorbent. In the Fig 1.7 (a), two evacuated vessels are connected to each other. The vessel no.1 contains liquid refrigerant while the vessel no.2 contains an absorbent/refrigerant binary solution. When valve is closed, temperature in vessel 1 is equal to temperature in vessel 2 ($T1 = T2$), and pressure in vessel 1 is greater to pressure in vessel 2 ($P2 < P1$).

When valve is opened, solution in vessel 2 will absorb refrigerant vapor from vessel 1 causing reduction in pressure until $P2 = P1$. While the refrigerant vapor is being absorbed, the temperature of the remaining refrigerant will decrease as a result of its vaporization, $T2 > T1$. This causes a refrigeration effect inside the vessel 1. At the same time, solution inside the vessel 2 becomes more dilute because of the higher content of refrigerant absorbed. This is called the "absorption process". Normally, the absorption process is an exothermic process, therefore, it must reject heat to the surrounding in order to maintain its absorption capability.

Whenever the solution could continue with the absorption process because of saturation of the refrigerant, the refrigerant must be separated out from the diluted solution. The heat is the key for this separation process. It is applied to the vessel 2 in order to separate the refrigerant from the solution as shown in the Fig. 1.7 (b) The refrigerant vapor will be condensed by transferring heat to the surroundings. With these processes, the refrigeration effect can be produced by using heat energy. However, the cooling effect cannot be produced continuously due to the process cannot be done simultaneously. Therefore, an absorption refrigeration cycle is a combination of these two processes as shown in Fig. 1.7. As the separation process occurs at a higher pressure than the absorption process, a circulation pump is required to circulate the solution. The coefficient of performance of an absorption refrigeration

system is obtained from;

$$COP = \frac{\text{Cooling Capacity in Evaporator}}{\text{Input Heat Generator}}$$

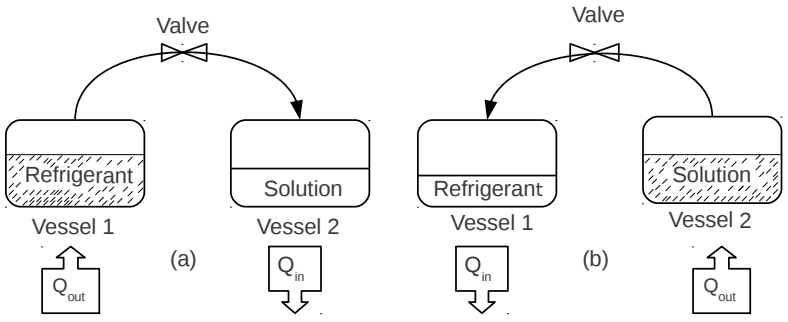

Figure 1.7: Principle of operation.

In a closed cycle, see Fig.1.1, the refrigeration effect is produced in a continuous way. The single effect is composed by five heat exchangers: generator, absorber, solution heat exchanger, condenser and evaporator, a pump and two expansion valves. The high temperature heat supplied to the generator is used to desorb refrigerant out from the solution (rejected out to the surroundings at the condenser) and is used to heat the solution from the absorber temperature (rejected out to the surroundings at the absorber). Thus, an irreversibility is caused as high temperature heat at the generator that is rejected at the absorber and the condenser. In order to reduce this irreversibility, a solution heat exchanger is introduced. The heat exchanger allows the solution from the absorber to be preheated before entering the generator by using the heat from the weak solution leaving the generator. Therefore, the COP is incremented due to that the heat input at the generator is reduced. Moreover, the size of the absorber can be reduced as less heat is rejected. Experimental studies show that COP can be increased up to 60 percent when a solution heat exchanger is used [6].

1.5 Working Fluids

The performance in absorption systems are close related to the chemical and thermophysical properties of working fluids. The fundamental requirements in a refrigerant-absorbent mixture are: i) wide range of miscibility within the operating pressure and temperature conditions in absorber; ii) wide range of immiscibility during generator process; iii) mixture should be chemically stable, non-toxic, and non-explosive.

In addition to these requirements, the following are desirable:

- The elevation of boiling point (the difference in the boiling point between the pure refrigerant and the mixture at the same pressure) should be as large as possible.
- Refrigerant should have a high heat of vaporization and high concentration differences in order to maintain low circulation mass flow between the generator and the absorber. This is desired because in solution loop input work is needed (pump) and also entropy is generated (expansion valve).
- The transport properties that influence heat and mass transfer, e.g., viscosity, thermal conductivity, and diffusion coefficient should be favorable.
- Both refrigerant and absorbent should be non-corrosive, environmental friendly, and low-cost.

In spite of many working fluids that are suggested in literature [6] [10], the most conventional absorption working fluids are ammonia/water (NH_3/H_2O) and water/Lithium Bromide mixtures ($H_2O/LiBr$). Both mixtures offer advantages and disadvantages, and their use is focused for different applications. The working fluid (NH_3/H_2O) has been widely used for both cooling and heating purposes. Both NH_3 (refrigerant) and H_2O (absorbent) are highly stable for a wide range of operating temperature and pressure. NH_3 has a high latent heat of vaporization, which is necessary for an efficient performance of the system. It can be used for applications of refrigeration at low temperature, due to that the freezing point of NH_3 is $-77°C$ but it offers the inconvenient of high pressures, toxicity and corrosive action to copper and its alloys. On the other hand, $H_2O/LiBr$ mixture is advantageous as a solution because $LiBr$ it is essentially non-volatile (a rectifier is not needed in cycle design), it owns an extremely high heat of vaporization and therefore, $H_2O - LiBr$ based cycles have lower driving temperatures than NH_3/H_2O. Therefore, $H_2O/LiBr$ absorption machines should be more adequate for solar assisted air-conditioning. However, using water as a refrigerant limits the evaporator temperature to $0°C$ ($5°C$ to cycles). As water is the refrigerant, the system must be operated under vacuum conditions. Moreover at high concentrations, the solution is prone to crystallization. It is also

corrosive to some metals and expensive.

The choice of the suitable working fluid depends strictly of the desired application of the absorption machine. This thesis focuses in $H_2O/LiBr$ mixture as a working fluid and it has the purpose to provide useful tools for a better design of falling film absorbers applied to absorption refrigeration systems.

1.6 Falling Film Heat Exchanger Design

Free surface and falling film phenomena have been a topic of interest of fluid mechanics due to wide range of application in chemical industry and heat and mass transfer processes. In the case of absorption refrigeration, the falling film can be applied at the generator and the absorber mainly. It has been object of study by many researchers [11–20]. The falling film heat exchangers configuration can be classified in tube bundle horizontal and vertical. In the particular case of falling film absorbers, vertical configuration is related to compact air-cooled absorption machines [17, 21–23]. The $H_2O/LiBr$ absorption systems are used mainly in large cooling capacity applications (industry, large buildings, etc.), therefore they require water from cooling towers to reject heat. However, for middle and low capacity (commercial and residential systems), absorption machines should be air-cooled in order to become competitive.

The falling film offers some advantages that make it attractive in the application of absorption systems:

- The fluid is driven by gravity, therefore pressure drops are practically null.
- It provides good heat transfer coefficients at low temperatures differences.
- The quantity of $LiBr$ solution used is very low.
- The falling film flows are specially advantageous for vacuum equipment.

In falling film absorbers, heat and mass transfer phenomena occur simultaneously. In order to obtain the best performance of the absorber all the governing parameters must be correctly determined such that a maximum heat and mass can be absorbed with a minimum area. Vacuum conditions are also a conditioner in the design of an absorber: i) large components due to specific volume of the water vapor and ii) requirement for hermetically sealed outer vessel. For these reasons the absorber is the key component in an absorption chiller.[24, 25].

1.7 Research objectives

Since the absorber is the most complex component in a absorption refrigeration cycle, this thesis focuses in absorption processes into falling film vertical tubes. Our objective is provide numerical tools with relatively low use of CPU time and experimental information for a better understanding of the absorption phenomena. As mentioned in the previous section 1.6, falling film absorption has been extensively studied, however there are some topics that are not totally understood:

- Wavy Flow.-The vertical falling film has an advantage that horizontal falling film lacks. Wavy regimes appears in vertical falling film from $Re \approx 25$, and its motion enhances both heat and mass transfer when compared with smooth film. However the complete simultaneous heat and mass transfer in a wavy film absorption problem has not been completely well defined analytically. The main difficulties are due to the coupled momentum, heat and mass transfer under the unsteadiness of the wavy motion.

- Effect of non-absorbable gases.- Air leaks into an absorption machine causes unacceptable corrosion problems due to the presence of oxygen, that is the reason why an absorption chiller must be essentially hermetic in design. Is also known than non-absorbable gases are one of the main reasons of the degradations of the absorption performance. When corrosion occurs, Hydrogen is generated, it is essentially inert, non-absorbable in the temperature range of interest and has very low solubility in both liquid water and aqueous $LiBr - H_2O$ solution. Hydrogen has a tendency to migrate from the high pressure side to the low pressure to the side due to the influence of pressure solubility. The primary effect of inert gases is to reduce the performance in absorption process, but the key point is to evaluate how this reduction behaves in function of the quantity of non-absorbable gases.

1.8 Outline of the Thesis

Here is shown a brief description of the chapters which structure this thesis.

- Chapter 2. A review of the principal mechanisms that take place in the absorption process are discussed in this chapter. Both convective and molecular mass transfer mechanisms are presented as well as their role in the liquid-vapor interface treatment in the mathematical models. A brief explanation of absorption driving potential is also presented.

- Chapter 3. An extensive description of both the design and the experimental set-up is presented in this chapter. Equations of data reduction are presented. A brief description of mass spectrometry technology is explained.

- Chapter 4. A simple analytical model based on the resolution of ordinary differential equations a(mass, species and energy) that constitute three ordinary differential equations. Their resolution allows to calculate solution and coolant temperature distributions, and mass flux absorbed along the falling film. This model uses empirical information for heat and mass transfer coefficients.

- Chapter 5 A model based on the modelling of Navier Stokes equations under boundary layer hypothesis coupled with energy and concentration equations. Free Surface Deflection equation and stability problem are introduced into boundary layer model in order to simulate mathematically the wavy motion. The boundary condition in the interface has been modified in order to consider the presence of the mist flow.

  As a first evaluation, numerical results of falling film absorption phenomena under smooth laminar regime are showed.

- Chapter 6. A mathematical model for the influence of non-absorbable gases in wavy regimes are presented. A model under boundary layer hypothesis for mass and momentum equations coupled with energy and mass species equations solving by means numerical methods in both, liquid and vapor sides. The boundary layers model coupled with energy and concentration are discretized in the vapor side. A special attention has been paid for the vapor mass diffusivity evaluation. The absorption pressure in the liquid-vapor interface is recalculated since it depends directly of the air concentration at the interface.

- Chapter 7. The results and conclusions are presented. In the first part an experimental results are compared against mathematical models presented in Chapter 2. In the second part experimental results accompanied with a study of mass spectrometry analysis are compared with the mathematical model described in chapter 5.

- Chapter 8. Conclusions about the work done in the present thesis and comments about the future actions are given in this last chapter.

Bibliography

[1] D. S. Kim and I. Ferreira. Solar refrigeration options- a state of the art review. *International Journal of Refrigeration*, 31(2008):3–15, 2007.

[2] T. F. Stocker, G. K. Qin, M. Plattner, S. K. Tignor, J. Allen, A. Boschung, Y. Nauels, and V. Xia. IPCC, 2013: Climate Change 2013: The Physical Science Basis. Contribution of Working Group I to the Fifth Assessment Report of the Intergovernmental Panel on Climate Change. Technical report, Cambridge University Press, 2013.

[3] European Solar Thermal Technology Plataform. Solar Heating nad Cooling for a Sustainable Energy Future in Europe. Technical report, 2010.

[4] A. Gonzalez-Gil, M. Izquierdo, J. D. Marcos, and E. Palacios. Experimental Evaluation of a direct air-cooled lithium bromide-water absorption prototype for solar air conditioning. *Applied Thermal Engineering*, 31(2011):3358–3368, 2011.

[5] X. Q. Zhai, M. Qu, Li. Yue, and R. Z. Wang. A review for research and new design options of solar absorption cooling systems. *Renewable and Sustainable Energy Reviews*, 15(2011):4416–4423, 2011.

[6] Srikhirin Pongsid, Aphornratana Satha, and Chungpaibulpatana Supachart. A review of absorption refrigeration technologies. *Renewable and Sustainable Energy Reviews*, 5(4):343–372, 2001.

[7] J. Deng, R. Z. Wang, and G. Y. Han. A review of thermally activated cooling technologies for combined cooling, heating and power systems. *Progress in Energy and Combustion Science*, 31(2011):172–203, 2010.

[8] V. H. Gomez, A. Vidal, R. Best, O. García-Valladares, and N. Velazquez. Theoretical and experimental evaluation of an indirect-fired GAX cycle cooling system. *Applied Thermal Engineering*, 28(2008):975–987, 2007.

[9] He. Yijian and Chen. Guangming. Experimental study on an absorption refrigeration system at low temperatures. *Progress in Energy and Combustion Science*, 46(2007):294–299, 2006.

[10] S. Jian, F. Lin, and Z. Shingang. A review of working fluids of absorption cycles. *Progress in Energy and Combustion Science*, 16(2012):1899–1906, 2012.

[11] J. W. Andberg. *Absorption of Vapours into Liquid Films Flowing over Cooled Horizontal Tubes*. PhD thesis, University of Texas, 1986.

[12] J. D. Killion and S. Garimella. A Critical Review of Models of Coupled Heat and Mass Transfer in Falling-Film Absorption. *International Journal of Refrigeration*, 24(8):755–797, 2001.

[13] R. Yang and B. D. Wood. A numerical Modelling of an Absorption Process on a Liquid Falling Film. *Solar Energy*, 48(3):195–198, 1992.

[14] M. H. Yuan, Y. H. Yang, T. S. Li, and Z. H. Hu. Numerical Simulation of Film Boiling on a Sphere with a Volume of Fluid Interface Tracking Method. *International Journal of Heat and Mass Transfer*, 51(7-8):1646–1657, 2008.

[15] S. G. Bankoff. Minimum Thickness of a Draining Liquid Film. *International Journal of Heat and Mass Transfer*, 14(12):2143–2146, 1971.

[16] J. Castro, C. Oliet, J. Farnós, and A. Oliva. Numerical Study of Falling Film and Bubble Absorbers for Small Capacity NH_3-H_2O Air-Cooled Absorption Systems. In *Proceedings of the 22th International Congress of Refrigeration*, pages 1–8, 2007.

[17] J. Castro. *Simulation of Heat and Mass Transfer Phenomena in the Critical Elements of H_2O-LiBr Absorption Cooling Machines. Experimental Validation and Application to Design.* PhD thesis, Universitat Politècnica de Catalunya, 2005.

[18] M. C. Chyu and A. E. Bergles. An Analytical and Experimental Study of Falling-Film Evaporation on a Horizontal Tube. *Journal of Heat Transfer - Transactions of ASME*, 109(4):983–990, 1987.

[19] M. S. Genk and H. H. Saber. An Investigation of the Breakup of an Evaporating Liquid Film, Falling Down a Vertical, Uniformly Heated Wall. *Journal of Heat Transfer - Transactions of ASME*, 124(1):39–49, 2002.

[20] S. Jani and A. Heydari. Falling film Generators of Absorption Chillers Thermal Hydraulic Design. Technical report, Department of Mechanical Engineering, Shariff University, 1984.

[21] J. Castro, C. Oliet, I. Rodríguez, and A. Oliva. Comparison of the Performance of Falling Film and Bubble Absorbers for Air-Cooled Absorption Systems. *International Journal of Thermal Sciences*, 48(7):1355–1366, 2009.

[22] J. Castro, A. Oliva, C. D. Pérez-Segarra, and C. Oliet. Modelling of the Heat Exchangers of a Small Capacity, Hot Water Driven, Air-Cooled H_2O-LiBr Absorption Cooling Machine. *International Journal of Refrigeration*, 31(1):75–86, 2008.

[23] J. Castro, A. Oliva, C. D. Pérez-Segarra, and J. Cadafalch. Evaluation of a Small Capacity, Hot Water Driven, Air-Cooled H_2O-LiBr Absorption Machine. *International Journal of Heat Ventilation Air Conditioning and Refrigeration Research*, 13(1):59–75, 2007.

[24] K. E. Herold, R. Radermacher, and S. A. Klein. *Absorption Chillers and Heat Pumps*. CRC Press, 1996.

[25] G. Alefeld and R. Radermacher. *Heat Conversion Systems*. CRC Press, 1994.

Chapter 2

Fundamentals of Heat and Mass Transfer phenomena in liquid Falling Film Absorption

ABSTRACT

This chapter summarizes some fundamentals of heat and mass transport in falling film absorption. Since one of the objectives of this manuscript is the development of mathematical tools for the simulation of vertical absorbers, it is necessary to explain the foundations of the main mechanisms that drives the absorption phenomena. First of all, a brief description of the main falling film parameters is presented. Then, the fundamentals of molecular and convective mass transfer and their application into the mathematical models, as well as the relation between mass absorbed and heat transport through the liquid-vapor interface, are described. Finally, the principle of pressure driving potential that promotes the absorption phenomena is explained through the equilibrium pressure temperature diagram.

2.1 Introduction

A falling film flow is a gravity driven flow of a continuous liquid film down over solid tube (or plate) having a free surface. There are many geometries and configurations, but this work is focused in the vertical tube configuration with falling film in the outside diameter and countercurrent flow inside.

The absorption phenomena in falling film flows is a topic that has several problems to be solved simultaneously: i) particularities of the hydrodinamics (the presence of a free surface boundary adds a certain degree of complexity); ii) coupled heat and mass transfer mechanisms and its influence to the film flow; iii) technological implementation due to all this characteristics. Its application in absorption technology has received much attention by many researches [1–19].

2.2 Falling Film hydrodinamics parameters

Probably the first systematic approach of the flow characteristics of a liquid falling film was made by Nusselt [20]. He derived, for a fully developed falling film flow, an expression for the velocity profile as a function of the maximum velocity and the film thickness. The Nusselt's analytical solution is the simplest way to approach falling film hydrodynamics and is very useful to determine some basic relations. This work uses the solution of the velocity profile from Nusselt solution to determine the inlet boundary conditions in the mathematical model described in chapter 5. The Nusselt's analysis makes the following assumptions (see Fig. 2.1),

- Laminar smooth flow.
- Steady state.
- Physical properties are constant, density (ρ) and viscosity (μ).
- The length L is much greater in order of magnitude as the thickness δ.
- The thickness (δ) remains constant along the film.
- The mass flow ($\dot{m}$) remains constant along the film.
- The velocity varies only across the film thickness $u = u(y)$.
- The inertia terms becomes null, therefore the gravity force becomes equal to shear stress force.
- There is no shear stress at the interface.

- The pressure gradients are negligible.

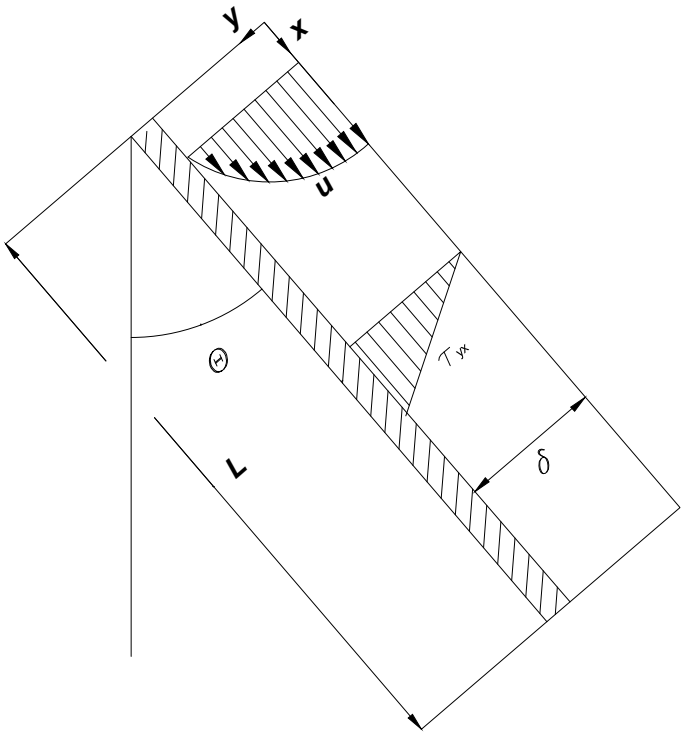

Figure 2.1: Schematic description of a falling film. Velocity profiles obtained by Nusselt [20].

The boundary conditions are:

$$y = 0 \begin{cases} u = u(y) \\ \tau_{yx} = 0 \\ v = 0 \end{cases} \tag{2.1}$$

$$y = \delta \begin{cases} u = 0 \\ \tau_{yx} = -\mu \frac{du}{dx} \\ v = 0 \end{cases} \tag{2.2}$$

The analysis makes the assumption of a smooth free surface. For a specified flow Reynolds number Re, the velocity profile is describes as:

$$u = U_N \left[2\frac{y}{\delta} - \left(\frac{y}{\delta}\right)^2 \right] \tag{2.3}$$

where, $U_N = \frac{\rho g \delta^2}{2\mu}$ and $\delta = \left(\frac{3\mu U_o}{\rho g}\right)^{\frac{1}{2}}$. Other typical parameter in falling film flows is the flow rate per unit of length Γ,

$$\Gamma = \frac{\dot{m}}{\pi d_{out}} \tag{2.4}$$

Then Reynolds number can be obtained in terms of Γ by using the concept of hydraulic diameter,

$$Re = \frac{4\Gamma}{\mu} \tag{2.5}$$

Other of the early investigations was made by Kapitza [21], who did both theoretical and experimental developments. He developed a dimensionless group which is function of the fluid properties, specifically he combined certain properties of the "kinematic surface tension" (as he called the ratio of the usual surface tension over the density of the liquid), kinematic viscosity (shear or dynamic viscosity divided by density) and gravity acceleration.

$$Ka = \frac{\sigma}{\rho \nu^{4/3} g^{1/3}} \tag{2.6}$$

The above parameter expresses the ratio of surface tension forces to inertial forces. The Ka number is an useful parameter in the study of wave growth and instability in falling liquid films, it acts as an indicator of the hydrodynamic wave regime in falling liquid films. This number is used in section 5.2.1 as surface tension parameter in order to solve Free Surface Deflection Equation (5.20).

The Weber number is another group that emerge from the natural scaling of the Navier-Stokes equations for constant property falling liquid film. It is named after Moritz Weber. The Weber number measures the importance of surface tension relative to inertial effects and is evaluated in terms of the Nusselt film parameters. It

is a useful parameter in analyzing thin film flows and the formation of droplets and bubbles:

$$We = \frac{\sigma}{\rho \delta u^2} \tag{2.7}$$

The Froude number (Fr) is another dimensionless number, named after William Froude. It defined as the ratio of the flow inertia to the body forces (usually due to only the gravity). Froude number is also know as speed–length ratio and it is defined as follows,

$$Fr = \frac{v^2}{g\delta} \tag{2.8}$$

2.3 Fundamentals of Mass Transfer in Falling Films

Since the nature of absorption phenomena entails simultaneous heat and mass transport, this section is devoted to summarize some of the fundamentals mechanisms of mass transfer. The mass can be transferred by random molecular motion in quiescent fluids, or it can be transferred from a surface into a moving fluid, aided by the dynamic characteristics of the flow. These two distinct modes of transport, molecular mass transfer and convective mass transfer, are analogous to conduction heat transfer and convective heat transfer. Each of these modes of mass transfer are involved during absorption in vertical falling films. In fact, both mechanisms often can act simultaneously.

2.3.1 Molecular Mass Transfer

The molecular mass transfer, or diffusion, as it is also called, occurs in mixtures. Its evaluation must involve an examination of the effect of each component (species). Due to each component owns a different mobility, the mixture velocity must be evaluated by averaging the velocities of all the present components. In multicomponent mixtures, the concentration of each specie can be represented in many ways [22–24]. Throughout this work, we use the concept of the mass fraction in order to refer to the concentration, the mass fraction concentration is defined by the mass concentration of the component A (ρ_A) divided by the total density of the mixture,

$$c_A = \frac{\rho_A}{\rho} \tag{2.9}$$

In the binary mixture $LiBr - H_2O$ solution it yields,

$$c_{LiBr} = \frac{\rho_{LiBr}}{\rho} \tag{2.10}$$

Along this manuscript (unless otherwise is indicated) the concentration is always referred to $LiBr$ component, therefore subscript is omitted ($c_{LiBr} = c$). The mass flux of a given species is defined as a vector quantity indicating the amount particles of a species (in either molar or mass units) moving through an unit area per unit of time. An empirical relation for such mass flux is referred as Fick's first law,

$$j_A = -\rho D_{AB} \nabla c \tag{2.11}$$

The above expression represents the mass flux relative to the mass average velocity. In order to express the mass flux with respect fixed coordinates, we need two more inputs [24]: i) the concentration gradient contribution and ii) the bulk motion contribution. The final expression yields:

$$\vec{n}_A = c_A(\vec{n}_A + \vec{n}_B) - j_A \tag{2.12}$$

It is interesting to denote that the resulting mass flux $\vec{n}_A$ is relative to stationary axes and it is the resultant of two vector quantities. Taking into account the concept of mass average velocity [1] the equation (2.12) can also be represented as follows,

$$\vec{n}_A = \rho_A \vec{v}_A = c_A(\rho_A \vec{v}_A + \rho_B \vec{v}_B) - \rho_{AB} D_{AB} \nabla c_A \tag{2.13}$$

For the binary mixture $LiBr - H_2O$ the final expression yields,

$$\rho_{l,H_2O} \vec{v}_{H_2O} = c_{H_2O}(\rho_{l,H_2O} \vec{v}_{H_2O} + \rho_{l,LiBr} \vec{v}_{LiBr}) - \rho_l D_l \nabla c_{H_2O} \tag{2.14}$$

The above equation can be represented in terms of the total liquid flux ($\vec{v}_l$),

$$\rho_{l,H_2O} \vec{v}_{l,H_2O} = \rho_{l,H_2O} \vec{v}_l - \rho_l D_l \nabla c_{H_2O} \tag{2.15}$$

The form of the equation (2.15) is suitable for obtaining an expression which allows the calculation of the mass flux absorbed by the falling film in a mobile interface.

[1] The mass-average velocity for a multicomponent mixture is defined in terms of the mass densities and velocities of all components.

2.3.2 Calculating the mass absorbed in a vertical falling film

In order to obtain an expression that allows the calculation of the mass flow absorbed in a vertical falling film in the binary mixture we refer to the Fig. 2.2. The mass flow can be expressed as the difference between the fluid velocity (vapor or liquid) and the interface velocity multiplied by the corresponding fluid density,

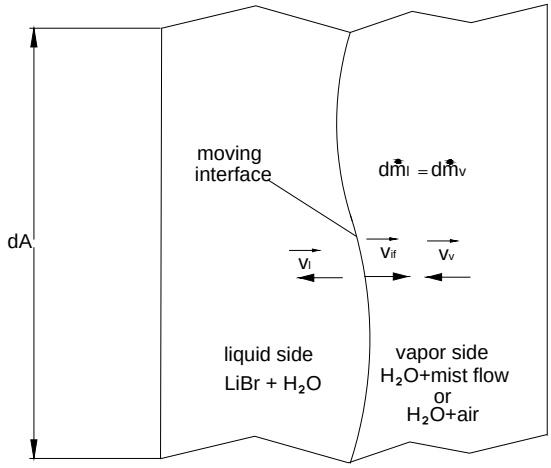

Figure 2.2: Absorption process in the falling film interface

$$d\dot{m}_l = \rho_l(\vec{v}_l - \vec{v}_{if}) \cdot \vec{n}\ dA = d\dot{m}_v = \rho_v(\vec{v}_v - \vec{v}_{if}) \cdot \vec{n}\ dA \tag{2.16}$$

The liquid phase is denoted with the subscript lO, while v represents the vapor side. Since $\dot{m}_l = \dot{m}_v$, the expression for the mass absorbed can be derived from either, the liquid or the vapor side. Along this section, all the deductions are from the point of view of the liquid side, however the same analysis can be derived from the point of view of the vapor side. Therefore the water mass which passes from vapor to liquid side through the interface is expressed by the following expression,

$$\rho_l(\vec{v}_l - \vec{v}_{if}) \cdot \vec{n}\ dA = \rho_{l,H_2O}(\vec{v}_{l,H_2O} - \vec{v}_{if}) \cdot \vec{n}\ dA + \rho_{l,LiBr}(\vec{v}_{l,LiBr} - \vec{v}_{if}) \cdot \vec{n}\ dA \tag{2.17}$$

In the above equation the terms $\vec{v}_{l,H_2O}$ and $\vec{v}_{l,LiBr}$ represent the absolute velocity of species H_2O and $LiBr$ relative to stationary coordinate axes, respectively. The $LiBr$ component is not volatile, therefore the diffusion velocity of $LiBr$ relative to mass average interface velocity becomes zero ($\vec{v}_{l,LiBr} - \vec{v}_{if} = 0$),

$$\rho_l(\vec{v}_l - \vec{v}_{if}) \cdot \vec{n}\ dA = \rho_{l,H_2O}\vec{v}_{l,H_2O} \cdot \vec{n}\ dA - \rho_{l,H_2O}\vec{v}_{if} \cdot \vec{n}\ dA \tag{2.18}$$

Going back to the equation (2.15) and replacing into the equation (2.18) we obtain the following expression,

$$\begin{aligned} \rho_l(\vec{v}_l - \vec{v}_{if}) \cdot \vec{n}\ dA &= -\rho_l D_l \nabla c_{H2O} \cdot \vec{n}\ dA + \\ \rho_{l,H_2O}\vec{v}_l \cdot \vec{n}\ dA &- \rho_{l,H_2O}\vec{v}_{if} \cdot \vec{n}\ dA \end{aligned} \tag{2.19}$$

Adding and subtracting the term $\rho_l c_{H_2O,if}\vec{v}_{if} \cdot \vec{n}$, using definition of partial density of substance $\rho_l c_{H_2O} = \rho_{l,H_2O}$ in above equation and rearranging it yields,

$$\rho_l(\vec{v}_l - \vec{v}_{if})(1 - c_{H_2O,if}) \cdot \vec{n}\ dA = -\rho_l D_l \nabla c_{H2O} \cdot \vec{n}\ dA \tag{2.20}$$

Finally the resulting expression of mass absorbed,

$$d\dot{m}_{abs,l} = \rho_l(\vec{v}_l - \vec{v}_{if}) \cdot \vec{n}\ dA = \frac{-\rho_l D_l}{(1 - c_{H_2O,if})} \nabla c_{H2O} \cdot \vec{n}\ dA \tag{2.21}$$

The equation (2.21) is expressed en terms of c_{H2O} concentration, but also it can be expressed in terms of c_{LiBr}

$$d\dot{m}_{abs,l} = \rho_l(\vec{v}_l - \vec{v}_{if}) \cdot \vec{n}\ dA = -\frac{D_l \rho_l}{c_{if}} \nabla c \cdot \vec{n}\ dA \tag{2.22}$$

The above equation is reescribed in order to include the influence of mist flow (this topic will be discussed in detail in chapter 3),

$$d\dot{m}_{abs_{H_2O,t}} = \frac{(1-c_{if})\dot{m}_{abs,l}c_{in}}{c_{if}} - \frac{D_l\rho_l}{c_{l,if}}\nabla c\cdot\vec{n}\ dA \tag{2.23}$$

The first term or the left member of above equation represents the mist flow contribution [2]. In appendix C are further details about the equation (2.24).

Both equations (2.21) and (2.22) are equivalents, in fact analogous equations can be obtained in vapor side, such equations will be obtained when measuring non-absorbable effects in chapter 6 without considering the effects of mist flow.

$$d\dot{m}_{abs,v} = -\frac{\rho_v D_v}{1-w}\nabla w\cdot\vec{n}\ dA \tag{2.24}$$

where w denotes the mass fraction concentration in the vapor mixture H_2O-air. Along this work (unless otherwise is indicated) the vapor side concentration is always referred to H_2O component, therefore the subscript is omitted $w_{H_2O}=w$.

2.3.3 Convective Mass Transfer

The mass transfer between two immiscible moving fluids separated by a mobile interface is often aided by the dynamic characteristics of the fluids involved. This mode of mass transfer is called convective mass transfer. The convective transport depends on both the transport properties (viscosity, thermal conductivity and diffusion coefficient) and the dynamic characteristics of the flowing fluid [22]. Similarly with convective heat transfer, forced and natural (free) convection are distinguished. The rate equation for convective mass transfer, generalized in a way analogous to Newton's law of convective heat transfer, results in:

$$d\dot{m}_{H_2O} = \kappa_l\Delta\rho_{H_2O}\ dA \tag{2.25}$$

The equation (2.25) can be also expressed in terms of the mass fraction concentration,

$$d\dot{m}_{H_2O} = \kappa_l\rho_l\Delta c_{H_2O}\ dA \tag{2.26}$$

Both the heat and the mass-transfer coefficients are related to the properties of the fluid, the dynamic characteristics of the flowing fluid, and the geometry of the

[2] Mist flow is defined as micro droplets of $LiBr-H_2O$ solution, that are dragged from the generator.

specific system of interest. In absorption of water vapor into aqueous solution of $LiBr$ convective mass transfer is expressed across liquid-vapor interface. If we assume equilibrium conditions in the interface therefore there is no mass transfer resistance. The mass flow of water vapor is totally absorbed into liquid film,

$$d\dot{m}_l = d\dot{m}_v \tag{2.27}$$

or,

$$\kappa_l \rho_l (c_{l,b} - c_{l,if})\ dA = \kappa_v \rho_v (c_{v,if} - c_{v,b})\ dA \tag{2.28}$$

The right side of above equation represents the mass flux per unit area in the vapor side. The concentration difference is taken into account when there is presence of air in the vapor side. The above equation represents mass absorbed through convective mass transfer. There are dimensionless parameters that are often used to correlate convective transport data. First of all, we shall to remember the molecular diffusivities of the three main transport phenomena: *momentum diffusivity*, $\nu = \frac{\mu}{\rho}$, *thermal diffusivity*, $a = \frac{k}{\rho c_p}$, and *mass diffusivity* D_{AB}. The ratio of the molecular diffusivity of momentum related to the molecular diffusivity of mass is designated as the *Schmidt* number

$$\frac{\text{momentum diffusivity}}{\text{mass diffusivity}} = Sc = \frac{\nu}{D_{AB}} = \frac{\mu}{\rho D_{AB}} \tag{2.29}$$

The Schmidt number plays a role in convective mass transfer analogous to that of the Prandtl number in convective heat transfer. The ratio of the thermal diffusivity related to the molecular diffusivity of mass is designated as the *Lewis* number.

$$\frac{\text{thermal diffusivity}}{\text{mass diffusivity}} = Le = \frac{k}{\rho c_p D_{AB}} \tag{2.30}$$

The Lewis number is encountered when process involves the simultaneous convective transfer of mass and energy. Finally, the ratio of molecular mass-transport resistance related to the convective mass transfer resistance of the fluid is called *Sherwood* number.

$$\frac{\text{convective mass transfer}}{\text{mass diffusivity}} = Sh = \frac{\kappa L_{ref}}{D_{AB}} \tag{2.31}$$

Where L_{ref} is the significant length, in the specific situation of falling film, we assume $L_{ref} = \delta$, therefore the Sherwood number is redefined as $Sh = \frac{\kappa\delta}{D_{AB}}$. The Sherwood number has also been referred to as the *mass transfer Nusselt number*. These three parameters Sc, Sh, and Le, will be encountered in the analysis of convective mass transfer in the following chapters.

So far we have discussed two expressions to access the calculation of the absorbed mass through a the LiBr aqueous solution falling film, (equations 2.22 and 2.28), in chapters 4, 5 and 6 such expressions will be employed according to the mathematical model applied. Specifically, the expression (2.24) will be applied in mathematical models where field concentrations can be calculated, while the expression (2.28) needs empirical information for the mass transfer coefficient.

2.4 Heat Transport in Falling Films

During the absorption phenomena the heat and mass transport occurs simultaneously. As the mass is transported across the interface, it must change phase and join to $LiBr - H_2O$ mixture. It means two aspects: i) the heat and mass processes are fully coupled, and ii) heat absorbed is almost proportional to the mass absorbed.

$$-\lambda_l \nabla T_l = -\frac{\rho_l D_l}{c_{if}} \nabla c \; h_{abs} - \lambda_v \nabla T_v \tag{2.32}$$

The equation (2.32) depicts an energy balance by unit surface which is performed in the liquid vapor interface. Notice that the first term in the right side of the equation (2.15) represents the mass absorbed through the interface. In order to evaluate the equation (2.32) it is necessary to compute the temperature and concentration fields across the falling film and evaluate the conditions in the liquid-vapor interface (T_{if}, c_{if}). Here a new term is introduced: enthalpy of absorption, that is function of both temperature and concentration $h_{abs} = f(T_{if}, c_{if})$. It is defined as the change in the enthalpy from vapor state and the enthalpy at solution state (also defined as the difference between vapor enthalpy and the heat of mixing). The term h_{abs} coupled with the term $\dot{m}_{abs}$ represent energy input through the interface, $\dot{Q}_{abs} = h_{abs}\dot{m}_{abs}$.

2.5 Driving Potential in Absorption Phenomena

As commented in chapter 1, the principle of absorption phenomena consists in the affinity of a substance in vapor phase (substance A) with a liquid binary mixture (substances A + B). In other words, the absorption phenomena describes the transfer of a vapor into an absorbent in liquid or solid state. Absorption is similar to condensation

in the sense that a phase change occurs from a vapor state to a liquid state. However, absorption phenomena is more complex than condensation since it implies the participation of a binary mixture. The Fig. 2.3 represents the equilibrium pressure temperature diagram for $LiBr - H_2O$ at different mass fraction concentrations. Note that for constant temperature the equilibrium pressure increases as the mass fraction decreases. The equilibrium pressure plays a key role in the absorption process, it is one of the causes of the driving potential that promotes the absorption phenomena.

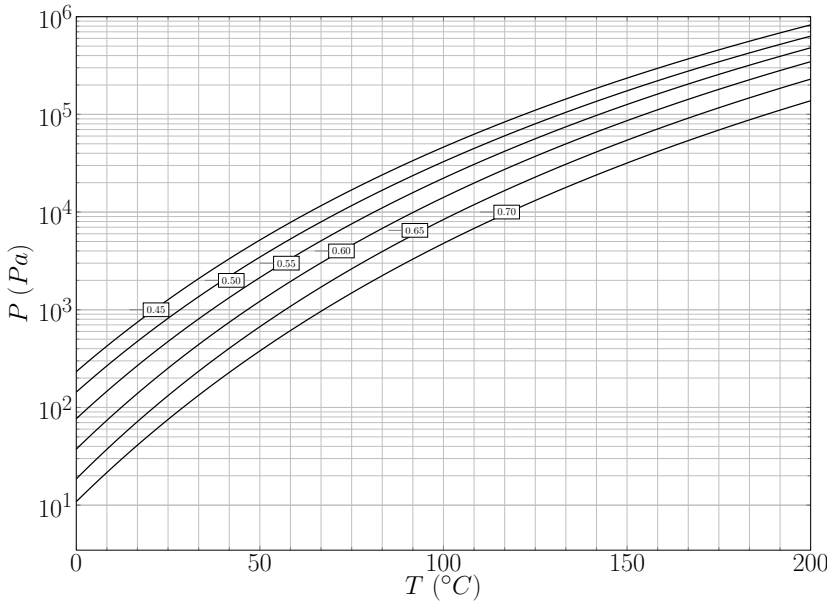

Figure 2.3: Pressure-temperature diagram for $LiBr - H_2O$ [25]

The driving force for mass transfer through the vapor-liquid interface can be expressed as the difference between the partial pressure of water-vapor in the interface $P_{abs_{if}}$ and the local theoretical average equilibrium pressure of $H_2O - LiBr$ aqueous solution at given temperature and concentration $\bar{P}_{abs_{eq}}$. If we assume that there are not non-absorbable gases, then vapor pressure in the interface is equal to vapor pressure in the bulk and it keeps constant along the interface. $P_{abs_{if}} = P_{abs_b}$. In contrast, when considering gradients of concentrations caused by air in the vapor side, the vapor pressure in the interface is not constant and its value decreases along the interface $P_{abs_{if}} \neq P_{abs_b}$ (see Fig. 2.4).

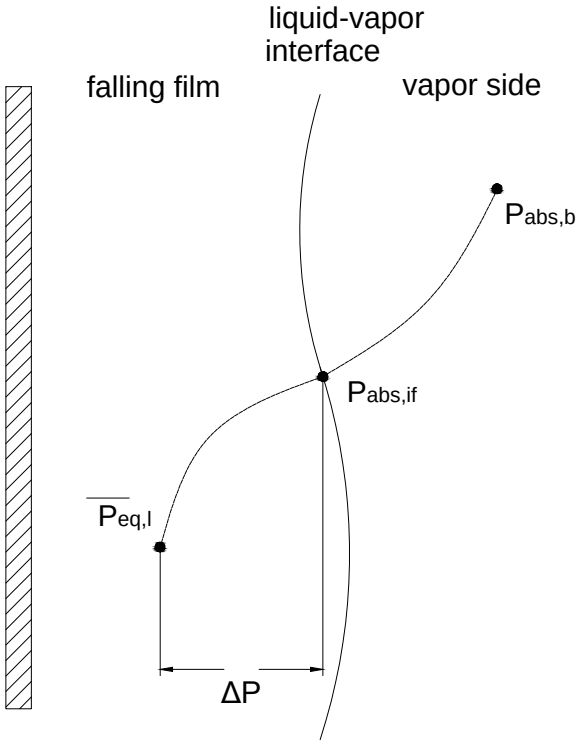

Figure 2.4: Schematic representation of the pressure driving potential in vertical falling film.

Nomenclature

a	thermal diffusivity, $m^2 s^{-1}$
c	$LiBr$ mass fraction concentration
c_p	specific heat capacity, $J\ kg^{-1}\ K^{-1}$
d	tube diameter, m
D	mass diffusivity, $m^2\ s^{-1}$
g	acceleration due to gravity, $m\ s^{-2}$
h	specific enthalpy, $J\ kg^{-1}$
j	mass flux relative to the average velocity, $kg\ s^{-1} m^{-1}$
$\dot{m}$	mass flow rate, $kg\ s^{-1}$

n_i	mass flow density of species i, $kg\ m^{-1}\ s^{-2}$
$\vec{n}$	outward directed unit normal vector, m
L_{ref}	reference length, m
p	perimeter, m
P	pressure, Pa
$\dot{Q}$	heat rate, W
T	temperature, K
U_N	maximum velocity in the interface the film, $m\ s^{-1}$
U_o	average velocity in the transversal section of the film, $m\ s^{-1}$
u	velocity component in x direction, $m\ s^{-1}$
w	H_2O mass fraction concentration in vapor side
x	longitudinal coordinate, m
y	transversal coordinate, m

Greek symbols

δ	film thickness, m
Δ	gradient between two magnitudes.
Γ	mass flow rate per unit length, $kg\ s^{-1}\ m^{-1}$
κ	mass transfer coefficient $m\ s^{-1}$
μ	dynamic viscosity, $kg\ m^{-1}\ s^{-1}$
ν	cinematic viscosity, $m^{2\ s^{-1}}$
λ	thermal conductivity, $W\ m^{-1}\ K^{-1}$
ρ	density, $kg\ m^{-3}$
ρ_i	mass concentration in specie i, $kg\ m^{-3}$
τ	shear stress, Pa
σ	superficial tension, $N\ m^{-1}$

Dimensionless Parameters

Re	Reynolds Number
Ka	Kapitza Number
Sc	Schmidt Number
Le	Lewis Number
Sh	Sherwood Number
We	Weber Number

Subscripts

A	referent to component A in a multicomponent mixture

abs	absorption
B	referent to component B in a multicomponent mixture
b	bulk
eq	equilibrium
H_2O	referent to the water component in aqueous solution
if	interface conditions
l	liquid phase in LiBr solution
$LiBr$	referent to the LiBr component in aqueous solution
t	total
out	outlet conditions
v	vapor phase

Superscripts

$^{-}$ average value

Bibliography

[1] J. U. Brackbill, D. B. Kothe, and C. Zemach. Modelling of Wavy Flow in turbulent free falling films. *International Journal of Multiphase Flow*, 15(1):505–520, 1989.

[2] R. I. Hirshburg. *Laminar Film FLow Phenomena, Theory and Application to the Two-Phase Closed Thermosyphon.* PhD thesis, Arizona State University, 1980.

[3] R. I. Hirshburg and L. W. Florschuetz. Laminar Wavy-Film Flow: Part I, Hydrodynamic Analysis. *ASME J. Heat Transfer*, 104(1):452–458, 1982.

[4] R. I. Hirshburg and L. W. Florschuetz. Laminar Wavy-Film Flow: Part II, Condensation and Evaporation. *ASME J. Heat Transfer*, 104(1):459–464, 1982.

[5] J. Kim and K. Cho. Enhancement of Absorption Performance due to the Film Wave Formation on Vertical Absorber. In *3rd International Symposium on Two-Phase Flow Modelling and Experimentation.*, pages 1–5, 2004.

[6] W. A. Miller and M. Keyhan. The Effect of Roll Waves on the Hydrodynamics of Falling Films Observed in Vertical Column Absorbers. In *Proceedings of the ASME Advanced Energy Systems Division 2001*, pages 1–12, 2001.

[7] C. D. Park, T. Nosoko, S. Gima, and S. T. Ro. Wave-augmented mass tranfer in a liquid film falling inside a vertical tube. *International Journal of Heat and Mass Transfer*, 47(2004):2587–2598, 2003.

[8] V. Patnaik. *Combined Heat and Mass Transfer in Wavy-Film Absorption.* PhD thesis, Pennsylvania State University, 1994.

[9] V. Patnaik and H. Pérez-Blanco. A study of absorption enhancement by wavy film flows. *International Journal of Heat and Fluid Flow*, 17(1):63–70, 1995.

[10] V. Patnaik and H. Pérez-Blanco. Roll Waves in falling films:an approximate treatment of the velicity field. *International Journal of Heat and Fluid Flow*, 17(1):63–70, 1995.

[11] F. W. Pierson and S. Whitaker. Some Theoretical and Experimental Observations of the Wave Structure of Falling Liquid Films. *Journal of Fluid Mechanics*, 16(4):401–407, 1977.

[12] H. Sabir, K. O. Suen, and G. A. Vinnicombe. Investigation of effects of wave motion on the performance of a falling film absorber. *International Journal of Heat and Mass Transfer*, 39(12):2463–2477, 1995.

[13] V. Ya. Shkadov. Wave Flow Regimes of Thin Layer of Viscous Fluid Subject to Gravity. *Fluid Dynamics*, 2(1):43–51, 1967.

[14] V. Ya. Shkadov. Wave Flow Theory for a Thin Viscous Liquid Layer. *Fluid Dynamics*, 3(2):12–15, 1968.

[15] P. Wayne. Some Theorical and Experimental Observations of the Wave Structure of Falling Film Liquid Films. *Industrial and Engineering Chemical Fundamentals*, 16(4):401–406, 1977.

[16] Ru Yang. *Heat and Mass Transfer in Laminar Wavy Film Absorption with the Presence of Non-Absorbable Gases.* PhD thesis, Arizona State University, 1987.

[17] R. Yang and D. Wood. A Numerical Solution of the Wavy Motion on a Falling Liquid Film. *Solar Energy*, 69(1):723–728, 1991.

[18] R. Yang and D. Jou. Heat and Mass Transfer on Wavy Film Absorption Process. *Solar Energy*, 71(3):533–538, 1993.

[19] S. M. Yih and K. Y. Chen. Gas Absorption Into Wavy and Turbulent Falling Films in a Wetted-Wall Column. *Chemical Engineering*, 17(1):123–136, 1982.

[20] W. Nusselt. Die oberflachen Kondensation das Wasserdampfes. Technical report, VDI-Zeitschrift, 1910.

[21] D. T. Haar. *Collected papers of P.L. Kapitza.* Pergamon Press, 1965.

[22] R. B. Bird, W. E. Stewart, and E. N. Lightfoot. *Fenómenos de Transporte.* REVERTÉ, 1973.

[23] C. O. Bennett and J. E. Myers. *Momentum, Heat, and Mass Transfer.* McGraw-Hill, 1975.

[24] J. R. Welty, C. E. Wicks, R. E. Wilson, and G. L. Rorrer. *Fundamentals of momentum, Heat and Mass Transfer.* Willey, 2008.

[25] L. McNeely. Thermodynamic Properties of Aqueous Solutions of Lithium Bromide. *ASHRAE Transactions*, 85(1):413–434, 1979.

Chapter 3

Experimental Setups and Procedures

ABSTRACT

This chapter gives a description about the design, construction and commissioning of the vertical absorption experimental apparatus. Details about construction materials, measuring sensors are exposed. During the development of this work, the authors have paid careful attention to the verification of experimental data. Such verification consists in performing energy and mass balances in the fluid film and coolant sides. Important discrepancies were found in our own experimental data, therefore an extensive study were carried out in order to find the source of such discrepancies. The final main conclusion is that there is a drag of $LiBr$ solution into the water vapor which increases with Re number. This mist flow is minimum (50 PPM) but it is enough in order to contribute in the energy imbalance. Finally a brief introduction about mass spectrometry technique and its application in the influence of the effect of the non-absorbable gases is given.

3.1 Introduction

There are some experimental works reported in the literature related with both vertical and horizontal falling film absorbers. Some of the main works are mentioned below.

Deng and Ma [2] developed an experimental study on the characteristics of an absorber using the $LiBr - H_2O$ solution as working fluid. The authors presented results for a falling film absorber which is made up of 24-row horizontal smooth tubes. They showed that the mass transfer coefficient is increased with the increase of spray density, the heat transfer coefficient is increased only in the small spray density range. This can be used to optimize the future design of absorption machines with falling film absorbers configured with horizontal tubes and $LiBr - H_2O$ as working fluid. Matasuda et al. [6] developed experiments on an absorber and generator of a complete absorption refrigeration machine. In this situation, the design was based in a vertical column made of stainless steel that forms the falling film heat exchanger. The $LiBr - H_2O$ solution at three different mass concentrations (0.4, 0.55 and 0.60 mass fraction of $LiBr$) were used as working fluid. The operation pressure was 1.3 kPa (the pressure for a practical absorber in a real absorption machine). Medrano et al. [7] developed an experimental apparatus for vertical falling film absorption with $LiBr - H_2O$ as working fluid at air-cooling thermal conditions. The control variables for the experimental study were absorber pressure, solution mass flow rate, solution concentration and cooling water temperature. High cooling water temperatures were selected to simulate air-cooling thermal conditions. The parameters considered to evaluate the performance of the absorber were the mass absorption flux, the degree of subcooling of the outlet solution and the falling film heat transfer coefficient. Miller and Keyhan [11] reported a study of the simultaneous heat and mass transfer which was conducted on a vertical falling film absorber to better understand the mechanisms of the heat and mass transfer processes. Thermographic phosphors were used to measure the temperature profile along the length of the absorber test tube. These measures of the local variations in temperature enabled calculation of the bulk concentration along the length of the absorber. Design data and correlations are sparse in the open literature.

In this manuscript an experimental setup which reproduces vertical falling film flow has been designed and built. The $LiBr - H_2O$ solution is used as working fluid. The absorption process is controlled adjusting the following independent variables: solution concentration, solution temperature, cooling water temperature, absorber pressure and solution mass flow. The versatility of the experimental set up allows to manipulate independent variables for producing many experimental data of heat and mass transfer ratios under wide variety of flows/conditions. The mass and heat absorbed are calculated by performing a mass and energy balances, respectively. An unexpected situation has been detected during the experimental data reduction. It has

been proved that water vapor drags some micro drops of $LiBr-H_2O$ solution from the generator to the absorber. This situation generates a kind of mist flow which increases as Re number increases. The amount of such micro-droplets is quantified in function of an overall energy balance taking into account both, liquid and vapor volumetric flows ($\frac{\dot{m}_l}{\rho_l}$, $\frac{\dot{m}_v}{\rho_v}$), and it results in a few quantity of liquid mist ($\approx$ 50 PPM Maximum). The section 3.4.4 explains in detail the study on which this conclusion is reached and the different actions that were taken on order to avoid this undesired situation. According to our knowledge,in the literature nobody mentions this untypical situation, however some authors show important inconsistencies in their experimental data [4, 7, 12, 13].

3.2 Experimental Apparatus

The experimental setup and its main components are shown in Fig. 3.3. The container (V1) is situated at the top of the structure, it has a capacity about 17 liters. (V1) works as a generator, see Fig. 3.2, it uses both an immersion heater of 2 kW and a set of Flexible Silicone Rubber Heaters (OMEGALUX ®) placed directly on the outer surface and with a total heating capacity of 44 kW. Each one of the heat generation sources is governed by an independent PID control, therefore each of them can be operated independently or simultaneously. The difference between using the immersion heater or flexible rubber heaters consists in the heat flux density ($\frac{W}{m^2}$)that provides each of the heaters. The absorber (A) is conformed by a single vertical tube of 0.022 m. of outer diameter. In order to visualize the absorption process, the vertical absorber is situated inside a borosilicate glass cover of $0.315m.$ of diameter and $1.5m.$ of length. Metal plates coupled with flat O-rings of nitrile-butadiene rubber (NBR) are situated both at top and the bottom of the glass container. The vertical absorber tube passes through the upper metal plates, therefore in order to assure the sealing between the tube and the plate, an O-ring (NBR) is placed coupled with a flange. The measuring instruments used are as follows: Resistance Temperature Detectors (RTD), Coriolis mass flow-meters and densimeters (C1,C2,C3) and Pressure Sensors (PS1,PS2). Other components are: Gear pumps (P1,P2,P3,P7), peristaltic pump (P6), vacuum pumps (P4,P5), thermal baths (TB1,TB2), plate heat exchanger (HX). Three different circuits can be distinguished in the experimental apparatus, (i) $LiBr$ aqueous solution, (ii) H_2O vapor and (iii) H_2O coolant. The circuit (i) begins in (V1) where the $LiBr$ aqueous solution is heated and water vapor is generated, temperature in (V1) is controlled by (RTD1). The rich solution is pumped from the generator and it passes across a heat exchanger (HX), where the points 1 and 2 represent the inlet and the outlet of the plate heat exchanger.

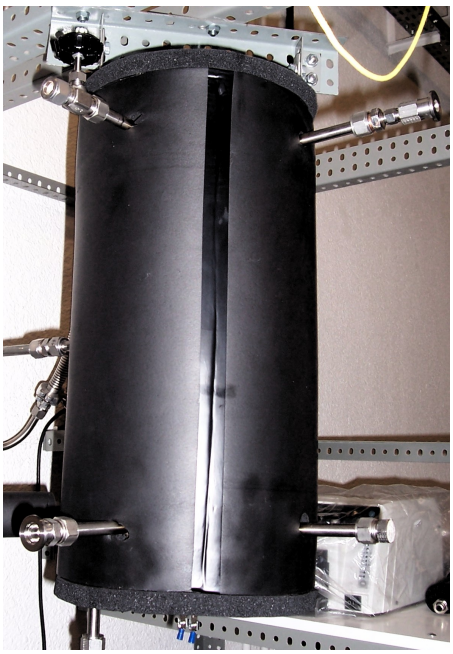

Figure 3.1: Container (V1) (Generator). General View

The inlet mass flow and density are measured by (C1), the rich solution enters at the top of the absorber where is collected in the dispenser which creates the falling film in the outer side of the vertical tube. While the fluid is flowing down, the absorption phenomena is produced. The bottom dispenser picks up poor solution that is sent back to the generator using gear pump (P2). Both mass flow and density of the outlet solution are measured by (C2). The solution passes across (HX), where points $1'$ and $2'$ represent the inlet and the outlet of the plate heat exchanger respectively. The water vapor flows from the top of the generator to the absorber. During the generation process, pump (P7) recirculates the aqueous solution, this is useful in order to maintain an homogeneous temperature inside the generator. Both absorption and generation pressures are measured using the pressure gauges (PS1) and (PS2), respectively. Since concentration is an important factor, it is necessary to adjust it in a accurate way. A peristaltic pump (P6) together with vessels (V2) and (V3) are used to establish concentration, (V3) contains H_2O while (V2) contains $H_2O - LiBr$ solution at high concentration. Using (P6) is possible to increase or decrease concentration in generator by adding either H_2O or $H_2O - LiBr$ solution. Both concentration

of rich and poor solution can be calculated since $c = f(\rho, T)$. Thus (RTD2) and (RTD5) are used for obtaining concentrations while (RTD3) and (RTD4) are used for calculating an energy balance in absorber. Coolant circuit is fed directly by the thermal bath (TB2), where inlet temperature can be adjusted and the coolant fluid is pumped in counter-flow. On the other hand, an energy balance in coolant fluid is performed using (RTD6) and (RTD7). The thermal bath (TB1) is used to adjust inlet temperature of rich solution. During absorption process is a key issue to maintain under control this temperature due to its influence in the absorption process. Finally, the vacuum pumps (P4) and (P5) together with a liquid nitrogen cold trap are used for removing non-absorbable gases. Measuring the temperature of steam is not an easy issue. Using RTD is not the best measurement technique, this due to the vapor tends to condense along the sheath and this causes false measurements. The authors have used an optical sensor (HAM) in order to obtain more accurate measurements.

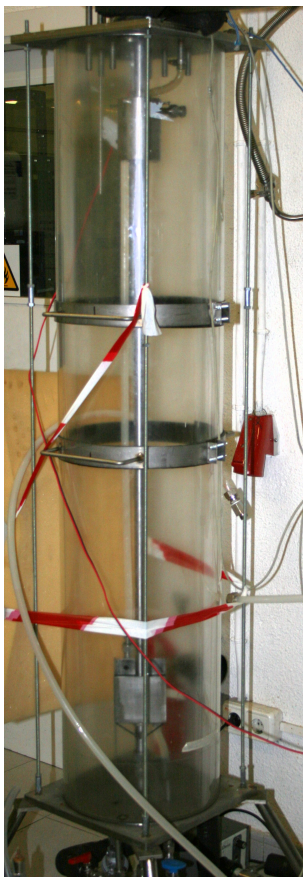

Figure 3.2: Absorber (A). General view

The commercial characteristics and specifications of the experimental set-up are:

i Two magnetically coupled gear pumps of variable velocity (Cole-Parmer E-74011-45), with the following specifications:

- Stainless steel.
- $0.32 - 8.00$ l/min of flow.
- Connection to the process 1/4" NPT.

- 230 VAC 50/60 Hz

ii Two vacuum pump (Telstar model 2G-9 and 2G-6), specifications:

- 9 m^3/h of volumetric flow.
- $8 \cdot 10^{-4}$ mbar of vacuum limit.

iii One thermostatic bath Haake model N3, Type $001 - 5722$.

- 3000 W of heating capacity.
- Temperature Range:5 $^oC \div 80^oC$

iv One thermostatic bath Huber model $CC - 245Wl$.

- 3000 W of heating capacity.
- Temperature range $-45 \div 200$ ^oC.

v Two mass flow meters and densimeters (Micro Motion Elite) reference $CMF025M300NB$.

- Accuracy: $\pm$ 0.15 % of reading in the mass flow
- $0.0005 g/cm^3$ in density with the transmitters Micro Motion Elite reference $RFT9739E4EBB$

vi An absolute pressure sensor (Rosemount 3051S, EMERSON).

- Range 0 to 2000 Pa.
- Accuracy: 0.125 % of reading.

vii An absolute pressure sensor (Rosemount 3051S, EMERSON).

- Range 0 to 10000 Pa.
- Accuracy: 0.125 % of reading.

viii Seven temperature probes $PT100$. Calibrated in order to correct possible bias in the readings.

- Class B.
- accuracy; 1/10 DIN ($\pm 0.03^\circ C$).
- Material: Pyro-Alloy ©

ix An optical Oxygen and temperature sensor.

- Measurement principle: oxygen dependent luminescence (Hamilton ©).

- Temperature range -10 to 130 °C.

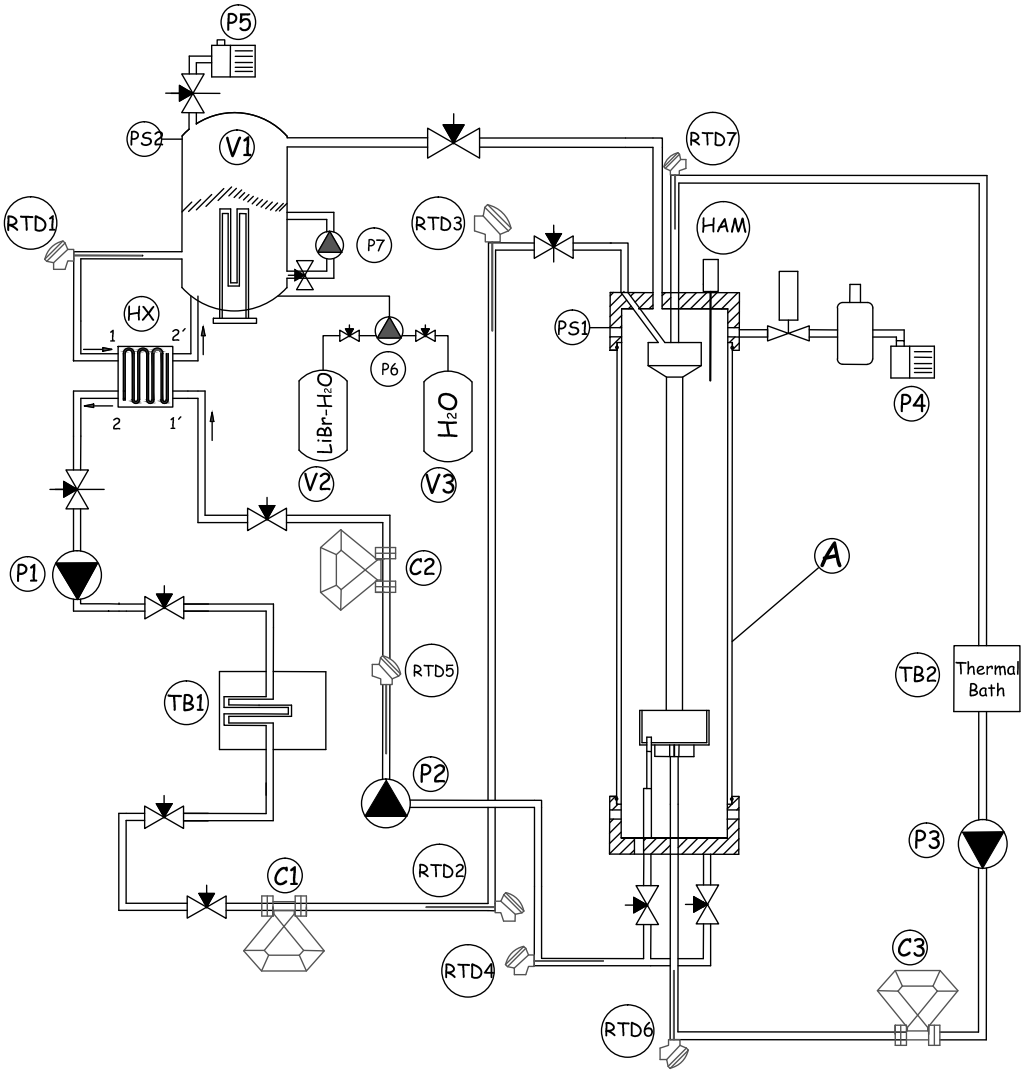

Figure 3.3: Falling Film Experimental Apparatus

3.2.1 Vacuum Requirements

As mentioned in section 2.5, typical pressures in a single effect $LiBr$ absorption machine are sub-atmospheric. The pressure levels associated with $LiBr-H_2O$ are not particularly low (see Fig. 2.3); however, the sensitivity of the absorption performance to leaks is very high, this is because air degrades the efficiency of the absorber and it also generates corrosion. In order to avoid misunderstandings during this manuscript we also refer in terms of absolute pressure units when referring to vacuum pressures (see Fig. 3.4).

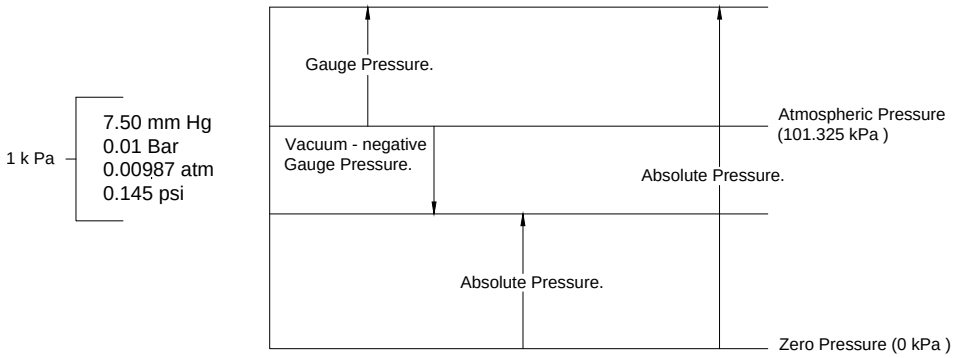

Figure 3.4: Vacuum terminology and units

In order to ensure quality vacuum in the whole system, the main elements were tested individually and then as a whole. The leak test procedure is described below,

i The component to being evaluated is connected with a cold trap and a vacuum pump (see Fig. 3.5). A Pirani gauge is connected into the element to be evaluated. Two valves (V1) and (V2) are situated in each side of the cold trap.

ii The vacuum pump is turned on and the evolution of the Pirani's reading is monitored. A first indication that the system is hermetic is that the Pirani lecture should be in the range of $9 \div 1e^{-2}$ mbar ($9 \div 1$ Pa), if not, there are two possible explanations, i) there is a leak in the system, usually these important leaks are easy to detect since the system do not reach a vacuum lower than $9e^{-1}$ mbar (90 Pa); ii) there is an important quantity of water vapor in the system, in such situation it is recommended to keep the pump working for a while (two or three days). This is helpful in order to remove water vapor from the system.

iii Once the system has reached the range of the $9 \div 1e^{-2}$ mbar the cold trap is loaded using LN_2 (Liquid Nitrogen), then the Pirani's lecture should be in the range $9 \div 1e^{-3}$ mbar($0.9 \div 0.1$ Pa). Next the valve V1 is closed and care must be taken that the cold trap to maintain a minimum level of LN_2. The behavior in the lecture should be a pressure reduction or at least the pressure keeps constant.

iv Next, the valve V2 is closed and the changes in pressure must to be timed for about $1 \div 2$ hours. Then the leak factor needs to be calculated by using the following expression,

$$F = \frac{VP}{t} \tag{3.1}$$

where V is the volume in liters, P is the pressure in mbar and t is the time in seconds. In this work an acceptable leak factor is $F \leq 5e^{-6}\ \frac{mbar\ l}{s}$ ($5e^{-4}\ \frac{kPa\ m^3}{s}$). In the case of having a higher leak factor there are two possible causes, i) there is a micro leak, this kind of leaks are difficult to detect, in the following section we describe some useful procedures in order to lead with such kind of leaks, ii) virtual leaks are present in the system. A virtual leak is a source of gas that's physically trapped within the source system with only a small, very low conductance of the path from the trapped pocket of gas to the system (e.g. an internal weld crack). In the following section some useful techniques for dealing with virtual leaks are described.

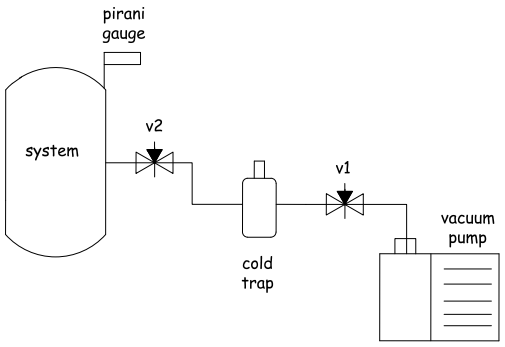

Figure 3.5: Schematic description of the components in the leakage test.

3.2.2 Leaks and virtual leaks

The leaks detection process is not an easy issue, as mentioned in previous section. The leaks can be categorized in two main groups: i) big leaks that are present when the maximum vacuum reached is not below of $1e^{-1}$ mbar; such kind of leaks can be detected by applying pressure in the system (typically He at 5 bar); then by applying soapy water in every weld, joint and fitting it is possible to visualize the source of the leak; ii) micro leaks, when the leak factor is $F > 1e^{-4}\ \frac{mbar\ l}{s}$. Micro-leaks are extremely difficult to find, probably the best way of detecting is using either a commercial leak detector or a mass spectrometry. A rudimentary technique consists in keeping the system in its maximum possible vacuum level, then water is applied in suspected leak areas (weld, joints, etc.) the Pirani's lecture gives a lower pressure due to the water molecule blocks the leaks in question. With respect to virtual leakage, it is a more complicated issue. The virtual leaks are one of the things that need plenty patience to deal with because they are not real leaks, they just seem to be. After spending many hours with leak detector and probing with helium the final conclusion is that there are not any leaks in the system that can be found, but the leak factor is still unacceptable. An useful technique that decreases virtual leaks consist in baking the suspect elements where gas or humidity is trapped. The virtual leaks can be also detected by observing a system's misbehavior. For instance, if performing a leak test from $6 \div 8$ hours of duration, and at a certain point the pressure is stabilized and is it keeps constant, then it is assumed that there is a virtual leak situation, in contrast if pressure increases at all times, then there is a real leak. In conclusion, vacuum is a condition imposed by the nature of the working fluid. It is not an easy topic. Patience and methodology are necessary in order to achieve acceptable vacuum levels. In the case of our experimental apparatus, the whole system was able to operate at an acceptable leak rate of $1.54 \cdot 10^{-5}\ kPa\ m^3\ s^{-1}$.

3.3 Film Breakdown Criterion Experimental Study

An important factor to consider in the falling film formation is to ensure the complete wetting of the tube's surface. The wet area basically depends on two factors, the minimum flow rate per length unit (Γ_{min}) and contact angle θ. The contact angle is given by the equilibrium between surface tension forces and the different interfaces: liquid-vapor, vapor-solid and liquid-solid. When the conditions are not met for a full wetting the film is "broken", then dry patches (dry or stagnation zones on the surface of the tube) are formed. The force balance in the stagnation point is given by [14]:

$$\rho \bar{u}^2 \delta \quad \approx \quad (1 - cos\theta)\sigma \tag{3.2}$$

where $\bar{u} = \frac{\Gamma}{\rho\delta}$ is the average film velocity upstream of the stagnation point. Once a dry patch is formed it will be rewetted if the left side of equation (3.2) prevails. It is interesting to note that if both sides of equation are divided by σ, the left side is the Weber number (We).

In the literature there are several criteria for determining the minimum flow necessary. Hobler [5] considers the total energy (kinetic plus surface) contained in a given streamwise length of broken film. If in this configuration the total energy exhibits a local minimum the author concludes that the film breaks, if the broken configuration exhibits no energy minimum the conclusion is that the continuous film is stable. Bankoff [1] exposed a criterion for the formation of rivulets with shape of segments of a circle. The author assumed equality of the mass flow and the total energy between both configurations, film and rivulets, and further assumed effectively that rivulets can form adjacent to each other with no intervening of dry surface. Mikielewicz and Moszynski [9] present an extension of the previous authors, they consider that the film is broken into rivulets shape of segments of a circle, consistent with a uniform surface tension.

In this manuscript all the experimental tests and the numerical validation are performed assuring that the total area is wetted, therefore it is important to determine what is the minimum Re number that assures such condition. For this reason, an experimental study has been performed combining H_2O and $LiBr$ aqueous solution as working fluids, and steel and copper as tube materials. The table 3.1 summarizes the results.

Working Fluid	Material	Re_{min}	$\theta(rad)$
H_2O	Steel	730	0.87
LiBr	Steel	82	0.439
H_2O	Copper	217	0.307
LiBr	Copper	20	0.829

Table 3.1: Experimental Results for the Film Breakdown Criterion

3.4 Setup of the experimental apparatus and procedure of operation

Once the experimental unit is ready to work and the $LiBr$ aqueous solution was loaded, it is necessary to establish a protocol for starting and operating properly the

experimental unit.

i we recommend leaving the vacuum pumps (P4) and (P5) turned on during a night before to the working day.

ii the absorber and the generator must be isolated hydraulically one to each other before starting.

iii turn on the PID which controls heat sources in the generator. The generator was left running for a period until the pressure reaches a desired value.

iv the thermal baths (TB1) and (TB2) are turned on. (TB2) is set with the inlet coolant temperature, while (TB1) is set about 10° C below the theoretical inlet solution temperature saturation conditions.

v pumps (P1) and (P2) are turned on, and vapor circuit is opened. Then aqueous solution starts to flow and the falling film is formed at the same time that vapor emigrates from generator to the absorber. At this point it is useful to monitoring the following variables: inlet and outlet temperatures for both the primary solution circuit and the coolant fluid, the inlet and outlet solution densities, generator and absorption pressures and inlet solution mass flow.

vi by using the inlet solution temperature and density, the inlet concentration is calculated c_{in}. If c_{in} is not the desired then it can be adjusted using (P6) and either (V2) or (V3).

vii the PID which drives the generation should be adjusted if needed. As the absorption pressure increases P_{abs} the inlet solution temperature needs to be readjusted using (TB1). It is important to keep inlet solution temperature close to the equilibrium during the unsteady state, in this way always there is absorption of water vapor into the falling film solution ($\rho_{in} > \rho_{out}$). Therefore, the system reaches the steady state easily. Once the desired absorption pressure and inlet solution temperature are reached, the inlet mass flow is adjusted.

viii we can consider that a steady-state is reached when none of the variables that govern the absorption performance show important perturbations. The Figs. 3.6, 3.7 and 3.8 shows the steady state behavior for the governing variables in a typical running.

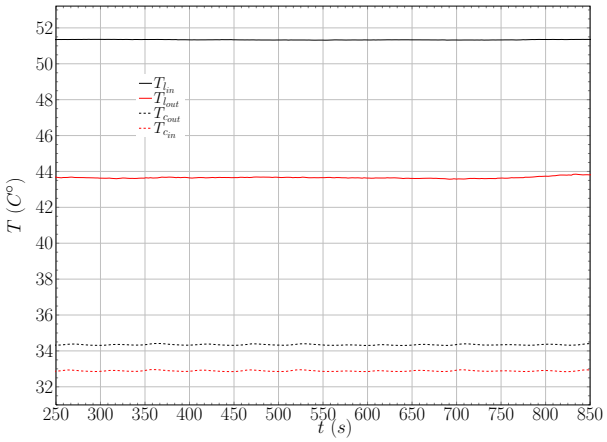

Figure 3.6: Steady state behavior of inlet and outlet solution and coolant temperatures ($T_{l_{in}}$, $T_{l_{out}}$, $T_{c_{in}}$ and $T_{c_{out}}$) during a typical experimental performance

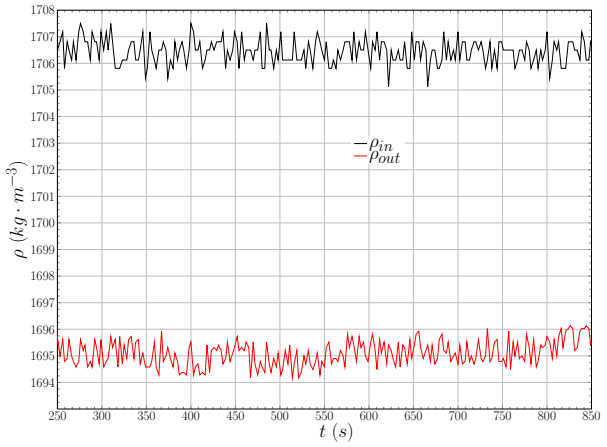

Figure 3.7: Steady state behavior of inlet and outlet solution densities (ρ_{in},ρ_{out}) during a typical experimental performance

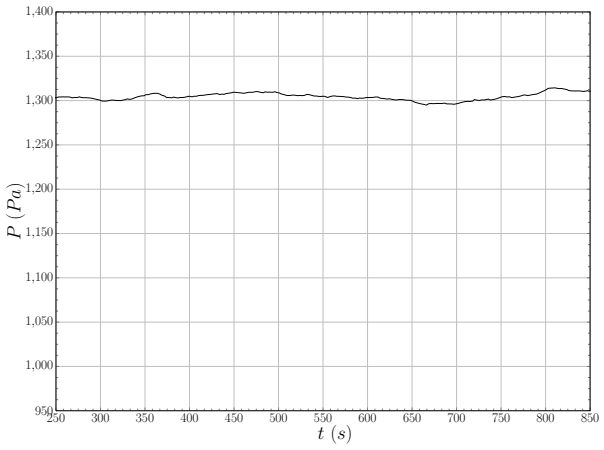

Figure 3.8: Steady state behavior of absorption pressure P_{abs} during a typical experimental performance

3.4.1 Uncertainty Analysis

An uncertainty analysis was conducted in order to determine the maximum error for the thermal load and the mass absorbed. Since the real value of a given measure is not directly known, it is more proper to speak of experimental uncertainty than of experimental error. The uncertainty analysis accounts for both the random error and systematic error. Random errors are related with the lack of repeatability and the precision of the instrument. Systematic errors are biases in measurement which lead to the situation where the mean of many separate measurements differs significantly from the actual value of the measured attribute.

The average uncertainty in the heat load absorber measured in the coolant side ($\dot{Q}_{abs,c}$) was $\pm 6.36\%$. The average uncertainty in the mass absorbed $\dot{m}_{abs}$ for all the reported experimental data were $\pm 10.5\%$.

3.4.2 Data Reduction

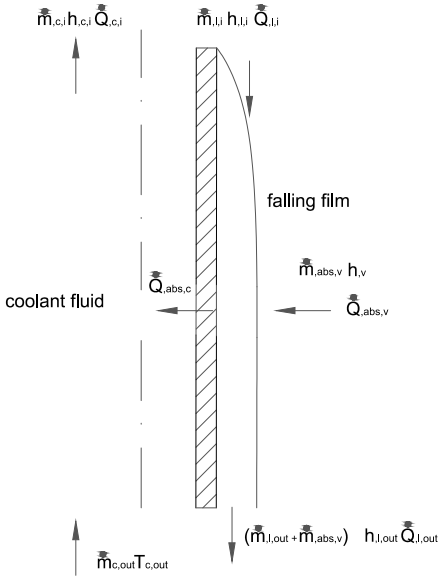

Figure 3.9: Schematic representation of the mass and energy balances in falling film and coolant fluids.

In order to ensure the reliability of the experimental data, energy and mass balances are performed in the $LiBr - H_2O$ falling film (see Fig.3.9):

$$\dot{m}_{l,in}h_{l,i} + \dot{Q}_{abs,v} = (\dot{m}_{l,in} + \dot{m}_{abs,v})h_{l,out} + \dot{Q}_{abs,c} \tag{3.3}$$

$$\dot{m}_{l,in}c_{in} = (\dot{m}_{l,in} + \dot{m}_{abs,v})c_{out} \tag{3.4}$$

In the above equations ($\dot{Q}_{abs,c}$) represents the total heat load which is removed for the coolant side, ($\dot{Q}_{abs,v}$) is energy input through the interface coming from the water vapor and $\dot{m}_{abs,v}$ is the mass of vapor water absorbed by the $LiBr - H_2O$ liquid film.

Using the equation (3.4) the mass absorbed is calculated directly from the experimental data, then using the equation (3.3) the energy input through the interface

($\dot{Q}_{abs,v}$) can be calculated. Moreover the energy input through the interface $\dot{Q}_{abs,v}$ can also being calculated from the following expression:

$$\dot{Q}_{abs,v} \approx \dot{m}_{abs,v} h_v(T_v, P_{abs}) \tag{3.5}$$

The reliability of the experimental data involves to calculate energy input through the interface $\dot{Q}_{abs,v}$ using equation the (3.3) and equation the (3.5). When comparing both quantities the difference should not exceed the uncertainty analysis error.
In section 3.4.4 it is shown some discrepancies between the equations (3.3) and (3.5). This fact has been confirmed in the experimentation by the determination of micro droplets formed by $LiBr - H_2O$. Therefore the equations (3.3) and (3.4) needs to be taken as follows:

$$\dot{m}_{l,in} h_{l,in} + \dot{Q}_{abs,v} + \dot{Q}_{abs,l} = (\dot{m}_{l,in} + \dot{m}_{abs,v} + \dot{m}_{abs,l}) h_{l,out} + \dot{Q}_{abs,c} \tag{3.6}$$

where,

$$\dot{Q}_{abs,v} = \dot{m}_{abs,v} h_v(T_v, P_{abs}) \tag{3.7}$$
$$\dot{Q}_{abs,l} = \dot{m}_{abs,l} h_l(T_{gen}, c_{in}) \tag{3.8}$$
$$\dot{Q}_{abs,c} = \dot{m}_c(h_{c,out} - h_{c,in}) \tag{3.9}$$

The term $\dot{m}_{abs,v}$ refers to the mass absorbed of water vapor, while the term $\dot{Q}_{abs,v}$ refers to the energy flow associated to such mass flux . Analogously, the term $\dot{m}_{abs,l}$ is the total mass of aqueous solution of mist flow that enters in the absorber, while the term $\dot{Q}_{abs,l}$ is the heat input associated to the mist flow. Finally the term $\dot{Q}_{abs,c}$ refers to the total heat load removed by the coolant side.
Mass balance in the film side yields,

$$\dot{m}_{l,in} + \dot{m}_{abs,v} + \dot{m}_{abs,l} = \dot{m}_{l,out} \tag{3.10}$$
$$\dot{m}_{l,in} c_{in} + \dot{m}_{abs,l} c_{in} = \dot{m}_{l,out} c_{out} \tag{3.11}$$

In the equation (3.10) the total mass fluxes in the film side are reflected, while the equation (3.11) represents the $LiBr - H_2O$ mass fluxes. Solving the equations (3.6) - (3.11) it is possible to calculate both mass fluxes, $\dot{m}_{abs_v}$ and $\dot{m}_{abs_l}$. In order

to evaluate the amount of total mist flow that enters in the absorber, the concept of volumetric void fraction is introduced.

$$X = \frac{\frac{\dot{m}_{abs,v}}{\rho_v}}{\frac{\dot{m}_{abs,v}}{\rho_v} + \frac{\dot{m}_{abs,l}}{\rho_l}} \tag{3.12}$$

Due to the liquid density is too large compared to vapor density ($\frac{\rho_v}{\rho l} \approx e^{-6}$), it is expected that the value of X be too small ($\ll 1\%$). For this reason for plotting is used the unit of part per million (PPM) where $1 \cdot 10^4\ PPM = 1\%$.

3.4.3 Driving Potential Estimations

The driving potential effects can be evaluated from both pressure or concentration gradients between liquid-gas interface at theoretical equilibrium conditions of bulk film. In fact both conditions are related to each other since $c_{eq} = f(P_{eq}, T_{eq})$. Therefore, the driving force for mass transfer through the vapor-liquid interface can be expressed as the difference between the partial pressure of water-vapor in vapor phase (which is equal to total pressure if non-absorbable gases are negligible) and the local theoretical equilibrium pressure of $H_2O - LiBr$ aqueous solution at given temperature and concentration. Hence, the higher is the absorption pressure, the greater is the potential for vapor transfer to the falling film. The pressure driving potential is defined as the Logarithmic mean pressure difference.

$$\Delta P_{LMPD} = \frac{\Delta P_1 - \Delta P_2}{ln\left(\frac{\Delta P_1}{\Delta P_2}\right)} \tag{3.13}$$

where, ΔP_1 and ΔP_2 are the difference between the partial pressure of water in the gas phase and the theoretical local equilibrium pressure of the bulk of the liquid at the inlet and the outlet conditions of the absorber.

In mass transfer problems, determination of the interfacial concentration is of paramount importance. However, in absorption equipments is difficult to measure interfacial conditions and for this reason it is very common to define an average mass transfer coefficient using more accessible data. The mass transfer driving potential can be establish as:

$$\Delta c_{LMCD} = \frac{\Delta c_1 - \Delta c_2}{ln\left(\frac{\Delta c_1}{\Delta c_2}\right)} \tag{3.14}$$

where $\Delta c_1 = (c_{in} - c_{eq})$ and $\Delta c_2 = (c_{out} - c_{eq})$, and $c_{eq} = f(T_{l_{av}}, P_{abs})$

3.4.4 Experimental Study of Mist Flow

This subsection is devoted to describe the experiments in which the presence of mist flow is confirmed. Two different experiments have been performed. The table 3.2 shows the difference of the evaluation of the energy input through the interface ($\dot{Q}_{abs_v}$) between the equations (3.3) and (3.5). It is shown that the difference between both quantities increases when *Re* increases. This tendency is repeated in each experimental test. It should be noted that the quantities calculated by the equation (3.3) are higher than values calculated by the equation (3.5), the maximum error is about 32%. It means that there is an *extra* unknown contribution of energy.

Re	$\dot{Q}_{abs_v}$ (W) Eq.(3.3)	$\dot{Q}_{abs_v}$ (W) Eq.(3.5)	Discrepancy(%)
2.201e+02	5.039e+02	3.453e+02	31.48
1.899e+02	5.164e+02	4.207e+02	18.53
1.564e+02	5.141e+02	4.443e+02	13.58
1.294e+02	5.054e+02	4.709e+02	6.98
1.000e+02	4.925e+02	4.825e+02	2.03
8.990e+01	4.645e+02	4.620e+02	0.54

Table 3.2: Comparison of Experimental energy input through the interface ($\dot{Q}_{abs_v}$). Equations (3.3) and (3.5)

In order to discard any measurement errors or sensor faults, a study was carried on in the sensors involved in data reduction. Individual and coupled tests of each circuit (primary and secondary) without generation of vapor were performed, the results obtained matched with the corresponding energy balance. Listed below are the taken actions in order to discard measurement errors or sensor faults:

i An energy balance was performed in the coolant fluid side, (the primary fluid was not present) since there was not heat load ($T_{c_{in}} \approx T_{c_{out}}$), the results of the mass flow-meter ($C3$) were compared against other with the same precision.

ii An energy balance was performed in aqueous solution side (the coolant side was not present). Since there was not neither vapor generation nor heat removed from coolant fluid, then the inlet solution temperature is approximately equal to the outlet solution temperature ($T_{s_{in}} \approx T_{s_{out}}$) and the inlet solution density is approximately equal to the outlet solution density ($\rho_{in} \approx \rho_{out}$).

iii An energy balance was performed in both aqueous solution and coolant side (without generation of vapor). It was established that The inlet solution temperature is is greater than the outlet coolant temperature ($T_{l_{in}} > T_{c_{out}}$). After applying the equations (3.4) and (3.3) the results of the mass absorbed and energy input through the interface $\dot{Q}_{abs,v}$ heat were lower than the measurement errors.

The above points ensure the lack of errors in the experimental measurements or errors in the sensors.

Furthermore it can be concluded that the imbalance arrives when vapor water is generated. Two possible phenomena could explain this extra heat input: i) heat transfer by convection from the water vapor towards the falling film interface; ii) aqueous solution dragged by the generation of water vapor, it creates vapor water containing suspended micro-drops (mist flow) of aqueous solution of $LiBr$.

The point (i) is discarted due to the water vapor density is too low $\frac{\rho_v}{\rho l} \approx 1e^{-6}$, consequently the convective heat transfer coefficient is too low since $Nu = \frac{\alpha_v x}{\lambda_v} \sim Re \cdot Pr$ and $Re = \frac{\rho_v U x}{\mu_v}$, $Pr = \frac{\mu_v cp_v}{\lambda_v}$ therefore the heat transfer can be consider negligible. The authors have made numerical studies that support this fact.

In order to confirm the presence of the mist flow into the water vapor flow, the authors have performed the following experimental test (see Fig. 3.11). Since the mist flow is formed in the generation process, a small vessel with water was installed in the vapor line, between the generator and the absorber. The vapor water enters in the bottom of the vessel, the mist flow mixes into the water and water drops almost pure leaves by the above side of the vessel.

The table 3.3 shows the results of the experimental test. The discrepancy between the equations (3.3) and (3.5) is still present, however there is an important difference in comparison with the table. 3.2. When using the water vessel the energy input through the interface ($\dot{Q}_{abs,v}$) calculated by the equation the equation (3.5) is higher than that one calculated using the equation (3.3) (see at the change of sign). This is due to the mist flow is still present, but it is formed by almost pure water. In other words, when the mist flow is formed by aqueous solution the total mass of H_2O entering through the interface is equal to the sum of the water vapor absorbed, plus the liquid fraction of water that corresponds to the mist flow. However when mist flow is formed by water, the total mass of H_2O is equal to the vapor water absorbed, plus the total of the mist flow. It means that the total quantity of water (either liquid or vapor) entering through the interface is greater when mist flow is formed by pure water but not all the mass absorbed performs the phase change indeed. Therefore it is reflected as a greater mass absorbed (see the equation (3.4)) and as a consequence the $\dot{Q}_{abs,v}$ calculated by the equation (3.5) increases.

A second experimental test has been performed. It consist in a small cylindrical vessel placed in the vapor line between the generator and the absorber. A small sponge of polyurethane is placed in the entrance of the vessel. The purpose is trap

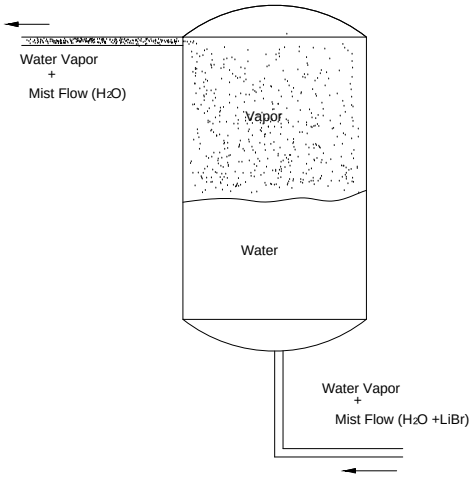

Figure 3.10: Schematic description of the experimental water vessel for mist flow.

Re Number	$\dot{Q}_{abs,v}$(W) Eq.(3.3)	$\dot{Q}_{abs,v}$ (W) Eq.(3.5)	Discrepancy(%)
2.256e+02	3.920e+02	5.916e+02	-33.74
2.006e+02	4.201e+02	5.601e+02	-24.99
1.764e+02	4.401e+02	5.301e+02	-16.97
1.464e+02	4.601e+02	5.201e+02	-11.53
1.164e+02	4.801e+02	5.101e+02	-5.88
8.164e+01	4.711e+02	4.810e+02	-2.04

Table 3.3: Comparison of Experimental energy input through the interface ($\dot{Q}_{abs,v}$) (water vessel). Equations (3.3) and (3.5)

the micro droplet suspended in the vapor flow. After performing the test we found that the filter was displaced from its original position, this due to the high velocities of the vapor. Furthermore small amounts of aqueous solution ($20ml$) were found. This test confirms the presence of mist flow suspended in the vapor flow.

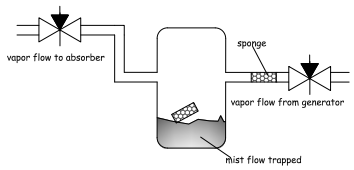

Figure 3.11: Schematic description of the experimetal trap-vessel for mist flow.

In the literature there are some experimental works that reproduce falling film absorbers (vertical or horizontal). However most of them do not divulge enough data in order to evaluate heat and mass balances (see the equations 3.3 - 3.5). Miller, in his Doctoral Dissertations [10] presents experimental data for vertical absorbers in smooth tubes. He presents discrepancies about 30% in the total heat load between a range of Reynolds $200 - 310$. Miller et al. [13] present a technical report for vertical absorbers using advanced surfaces. They reported a range of Re number between 26 to 80, the discrepancies between energy balances are 5.85% ($Re \approx 26$) and 43.46% ($Re \approx 80$). The vapor water that enters into the absorber came directly from the generator. A fact to emphasize is that in both works the heat load calculated using the equation (3.3) is higher than quantity related to the equation (3.5) as in the present work.

On the other hand, Medrano et al. [7, 8] and Hiroshi et el. [4] do not consider in their experimental data reduction the measure of c_{out}, then it is calculated by solving equations the (3.3)-(3.5) in order to find the new value of c_{out} which satisfies such equations. In this way this fact makes not possible to detect any unbalance in energy or mass equations.

After a exhaustive review of the test device configuration, possible explanations for the mist flow could be: i) large differences between generation and absorption pressures; ii) excessive nucleation during the generation procedure; iii) high vapor velocities provoked by high heat fluxes.

The authors have taken actions in order to avoid the above points: i) it has been redesigned the vapor circuit that avoid high pressure drops between generator and absorber; ii) the aqueous solution is recirculated during the generation process, thus the solution temperature inside the generator keeps homogeneous; iii) in order to decrease heat fluxes that leads to high vapor velocities [3], the generation area was increased.

Despite the taken actions, mist flow is still present. However it is possible to calculate both the void fraction and the total mass flow of solution that strains into

the absorber using set of equations (3.6) - (3.11).

An study of the experimental results between the equations (3.3) and (3.5) was performed in order to determine the maximum Re where the mist flow has not influence. The Fig. 3.12 shows the effects of Reynolds number ($Re \approx 90 - 270$) in $\dot{Q}_{abs,v}$ for equation (3.3) (black dots) and equation (3.5) (red dots) at different inlet mass concentrations ($c_{in} \approx 0.57 - 0.61\%$). The experimental results are depicted using the error bar calculated by the uncertainty analysis. An acceptable matching is consider when $Re < 150$.

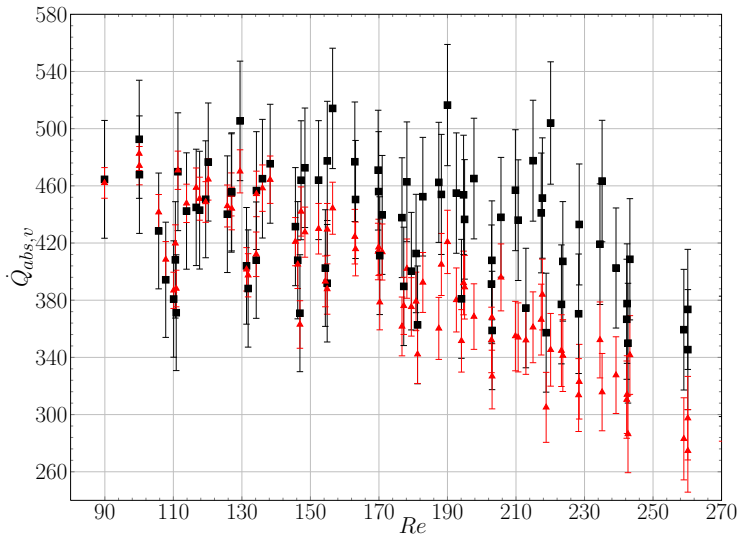

Figure 3.12: Effects of Reynolds number in $\dot{Q}_{abs,v}$ for equation the (3.3) (black dots) and the equation (3.5) (red dots) at different inlet mass concentrations

The Fig.3.13 is analogous to the previous figure, it shows $\dot{m}_{abs,v}$ for the equation (3.4) (black dots) and the equation (3.5) (red dots) at different inlet mass concentrations ($c_{in} \approx 0.57 - 0.61\%$).

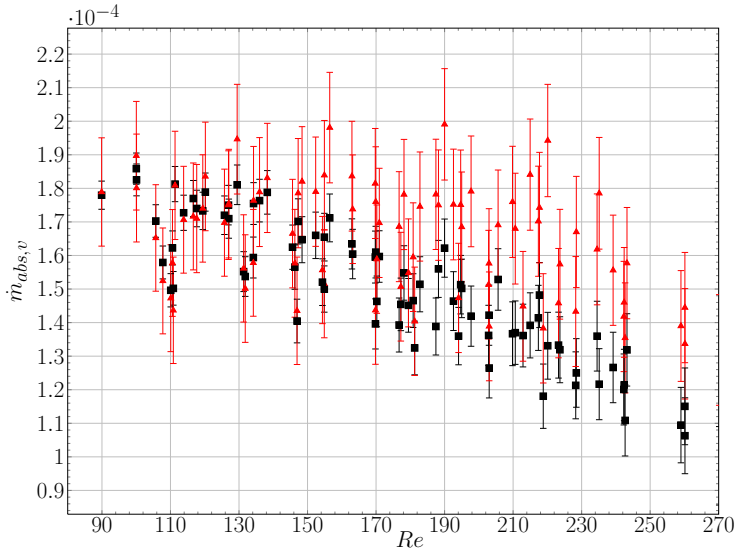

Figure 3.13: Effects of Reynolds number in $\dot{m}_{abs,v}$ for the equation (3.3) (black dots) and the equation (3.5) (red dots) at different inlet mass concentrations

Finally the Fig. 3.14 shows the error rate (%) between the equations (3.3) and (3.5). Errors below 10% are present when $Re < 150$ and are consider acceptable.

3.5 Mass Spectrometry Study

A Mass Spectrometry technology for Residual Gas Analysis (RGA) has been used to evaluate the influence of non-absorbable gases. The RGA technology provide a unique technique into the vacuum environment for contamination monitoring, leak detection and analysis of the species of interest within the vacuum chamber.

The operating principle of the mass spectrometer-RGA is based on the generation of multiple ions from the sample under investigation, it then separates them according to their specific mass-to-charge ratio (m/z), and then records the relative abundance of each ion type.

The first step in the mass spectrometric analysis of compounds is the production of gas phase ions of the sample, basically by means of electron ionization. This molecular ion undergoes a fragmentation. Each primary product ion derived from the molecular ion, in turn, undergoes fragmentation. The ions are separated in the mass

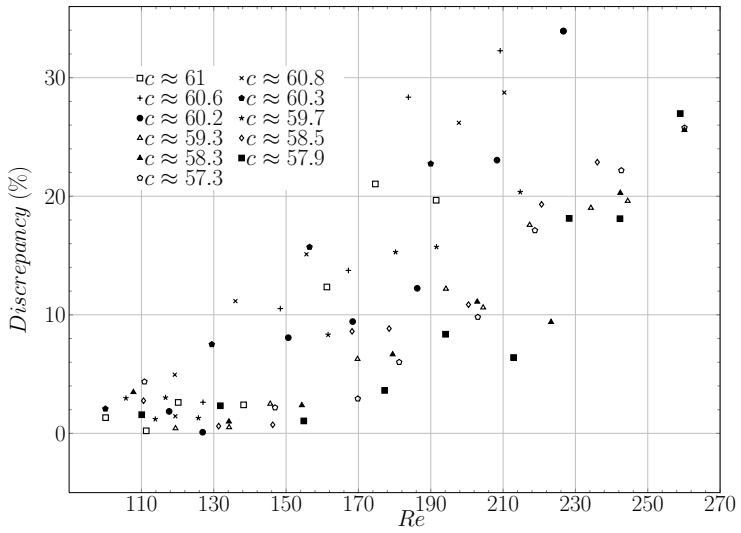

Figure 3.14: Effects of Re in discrepancy rate (%) at different inlet solution mass concentrations

spectrometer according to their mass-to-charge ratio, and are detected in proportion to their abundance. The abundance is presented in a pressure fingerprint (peaks of Torr). A mass spectrum of the molecule is thus produced. It displays the result in the form of a plot of ion abundance versus mass-to-charge ratio. The ions provide information concerning to the nature and the structure of their precursor molecule.

The vacuum residual analysis include:

- The Hydrogen, measured at mass 2.
- The Helium, measured at mass 4, and used as search gas for leak detection.
- The Water vapor, measured at mass 18.
- The Nitrogen and Oxygen, measured at mass numbers 28 and 32, with additional peaks measured for confirmation at mass numbers 14 and 16. The presence of this two elements in a significant signal is often the first indication of a leak.

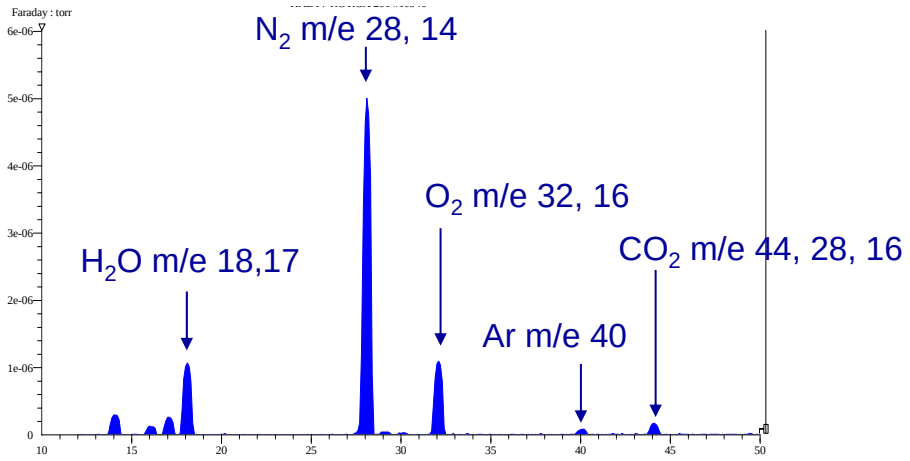

Figure 3.15: Typical peak profile for H_2O and air components at atmospheric pressure.

- The Hydrocarbons and organic compounds, which are measured at several masses. Since this manuscript is focused in non-absorbable gases originated by air leaks, such contaminants are not consider.

Mass spectrometry of RGA does not interpret the acquired data, the information is presented as a profile of mass/charge peaks. The Fig. 3.15 describes a typical cracking pattern for air in atmospheric pressure. The x axis of the graph shows the Atomic Mass Units (AMU). The y axis refers to the relation the relative abundance in units of pressure (Torr). The typical contaminant species in air leaks are shown in peaks: 28 (N_2) confirmed by presence of peak in 14, 32 (O_2) confirmed by presence of peak at 16, 18 (H_2O) is confirmed by peak at 17. In air at atmospheric pressure N_2 and O_2 are the elements with greater presence (78% and 21% respectively), other elements such Ar and CO_2 have much less presence (0.994% and 0.035% respectively). It means that there is a ratio between the N_2 and $O2$ around 5:1, it is expected that similar ratios are found during the mass spectrometry study in the absorber. In order to verify the reliability of the mass spectrometry data a second sensor was used. An optical sensor for dissolved oxygen (Hamilton ©) was used for this purpose. Thus the O_2 percentage can be evaluated by two different methods with a reasonable agreement.

Experimental Procedure

The Fig. 3.16 is a schematic representation of the connection between the mass spectrometer (MS) and the vertical absorber. The absorber and the mass spectrometer are isolated by two valves (V1) and (V2). Before starting the mass spectrometer study it is necessary to tuning the MS, as well as to evaluate the fits and connections between the MS and the absorber. Air intrusion is controlled using a micrometer valve and a small vessel with air at atmospheric pressure.

The first item to evaluate is the vacuum quality inside the quadrupole. In order to obtain the maximum vacuum in the quadrupole is recommended leaving the MS turned on during a night before to the test day. The minimum vacuum recommended by the manufacturer is $1e^{-4}$ Torr (0.0133 Pa), the authors however reached lower values about $8.0e^{-7}$ Torr (0.0001066 Pa). Since there is not possible to achieve a perfect vacuum, it is always expected to find small quantities of air components inside the quadrupole. A Mass spectrometry was performed in the quadrupole (Valves V1 and V2 are fully closed). The values of the partial pressure of each element are of the following orders of magnitude: $N_2 \approx 1{\times}10^{-8}$ torr, $O_2 \approx 1{\times}10^{-10}$ torr, $Ar \approx 1{\times}10^{-10}$ torr, $H_2O \approx 1 \times 10^{-8}$ torr.

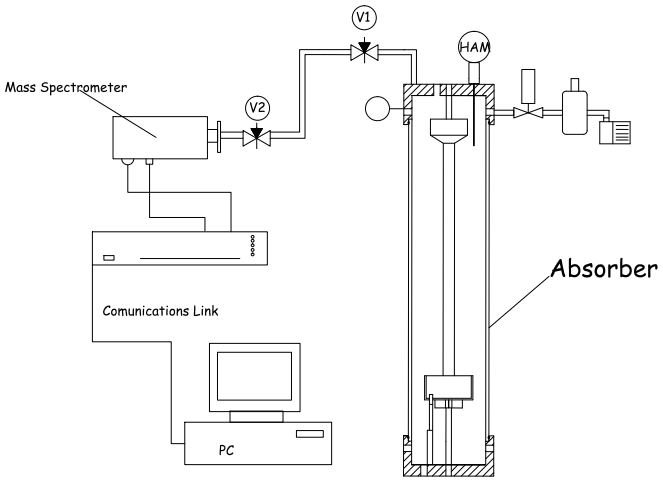

Figure 3.16: Schematic representation of the mass spectrometry experimental setup.

The same procedure is repeated with the valve (V2) fully open. In this way it

is possible evaluate the fits and connections between (V1) and (V2). The values of the partial pressure of each element should be the same as in the quadrupole. If not so, a possible leak could exist. Once the previous test has been performed, then it is possible to perform an mass spectrometry study in the absorber. Listed below is the protocol for performing correctly this task:

- Protocol implementation of the Mass Spectrometer.
  - Turn on the backing vacuum pump.
  - After 30 minutes, turn on the turbo pump and wait until it reaches its limit velocity (about 27000 RPM).
  - Turn on the Penning pressure sensor (only when the turbo pump is in its top speed).
  - Wait until reach the desire pressure in the quadrupole.
  - Turn on the Mass Spectrometer Control Unit (MSIU).
  - Turn on the MASsoft Professional software.
- Protocol implementation for the mass spectrometer study.
  - Reach a steady state in the falling film absorption experiment.
  - Open (V2) and perform a mass spectrometry in order to obtained an background cracking pattern for the quadrupole and connections.
  - Perform air intrusions into the absorber (if required).
  - Open valve (V1).
  - Monitor the results until the partial pressures of the components make steady.
  - Close valve (V1).

The RGA is an powerful tool and it provides excellent stability for mass peak measurements.

Conclusions

An experimental unit which reproducing falling-film absorption in vertical tubes has been designed, built and tested. An mass spectrometer for RGA has been set up and tested in order to assure high quality experimental data. The following conclusions are highlighted:

- A verification of the experimental data was carried out by performing energy and mass balances. Important imbalances were found that augmented as Re number is increased.

- After a detailed study it was concluded that there is a quantity of $LiBr - H_2O$ in form of micro drops (mist flow) that is dragged from the generator.
- The principal cause of mist flow generation is the way as the heat flow is applied in the generator. In this experiment two different ways were used for providing heat fluxes in the generator: i) an immersion electrical heater (2 kW); ii) a set of Flexible Silicone Rubber Heaters (44 kW). In both cases mist flow was present. High heat fluxes are related high vapor velocities ([3]).
- The final solution for eradicating the mist flow involves the redesign of the generator. The main key lies in the quantity of heat per unit of area that is applied during the generation of the water vapor.
- The equations for the data reduction have been modified in order to consider the mass and heat contribution of such mist flow. In this way the quantity of mist flow can be evaluated and using the equation (3.12) is possible quantify it.
- An evaluation and start up of Mass Spectrometer for Residual Gas Analysis has been developed. Mass spectrometry is a tool that allows to evaluate the amount of air which the absorber contains, among other species. The measurement has been checked against a optical oxigen sensor, with a reasonable agreement.

Nomenclature

c	mass fraction concentration
h	enthalpy, $J\ kg^{-1}$
$\dot{m}$	mass flow, $kg\ s^{-1}$
P	pressure, Pa
$\dot{Q}$	heat rate, W
T	temperature, K
u	velocity profile x axis direction, $m\ s^{-1}$
X	void fraction

Greek symbols

ΔP	pressure driving potential, Pa
ΔC	concentration driving potential
δ	film thickness m
ρ	density $m^3\ kg^{-1}$

σ	surface tension $N\ m^{-1}$

Dimensionless Groups

Fr	Froud Number, $Fr = \frac{g\delta_o}{V_o^2}$
Re	Reynolds Number, $Re = \frac{4\Gamma}{\mu}$
We	Weber Number, $We = \frac{\rho V_o^2 \delta_o}{\sigma}$

Subscripts

abs	absorption
av	average
gen	generation
in	inlet conditions/ related to inner diameter
l	liquid fluid
c	coolant fluid
eq	equilibrium
in	inlet conditions/ related to inner diameter
out	outlet conditions/related to outer diameter
sat	saturation conditions
t	total
if	interface conditions
l	liquid fluid
v	vapor fluid
w	wall solid tube

Bibliography

[1] S. G. Bankoff. Minimum Thickness of a Draining Liquid Film. *International Journal of Heat and Mass Transfer*, 14(12):2143–2146, 1971.

[2] S. M. Deng and W. B. Ma. Experimental studies on the characteristics of an absorber using LiBr/H2O solution as working fluid. *International Journal of Refrigeration*, 22(1999):293–301, 1998.

[3] K. E. Herold, R. Radermacher, and S. A. Klein. *Absorption Chillers and Heat Pumps*. CRC Press, 1996.

[4] T. Hiroshi, Y. Hikari, and H. Hiroshi. Vapor Absorption by LiBr Aqueous Solution in Vertical Smooth Tubes. *International Journal of Refrigeration*, 26(2003): 659–666, 2003.

[5] T. Hobler. Minimum Thickness of a Draining Liquid Film. *Chemia stosowana*, 2B(-):145–159, 1964.

[6] A. Matasuda, K. H. Cjoi, and T. Kawamura. Effect of Pressure and Concentration on Performance of a vertical falling-film type of absorber and generator using lithium bromide aqueous solutions. *International Journal of Refrigeration*, 18(8):538–542, 1994.

[7] M. Medrano, M. Bourouis, and A. Coronas. Absorption of water vapour in the falling film of water-lithium bromide inside a vertical tube at air-cooling thermal conditions. *Industrial and Engineering Chemical Fundamentals*, 31(2002):891–898, 2001.

[8] M. M. Medrano. *Desarollo de un Absorbedor Tubular Vertical Enfriado por Aire para un Climatizador de Absorción de Agua-Bromuro de Litio*. PhD thesis, Universitat Rovira i Virgili, 2000.

[9] J. Mikielewicz and J. R. Moszynski. Minimum Thickness of a Liquid Film Flowing Vertically Down a Solid Surface. *International Journal of Heat and Mass Transfer*, 19(7):771–776, 1976.

[10] W. A. Miller. *The Experimental Analysis of Aqueous Lithium Bromide Vertical Film Absorption*. PhD thesis, University of Tennessee, 2000.

[11] W. A. Miller and M. Keyhan. The Correlation of Simultaneous Heat and Mass Transfer Experimental Data for Aqueous Lithium Bromide Vertical Falling Film Absorption. *Journal of Solar Energy Engineering*, 123(2001):30–42, 2001.

[12] W. A. Miller and H. Pérez-Blanco. Vertical-Tube Aqueous LiBr Falling Film Absorption Using Advanced Surfaces. In *Proceedings of the International Absorption Heat Pump Conference 1993*, pages 185–202, 1993.

[13] W. A. Miller, H. Pérez-Blanco, and V. Patnaik. Advanced Surfaces for Vertical Tube Absorbers. Final Report to the Gas Research Institute. Technical report, Oak Ridge National Laboratory, 1993.

[14] W.M. Rohsenow, J.P. Hartnett, and E.N. Ganic. *Handbook of Heat Transfer Fundamentals*. McGraw-Hill, 1985.

Chapter 4

Quick Calculation One Dimensional (1-D) Empirical Model

ABSTRACT

This chapter describes an 1-D analytical model based on the resolution of the conservation equations (mass, species and energy) that constitute three ordinary differential equations. Their resolution allows to calculate solution and coolant temperature distributions, and mass flux absorbed along the falling film. Extra equations are used for calculating bulk and interface mass concentrations, as well as interface temperature distribution. This model uses empirical information for calculating the heat and mass transfer coefficients. The main advantage of this model is the savings in CPU computation time.

4.1 Introduction

There have been several efforts to develop simplified-empirical models for design/prediction of heat and mass transfer in falling-film absorbers [1, 4, 8–11, 13]. A 1-D model similar to the one proposed by Patnaik [8], Patnaik et al. [9], Pearson [10] has been developed, with the difference that in this work axial heat conduction in the tube wall has been taken in consideration (for further details see appendix A). The mathematical model is constructed from two energy balances and a mass balance in the coolant and falling film sides. The solution of the ordinary differential equations yields in temperature distribution for coolant and falling film side as well as mass transfer gradients. Runge-Kutta methodologies are used to perform numerical integration. All the empirical information for getting mass and heat transfer coefficients are extracted from literature. The usefulness of this model can be appreciated in the fact of saving time on CPU calculations.

4.2 Mathematical model and numerical implementation

Three independent equations are obtained for solving three dependent variables ($T_l, T_c, \dot{m}_l$). The following hypotheses have been assumed:

i Steady-state conditions.

ii One-dimensional problem: only variation of flow properties in the axial direction.

iii The thermophysical properties are assumed constant.

iv The falling film flow is laminar, or wavy-laminar.

v The interface is under thermodynamic equilibrium conditions.

vi The solution temperature profile is linear with respect to the transverse coordinate.

vii The vapor-side resistance to mass transfer is negligible.

viii The vapor drag on the falling film is negligible.

ix The heat transfer from the liquid phase to the vapor phase is negligible.

x The vapor mass absorbed is very small compared to solution flow, as established by empirical studies.

xi The effect of the axial heat conduction along the tube wall is considered.

4.2.1 Governing Equations

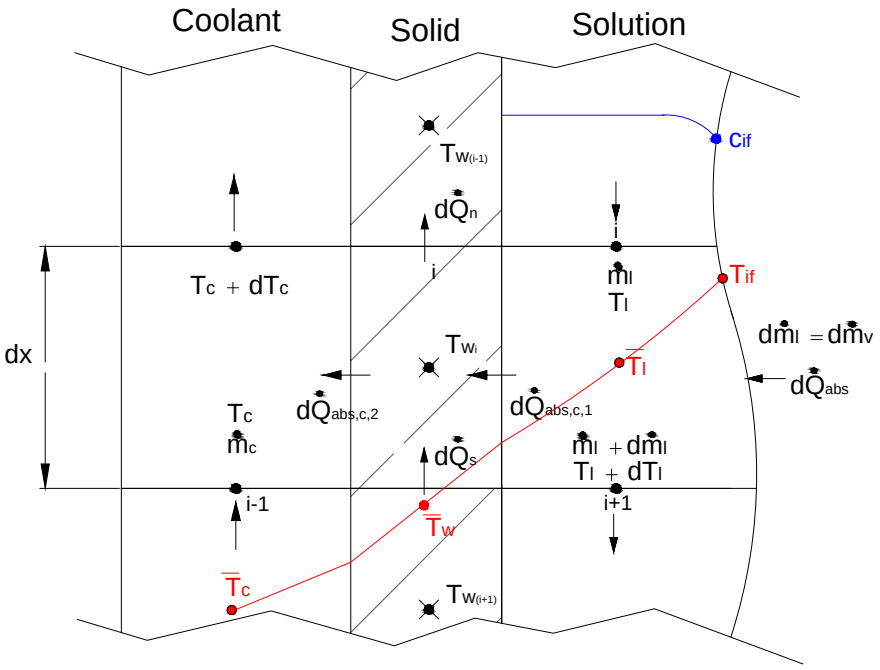

Figure 4.1: Schematic control volume of the liquid film, solid and coolant domains. Typical temperature profiles

The Fig. 4.1 represents an infinitesimal control volume of the domain (aqueous solution, solid and fluid coolant). The energy balances in the solution and coolant fluids are related through wall temperature T_w. The total heat flux is dissipated by the coolant fluid. It is also known as heat load ($d\dot{Q}_c$). Also, it can be seen the heat flux that passes through the film interface is that labeled as energy input through the interface ($d\dot{Q}_{abs}$), and it is closely related with the mass absorbed ($\dot{m}_{abs}$).

The energy balances in solution and coolant yields in equations (4.1) and (4.2) respectively, while mass balance in the interface brings to equation (4.3). A dimensionless form is obtained using coolant outlet properties.

$$\frac{dT_l^*}{dx^*} = \frac{1}{M_l^*}\left[-\frac{d\dot{m}_l^*}{dx^*}(h_v^* - c_{p_l}^* T_l^*) + \alpha_l^*(T_l^* - T_w^*)\right] \tag{4.1}$$

$$\frac{dT_c^*}{dx^*} = -\alpha_c^*(T_c^* - T_w^*) \tag{4.2}$$

$$\frac{d\dot{m}_l^*}{dx^*} = \frac{2\pi r_{out} L}{\dot{m}_c}\frac{ShD_l}{\delta}\rho_l(c_l - c_{if}) \tag{4.3}$$

The bulk solution concentration is defined by:

$$c_l = \frac{\dot{m}_{l_i}}{\dot{m}_l} \tag{4.4}$$

Since interface is under equilibrium, concentration can be obtained from an empirical correlation [6], then:

$$c_{if} = f(T_{if}, P_{abs}) \tag{4.5}$$

Then, interfacial temperature is obtained by making a energy balance in interface. Assuming a linear profile, its expression results in:

$$T_{if} \quad = \quad T_l + \frac{h_{abs}^* M_c}{\pi L \lambda} \quad \frac{\delta}{4(r_{out} + \delta)} \quad \frac{d\dot{m}_l^*}{dx^*} \tag{4.6}$$

The coolant and liquid solution fluids entrance conditions constitute the following boundary conditions:

$$x^* = 0, \begin{cases} T_l^* = T_{if}^* = T_{l,in}^* \\ c_l^* = c_{if}^* = c_{l,in}^* \\ \dot{m}_l^* = \dot{m}_{l,in}^* \end{cases} \tag{4.7}$$

$$x^* = 1, \quad T_c^* = T_{c,in}^* \tag{4.8}$$

In the above equations the superscript * denotes dimensionless quantities. M_c and M_l represent the heat capacity of liquid film and coolant fluid respectively (see appendix A for further details).

The equations (4.1), (4.2), (4.3), (4.5), (4.6) and their boundary conditions form a first-order ordinary differential equations system. The empirical information is obtained from literature. Three parameters are needed, the heat transfer coefficient in coolant side α_c, [3], the heat and mass transfer coefficients in solution side α_l [5, 12] and the mass transfer coefficient κ_l [14]. Further details about the mathematical formulation and about the heat and mass transfer phenomena are included in appendix A.

Solid domain

Inasmuch as heat conduction along the tube is being taken into consideration, the solid domain is discretized in control volumes. An energy balance over each solid part of the tube is therefore performed. The energy balance takes into account the heat exchanged with the coolant fluid ($\dot{Q}_{abs,c,1}$) and the heat transferred from the fluid flow of solution ($\dot{Q}_{abs,c,2}$). The discretized energy equation in its steady state form is applied at each solid control volume and it is expressed as follows:

$$\lambda \left(\frac{\partial T}{\partial x}\right)_s - \lambda \left(\frac{\partial T}{\partial x}\right)_n = \dot{q}_{abs,c,1}\pi d_{out}\Delta x - \dot{q}_{abs,c,2}\pi d_{in}\Delta x \tag{4.9}$$

The derivative approaches as,

$$\lambda \left(\frac{\partial T}{\partial x}\right)_s - \lambda \left(\frac{\partial T}{\partial x}\right)_n \approx \lambda \frac{T_{w,i} - T_{w,i-1}}{\Delta x} S - \lambda \frac{T_{w,i+1} - T_{w,i}}{\Delta x} S \tag{4.10}$$

In order to calculate the heat fluxes $\dot{q}_{c,1}$ and $\dot{q}_{c,2}$ empirical information is used (see appendix A). The set of algebraic equations of the solid domain can be solved by means of a node-by-node iterative procedure (Gauss-Seidel) [2] or a direct method (TDMA) [7].

4.2.2 Resolution Procedure

The set of dimensionless equations are discretized in the domain from $x^* = 0$ up $x^* = 1$. A fourth-order Runge-Kutta scheme is used to perform the numerical integration. When solving the set of equations the temperature fields in solution (T_l)

and coolant side (T_c) are obtained as well as the absorbed mass flow rate ($\dot{m}_l$). The algorithm resolution is as follows:

1. A guessed field temperature in wall tube T_w and outlet coolant temperature $T_{c,out}$ are assumed.
2. The empirical information is calculated, α_c, α_l and κ_l.
3. Runge-Kutta scheme is applied to equations (4.1), (4.2), (4.3) and interfacial equations (4.5), (4.6) are solved to obtain T_{if} and c_{if}.
4. Check if $\left|\frac{T_{if}-T_{if}^{o}}{T_{if}}\right| \leq \varepsilon$ and $\left|\frac{c_{if}-c_{if}^{o}}{c_{if}}\right| \leq \varepsilon$. If so, carry on to the next row, if not, back to the point 3.
5. Check if $\left|T_{c,Nx} - T_{c,in}\right| \leq \varepsilon$. If so, carry on to calculate solid wall, if not, back to point 1. to calculate a new value of $T_{c,out}$ using bisection method.
6. The solid wall tube temperature is calculated using equation (4.9).
7. Check if $\left|\frac{T_w-T_w^{o}}{T_w}\right| \leq \varepsilon$. If so, then finish the algorithm , if not then $T_w = T_w^{o}$ and back to the point 2.

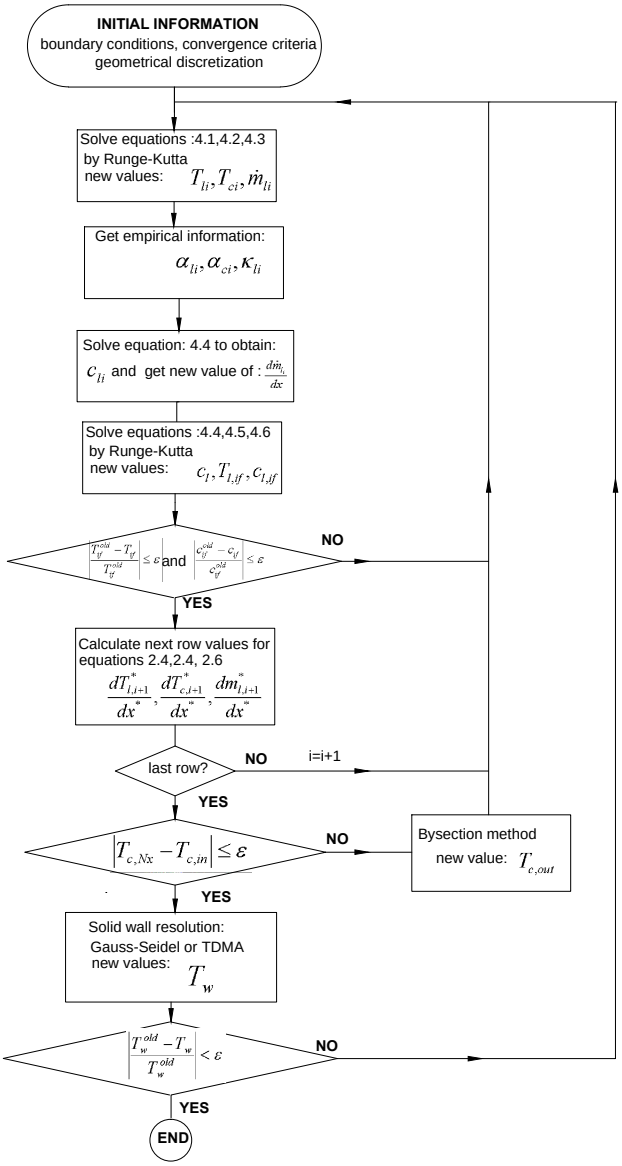

Figure 4.2: Resolution algorithm for the 1-D mathematical model.

4.3 Numerical verification

In order to verify the the behavior and the quality of the numerical solutions, a numerical verification study has been performed. The aspects to be evaluated into this section are the following:

1. Programing errors.- There are errors caused in the implementation of the code. Since the evaluation of the programing errors is necessary a comparison against other numerical model as a reference is carried out. This test will be performed in chapter 5.
2. Convergence errors.-These kind of errors are related with the iteration procedures. It is important to establish a convergence criteria that ensures both, asymptotic results and reasonable number of iterations. A numerical study is performed in order to evaluate the convergence criterion and its influence in the numerical results.
3. Discretization errors.- Such kind of errors are the truncation error of the approximation of the partial derivatives in the differential equation plus any errors introduced by the numerical treatment of the boundary conditions. In order to evaluate them a mesh interdependency analysis is performed.

The characteristics of the benchmark case considered are shown in the table 4.1.

Geometry	
Outer Diameter Tube (m)	0.022
Inner Diameter Tube (m)	0.018
Length Tube (m)	1.0
Working Conditions (LiBr Aqueous solution)	
Inlet solution mass flow ($kg \cdot s^{-1}$)	$7.5e^{-3}$ ($Re \approx 100$)
Inlet temperature (°C)	saturation conditions (T_{sat})
Inlet LiBr concentration (% $LiBr$)	60
Absorption pressure (Pa)	1300
Working Conditions Coolant Side	
Inlet solution mass flow ($kg \cdot s^{-1}$)	$11.9e^{-1}$ ($Re \approx 6000$)
Inlet temperature (°C)	30

Table 4.1: Geometry and working conditions for the reference case.

4.3.1 Convergence Errors

There are two different iteration procedures (see Fig.4.2). The first criterion (ε_1) is the absolute error between the value of the inlet coolant temperature $T_{c,in}$ (known

working condition), and the calculated value $T_{c,Nx}$ which is consequence of the bi-section calculation of the $T_{c,out}$. The second criterion (ε_2) is the maximum absolute error in the wall tube field temperature between two consecutive iterations. The table 4.2 shows the results for both convergence criteria for the 1-D dimensional empirical model. In this study the data computed are, by order, heat load calculated in the film side ($\dot{Q}_{abs,c,1}$), heat load calculated in the coolant side ($\dot{Q}_{abs,c,2}$), mass absorbed, outlet mass concentration and outlet solution temperature. Asymptotic results are achieved when the convergence criteria $\approx 5.0e^{-7}$.

ε_1	ε_2	$\dot{Q}_{abs,c,1}$ (W)	$\dot{Q}_{abs,c,2}$ (W)	$\dot{m}_{abs}$ $(kg \cdot s^{-1})$	c_{out} $(\%LiBr)$	T_{out} $(^{\circ}C)$
1.0 e^{-2}	1.0 e^{-2}	6.046483e+02	4.236778e+02	2.457211E-04	5.809659e+01	3.849081e+01
1.0 e^{-3}	1.0 e^{-2}	6.041074e+02	4.232659e+02	2.456913E-04	5.809682e+01	3.820638e+01
1.0 e^{-4}	1.0 e^{-2}	6.041386e+02	4.232811e+02	2.459349e-04	5.809672e+01	3.820726e+01
1.0 e^{-6}	1.0 e^{-2}	6.041363e+02	4.232801e+02	2.457037E-04	5.809672e+01	3.820679e+01
1.0 e^{-3}	1.0 e^{-3}	5.927012e+02	5.659630e+02	2.178064e-04	5.830834e+01	3.924360e+01
1.0 e^{-6}	1.0 e^{-3}	5.926356e+02	5.659033e+02	2.177994e-04	5.830840e+01	3.920860e+01
5.0 e^{-7}	1.0 e^{-3}	5.926356e+02	5.659033e+02	2.175848E-04	5.830840e+01	3.920860e+01
1.0 e^{-5}	1.0 e^{-5}	5.912754e+02	5.902674e+02	2.130508e-04	5.834429e+01	3.932839e+01
1.0 e^{-6}	1.0 e^{-5}	5.915407e+02	5.902670e+02	2.128376E-04	5.834429e+01	3.932819e+01
1.0 e^{-7}	1.0 e^{-5}	5.912751e+02	5.902670e+02	2.128376E-04	5.834429e+01	3.932819e+01
5.0 e^{-7}	5.0 e^{-7}	5.912789e+02	5.904334e+02	2.128121E-04	5.834448e+01	3.932779e+01
1.0 e^{-7}	1.0 e^{-7}	5.912793e+02	5.904040e+02	2.128113E-04	5.834448e+01	3.932774e+01

Table 4.2: Convergence study for the 1D empirical model algorithm depending on ε_1 (absolute error between the value of the inlet coolant temperature $T_{c,in}$) and ε_2 (maximum absolute error in the wall tube field temperature between two consecutive iterations).

4.3.2 Truncation Errors (Discretization)

The table 4.3 shows the results for the discretization error's study. The domain is transformed into the dimensionless x coordinate ($x^* = \frac{x}{L}$). The data showed in the table 4.3 are as follows: The number of grid points (N_x), the length of the calculations steps in the x direction (Δx), heat load in film side ($\dot{Q}_{abs,c,1}$), heat load in coolant side ($\dot{Q}_{abs,c,2}$), mass absorbed ($\dot{m}_{abs}$), outlet mass concentration (c_{out}) and outlet temperature (T_{out}). Notice that both magnitudes of heat load become equal when the asymptotic values are reached.

N_x	Δx (m)	$\dot{Q}_{abs,c,1}$ (W)	$\dot{Q}_{abs,c,2}$ (W)	$\dot{m}_{abs}$ $(kg \cdot s^{-1})$	c_{out} $(\%LiBr)$	T_{out} $(^{\circ}C)$
50	0.02	5.876054e+02	5.789527e+02	2.112247e-04	5.838776e+01	3.936634e+01
100	0.01	5.893396e+02	5.835991e+02	2.120783e-04	5.836592e+01	3.934681e+01
200	$5e^{-3}$	5.903316e+02	5.868374e+02	2.125639e-04	5.835437e+01	3.933648e+01
400	$2.5e^{-3}$	5.908846e+02	5.888999e+02	2.128335e-04	5.834834e+01	3.933117e+01
600	$1.66e^{-3}$	5.910992e+02	5.897070e+02	2.129368e-04	5.834622e+01	3.932935e+01
800	$1.25e^{-3}$	5.912084e+02	5.901304e+02	2.129911e-04	5.834514e+01	3.932840e+01
1000	$1.0e^{-3}$	5.912789e+02	5.904002e+02	2.130253e-04	5.834448e+01	3.932779e+01
1500	$6.66e^{-3}$	5.913843e+02	5.907827e+02	2.130768e-04	5.834355e+01	3.932697e+01
2000	$5.0e^{-4}$	5.914400e+02	5.909792e+02	2.131051e-04	5.834307e+01	3.932653e+01
2500	$4.0e^{-4}$	5.914782e+02	5.911065e+02	2.131243e-04	5.834276e+01	3.932621e+01
3000	$3.33e^{-4}$	5.915040e+02	5.911917e+02	2.131368e-04	5.834256e+01	3.932604e+01

Table 4.3: Results for different discretizations in the 1D-Dimensional empirical model

4.4 Conclusions

A 1-D dimensional empirical model based on the resolution of the falling film absorption in vertical absorbers based on the resolution of a set of ordinary differential equations is presented. This model solves temperature profiles for falling film (interfacial and bulk), wall solid and coolant fluid side temperatures, mass concentrations profiles (interfacial and bulk) and the heat and mass transfer rates in absorption phenomena using empirical information in the form of heat and mass transfer coefficient. The model shows an interesting option as saving computation time is concerned. A numerical verification study has been performed.

Nomenclature

A	area, m^2
c_p	specific heat capacity, $J\ kg^{-1}\ K^{-1}$
c	$LiBr$ mass fraction concentration
D	mass diffusivity, $m^2 s^{-1}$
d	tube diameter, m
h	specific enthalpy, $J\ kg^{-1}$
L	tube length, m
M	heat capacity, $W\ K^{-1}$
$\dot{m}$	mass flow , $kg\ s^{-1}$
P	pressure, Pa
$\dot{Q}$	heat rate, W
r	tube radius, m

S	cross section, m^2
T	temperature, K
x	coordinate, m

Greek symbols

α	heat transfer coefficient, $W\ m^{-2}\ K^{-1}$
δ	film thickness, m
κ	mass transfer coefficient $m\ s^{-1}$
ε	convergence accuracy criterion
λ	thermal conductivity, $W\ m^{-1}\ K^{-1}$
ρ	density, $kg\ m^{-3}$

Dimensionless Groups

Sh	Sherwood Number, $Sh = \frac{\kappa\delta}{D}$

Subscripts

abs	absorption
c	coolant fluid
Nx	number of grid points in x direction
n	north direction
i	grid position in the x direction
if	interface conditions
in	inlet conditions, inner
l	liquid phase in LiBr solution
out	outlet conditions, outer
s	south direction
v	vapor phase
w	wall solid tube

Superscripts

$*$	dimensionless quantity
old	previous step value

Bibliography

[1] I. Fujita and E. Hihara. Heat and Mass Transfer Coefficients of falling-film absorption process. *International Journal of Heat and Mass Transfer*, 48(2005): 2779–2786, 2004.

[2] C. F. Gerald. *Applied Numerical Analysis*. Addison-Wesley, 1978.

[3] V. Gnielinski. New equations for heat and mass transfer in turbulent pipe and channel flow. *International Chemical Engineering*, 16(2):359–368, 1976.

[4] D. S. Kim and C. A. Infante Ferreira. Air-Cooled Solar Absorption Air Conditioning. Technical report, Faculty of Design, Construction and Production, Mechanical Engineering and Marine Technology, 2005.

[5] J. G. Knusden. *Heat Transmissions. In Chemical Enginners'Handbook*. McGraw-Hill, 1973.

[6] L. McNeely. Thermodynamic Properties of Aqueous Solutions of Lithium Bromide. *ASHRAE Transactions*, 85(1):413–434, 1979.

[7] S. V. Patankar. *Numerical Heat Transfer and Fluid Flow*. Hemisphere Publishing Corporation, 1980.

[8] V. Patnaik. *Combined Heat and Mass Transfer in Wavy-Film Absorption*. PhD thesis, Pennsylvania State University, 1994.

[9] V. Patnaik, H. Pérez-Blanco, and W. A. Ryan. A Simple Analytical Model for the Design of Vertical Tube Absorbers. *ASHRAE Transactions*, 99(2):69–80, 1993.

[10] J. Pearson. A Simple Model for the Design of Vertical Tube Absorbers. Technical report, Ray W. Herrick Laboratories, Purdue University, 1993.

[11] M. d. Raisul, N. E. Wijeysundera, and J. C. Ho. Simplified models for coupled heat and mass transfer in falling-film absorbers. *International Journal of Heat and Mass Transfer*, 47(2004):395–406, 2002.

[12] R. A. Seban. Transport to Falling Films. *ASAE Transactions*, 6(1):417–428, 1978.

[13] B. B. Tsai and H. Perez-Blanco. Limits of Mass Transfer enhancement in lithium bromide-water absorbers by active techniques. *International Journal of Heat and Mass Transfer*, 41(15):2049–2416, 1997.

[14] S. M. Yih and K. Y. Chen. Gas Absorption Into Wavy and Turbulent Falling Films in a Wetted-Wall Column. *Chemical Engineering*, 17(1):123–136, 1982.

Chapter 5

Absorption with Presence of Mist Flow. Modelling and Numerical Implementation

ABSTRACT

This chapter describes the mathematical formulation and numerical implementation of a semi-empirical model based on Navier-Stokes equations together with energy and mass species equations simplified under the boundary layer hypotheses. The coupled equations are solved by means of finite difference method in a step by step procedure. The laminar wavy regime is considered by including and solving the Free Surface Deflection Equation. A numerical verification has been performed which includes the mathematical model described previously in chapter 4.

5.1 Introduction

The absorber usually is the largest element of absorption machines due to its low heat and mass transfer coefficients, and this fact determines the total design of the whole system. Vertical falling film flow absorbers are the typical solution of air cooled systems [25, 27, 30, 50]. In such devices the heat and mass transfer processes are produced simultaneously.
Falling film heat exchangers have a wide range of applications (evaporation, condensation, absorption, distillation, etc...) therefore it has been extensively studied by several authors [8, 10, 13, 19, 20, 22–24, 29, 37, 42, 43, 46].

One of the earliest attempts for modelling falling film $LiBr - H_2O$ absorbers was published by Grigoreva and Nakoyarkov [14]. These authors consider the case of steady state absorption in a smooth laminar falling film flow in a isothermal, impermeable vertical plate. A constant profile is assumed in streamwise velocity. The heat and mass transport are described by solving of energy and species equations in two spacial dimensions under the following assumptions: i) mass and thermal diffusion are negligible in the streamwise direction, ii) the transverse velocity is negligible. By using these simplifying assumptions the authors provide a solution by means of techniques of Fourier's separation variables. Grossman [15] uses essentially the same simplifying assumptions that Grigoreva and Nakoyarkov [14], but he uses a different boundary condition in the inlet (the inlet solution temperature is equal to the wall temperature, thus no thermal boundary layer develops from the wall) and a parabolic velocity profile. Grossman uses two methods to solve the problem. First, using the Fourier method as in Grigoreva and Nakoyarkov [14], he seeks a expansion of the series solution. Second he uses a numerical technique based on finite difference methods.
In the same line, Brauner et al. [5] presents a solution valid near the inlet region using similar technique as in Grigoreva and Nakoyarkov [14]. The Brauner's contribution is the application of Fick's law of diffusion at the interface without assuming infinite dilution in the liquid film. On the other hand, Andberg [2] is probably one of the first attempts to develop a solution for the horizontal tube case. The hydrodynamic of the falling film are divided into different regions which were solved individually in the stream-wise direction. In this case, the boundary layer approximations of the Navier Stokes equations are applied using finite difference techniques. Finally, Kawae et al. [21] develops a finite difference model for films similar to Andberg [2], but applied to vertical falling-film. The main differences are: i) thermophysical properties are not constant, ii) Fully developed parabolic stream-wise velocity profile, iii) transverse velocity equal to zero.

Unlike single-phase heat transfer, absorption process involves somewhat complex phase change phenomena at the vapor-liquid interface. This phase change at the interface provides particular boundary conditions to the heat and mass transfer. The determination of the interface condition becomes important for the design and analysis

of an absorption system in this aspect.

A mathematical model of falling film absorption of H_2O by $LiBr$ aqueous solutions has been implemented. The model is semi-empirical, based on Navier Stokes equations together with energy and mass species simplified under the boundary layer hypotheses. The coupled equations are solved by means of finite difference method in a step by step procedure. Other issue which is worth of attention is the wavy regime in vertical falling film. The experimental observation shows that wavy regime appears even in low Reynolds number ($Re \approx 20$) [33, 48]. It is also well known that wavy regime causes increase of diffusion and mass transfer [28, 31, 39, 44]. For this reason the simulation of wavy profiles are implemented together with the falling film formulation. In the mathematical model, the Free Surface Deflection equation is solved in each grid step for every Reynolds number, which is recalculated in function of mass absorbed. The mathematical model has been modified in order to consider the mist flow (see section 3.4.4).

5.2 Boundary Layer Mathematical Based Model

The absorber is modelled as a single vertical tube. The falling film flow occurs when aqueous solution flows down in the outer part of the tube. The cooling water in counter flow is used in the inner part of the tube. The vertical tube is immersed in a water vapor environment that is also introduced in the top part of the absorber. The Fig. 5.1 shows a schematic of the vertical absorber.

A similar model was original proposed by Andberg [2], however it was implemented for the simulation of absorption in horizontal tubes. This author distinguishes three different hydrodynamic regions, i) turning jet region, ii) turned jet region, iii) fully viscous film. The present work uses the same mathematical formulation as Andberg but without taking account region (i) and assuming totally fully viscous region due to that vertical tubes are simulated. The Fig. 5.2 shows details of the vertical falling film and its boundary conditions. Detailed treatment of the liquid-vapor interface boundary condition has been considered in order to take into consideration the influence of the mist flow phenomena described in chapter 3.

The following hypotheses are assumed in the calculation:

i Steady state flow.

ii The initial velocity considered corresponds to fully developed flow.

iii Physical properties variable only in the flow direction.

iv There is no shear stress at the interface.

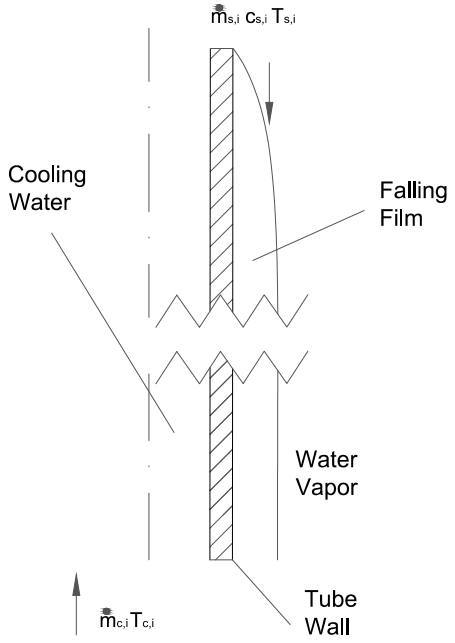

Figure 5.1: Schematic of the vertical falling film absorber

v The radius of the tube is much greater than the falling film thickness, therefore curvature effects are neglected.

vi There is thermodynamic equilibrium at the interface.

vii The flow can be both laminar smooth or wavy laminar and it is also incompressible.

viii The diffusion terms are negligible in the flow direction.

ix The convection terms are negligible in the direction orthogonal to the flow.

x The pressure gradients are negligible.

xi Dufour and Soret effects have not been considered.

xii Curvature effects due to wavy flow are neglected (capillary waves).

According to the above mentioned hypotheses, the governing conservations equations of mass (5.1), momentum (5.2), energy (5.3) and mass species (5.4) can be written as:

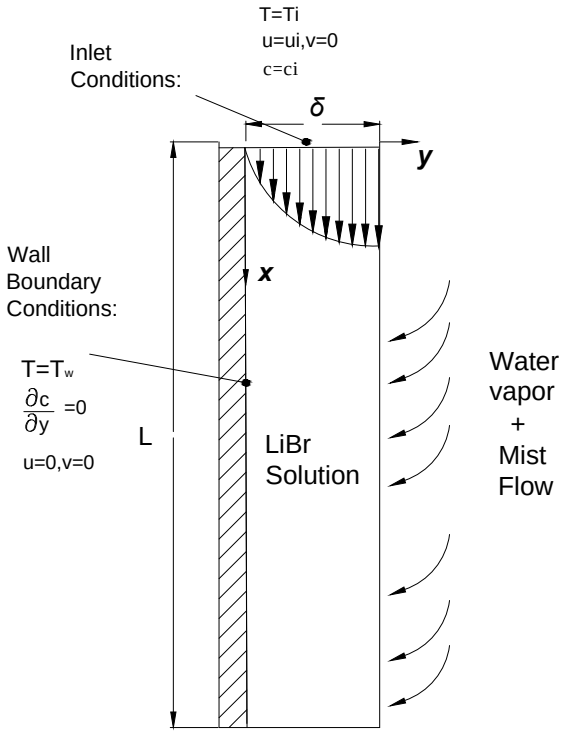

Figure 5.2: Boundary Conditions en Vertical Falling Film

$$\frac{\partial u}{\partial x} + \frac{\partial v}{\partial y} = 0 \tag{5.1}$$

$$u\frac{\partial u}{\partial x} + v\frac{\partial v}{\partial y} = gcos(\theta) + \nu\frac{\partial^2 u}{\partial y^2} \tag{5.2}$$

$$u\frac{\partial T}{\partial x} + v\frac{\partial T}{\partial y} = a\frac{\partial^2 T}{\partial y^2} \tag{5.3}$$

$$u\frac{\partial c}{\partial x} + v\frac{\partial c}{\partial y} = D\frac{\partial^2 c}{\partial y^2} \tag{5.4}$$

According with Andberg [2] and Castro [6], the above governing equations and its boundary conditions are subjected to a change of coordinates (further details are presented in appendix B). In the case of falling film flow in vertical tubes only the region (iii) is solved (fully viscous film). For this region the dimensionless coordinates are:

$$\xi = \frac{x}{L} \tag{5.5}$$

$$\zeta = \frac{y}{\delta(x)} \tag{5.6}$$

where L is the length of the vertical tube and δ is the thickness of the falling film. Under this conditions the partial derivatives are as follows:

$$\frac{\partial}{\partial x} = \frac{1}{L}\frac{y}{\delta^2}\frac{d\delta}{dx}\frac{\partial}{\partial \zeta} \tag{5.7}$$

$$\frac{\partial}{\partial y} = \frac{1}{\delta}\frac{\partial}{\partial \zeta} \tag{5.8}$$

$$\frac{\partial^2}{\partial y^2} = \frac{1}{\delta^2}\frac{\partial^2}{\partial^2 \zeta} \tag{5.9}$$

Therefore, the equation of conservation of mass in the transformed coordinates is expressed as follows:

$$\xi\frac{\partial \rho u}{\partial \xi} - \beta_1 \zeta \frac{\partial \rho u}{\partial \zeta} + \xi\frac{\partial \rho v}{\partial \zeta} = 0 \tag{5.10}$$

The remaining conservation equations momentum (5.2), energy (5.3), and species conservation(5.4) in transformed coordinates become,

$$u\xi\frac{\partial u}{\partial \varepsilon} - \beta\zeta u\frac{\partial u}{\partial \zeta} + v\xi\frac{\partial u}{\partial \zeta} = \beta_2 + \beta_3\nu\frac{\partial^2 u}{\partial \zeta^2} \tag{5.11}$$

$$\frac{\partial T}{\partial \xi} = \left(\frac{\zeta}{\delta}\frac{\partial \delta}{\partial \xi} - \frac{v}{u}\frac{L}{\delta}\right)\frac{\partial c}{\partial \zeta} + \frac{a}{\delta^2}\frac{L}{u}\frac{\partial^2 T}{\partial \zeta^2} \tag{5.12}$$

$$\frac{\partial c}{\partial \xi} = \left(\frac{\zeta}{\delta}\frac{\partial \delta}{\partial \xi} - \frac{v}{u}\frac{L}{\delta}\right)\frac{\partial c}{\partial \zeta} + \frac{D}{\delta^2}\frac{L}{u}\frac{\partial^2 c}{\partial \zeta^2} \tag{5.13}$$

where,

$$\beta_1 = \frac{x}{\delta}\frac{d\delta}{dx} = \frac{\xi}{\delta}\frac{d\delta}{d\xi}$$
$$\xi = \frac{x}{\delta} = \frac{\xi L}{\delta}$$
$$\beta_2 = xg(x) = g\xi L cos(\theta)$$
$$\beta_3 = \frac{x}{\delta^2} = \frac{\xi L}{\delta^2}$$

The boundary conditions are:

$$x = 0 \begin{cases} T_l = T_{l,in} & (a) \\ c = c_{in} & (b) \\ u = u_{l,in} & (c) \\ v = 0 & (d) \end{cases} \tag{5.14}$$

$$y = 0 \begin{cases} T = T_w & (a) \\ \nabla c \cdot \vec{n} = 0 & (b) \\ u = 0 & (c) \\ v = 0 & (d) \end{cases} \tag{5.15}$$

$$y = \delta \begin{cases} T_{l,if} = f(P_{abs}, c_{if}) & (a) \\ -\lambda \nabla T \cdot \vec{n} = h_{abs}\dot{m}_{abs,v} + h_l \dot{m}_{abs,l} & (b) \\ \frac{\partial u}{\partial x} = 0, v = 0 & (c) \end{cases} \tag{5.16}$$

The equations (5.14 a-d) represent the inlet conditions, inlet solution trremperature ($T_{l,in}$) and inlet mass concentration ($c_{l,in}$) are known data, and the inlet velocity solution ($u_{l,in}$) calculated by means of the Nusselt's typical velocity profile. The equations (5.15 a-d) represent the wall boundary conditions, where T_w is the wall temperature, and $\nabla c \cdot \vec{n} = 0$ depicts impermeable wall condition. The equations (5.16 a-c) describe the conditions of the interface, the equation (5.16 a) describes thermodynamic equilibrium, the equation (5.16 b) represents an energy balance in the liquid falling film interface. Notice that the convection heat transfer in vapor side is neglected. The equation (5.16 c) indicates no shear stress at the interface. The mass absorbed from the vapor water and the total mass of mist flow of aqueous solution can be calculated by means of the following expressions:

$$\dot{m}_{abs_{H_2O,t}} = \dot{m}_{abs,v} + \dot{m}_{abs_{H_2O,l}} \tag{5.17}$$

$$\dot{m}_{abs_{H_2O,l}} = \dot{m}_{abs,l}(1 - c_{in}) \tag{5.18}$$

$$\dot{m}_{abs_{H_2O,t}} = \frac{(1 - c_{if})\dot{m}_{abs_l} c_{in}}{c_{if}} + \frac{D\rho}{c_{if}} \nabla(1 - c) \cdot \vec{n} \tag{5.19}$$

The equation (5.17) describes the total mass flow of H_2O that enters throughout the interface, the equation (5.18) refers to portion of water liquid of the mist flow, and finally the equation (5.19) describes by means of the Fick's law for a moving flow of the total mass flow of H_2O. In appendix C there are further details about how equation is obtained. The above equations together with equation (3.12) (Void fraction is an experimental data, see chapter 3) are solved in order determine the four unknowns ($\dot{m}_{abs_{H_2O,t}}, \dot{m}_{abs_v}, \dot{m}_{abs_{H_2O,l}}, \dot{m}_{abs_l}$).

The above set of expressions are a partial differential system of equations, and due to its parabolic nature, they can be solved using a step-by-step procedure. The following section provides details about the algorithm of resolution.

5.2.1 Wavy Regime Model

One of the characteristics of the hydrodynamics in vertical falling film is the wave phenomena in the free-surface flow. It is well known that wavy motion in falling liquid films enhances significantly the heat and mass transfer, therefore it has been investigated both experimentally and analytically for many authors [4, 16–18, 26, 28, 31, 33–36, 39–41, 44, 45, 47–49]. The problem is not an easy issue from numerical point of

view, due to heat and mass transfer coupled problem and the presence and the unsteady behavior of the wave motion. From a hydrodynamic point of view, the wave motion is function of Reynolds number of the different flow regimes, the table 5.1 shows a brief description of falling film flow.

Flow Description	Reynolds Number
smooth film	$\mathrm{Re} \leq 20$
capillary wavy laminar	$20 < \mathrm{Re} < 200$
inertial wavy laminar (Roll waves)	$200 < \mathrm{Re} < 1000$
inertial wavy turbulent	$1000 < \mathrm{Re} < 4000$
fully turbulent	$\mathrm{Re} \geq 4000$

Table 5.1: Falling film flow description at different Reynolds numbers [16, 33, 34]

This work focuses in capillar wavy laminar regime ($20 < Re < 200$). In literature some of the most relevant studies about wavy phenomena in free surface are those that assume a periodic wave state. This assumption simplifies the mathematical derivation and it also provides good confidence in numerical results. Yang [48] and Hirshburg [16] obtain the Free Surface Deflection Equation, they assume a parabolic profile of the streamwise velocity. Then, the cross-stream velocity is calculated from the conservation of mass. The velocity distributions are substituted into momentum equation and integrated across the film. In the Fig. 5.3 are shown the characteristic dimensions of the problem. The wavelength of the wavy surface is Λ, the mean film thickness of the film over the wavelength is δ_o, the characteristic velocity is defined as $U_o = \frac{\Gamma}{\rho_l \delta_0}$ and the wave number is $\psi = \frac{\delta_o}{\Lambda}$. Since the film thickness is too small compared to flow length, $\Lambda \gg \delta_o$ or $\psi \ll 1$, this simplifies the formulation. Hirshburg [16] tried to extend the Free Surface Deflection Equation to higher Reynolds numbers where $\Lambda \sim \psi$, however his mathematical formulation involves an uncertainty and it becomes unpractical. Patnaik [33], Patnaik and Pérez-Blanco [34, 35] also present a mathematical model for roll waves in falling films for range value of $200 < Re < 1000$, the authors distinguish four different wave zones, each zone is characterized by a film thickness function, that are obtained by Brackbill et al. [4]. Then, a parabolic profile for the streamwise velocity is assumed, this profile is function of the x and y coordinates, t, and the corresponding film thickness function, in this way, a different parabolic profile is obtained for each wave zone. The transverse velocity component is obtained by deriving the continuity equation. A periodic smooth function which passes through the known points is obtained with a three-term Fourier series.

As mentioned previously, this work is based on the assumption of a periodic wave state, [16–18, 45, 47, 48]. Under this conjecture the Free Surface Deflection Equation

is obtained:

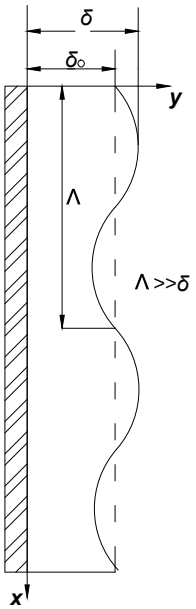

Figure 5.3: Characteristic dimensions in Wavy Regime

$$\frac{\psi^3}{We}(1+\phi)^3\frac{\partial^3\phi}{\partial\eta^3} - \left[\frac{Z^2\psi}{5}(1+\phi)^2 - 1.2\psi(1-Z)^2\right]\frac{\partial\phi}{\partial\eta} + Fr(3\phi+3\phi^3+\phi^3) - \frac{12}{Re} + \left[Fr - \frac{12}{Re}\right] = 0 \tag{5.20}$$

where

The equation (5.20) is a nonlinear partial differential equation, its solution yields in a nondimensional wave profile. Since ψ and Z are variables that are characterized by fluid hydrodynamics and surface tension, then $Z = f(Re,\gamma)$ and $\psi = f(Re,\gamma)$, where γ is a nondimensional parameter for the surface tension and it is defined as $\gamma = \frac{\sigma(\nu^4 g)^{-\frac{1}{3}}}{\rho_l}$. Anshus [3], Pierson and Whitaker [36] have studied and solved the linear

Re	=	$\frac{4\Gamma}{\mu}$
We	=	$\frac{\rho U_o^2 \delta_o}{\sigma}$
Fr	=	$\frac{g\delta_o}{U_o^2}$
η	=	$\frac{x-zt}{\Lambda}$
Z	=	$\frac{z}{U_o}$
ψ	=	$\frac{\delta_o}{\Lambda}$

Table 5.2: Dimensionless parameters for the Free Surface Deflection Equation

stability problem associated a vertical liquid film under the action of gravity in terms of the Orr-Sommerfeld Equation (OSE). OSE describes the linear two-dimensional modes of disturbance to a viscous parallel flow and it determines with accuracy what are the conditions for hydrodynamic stability are. In the case of the free surface flows, the resolution of the OSE provides the characteristic physical parameters of the wave flow (ψ and Z). Then such parameters are applied in the equation (5.20). Thus ψ and Z are maintained constant for each solution. The equation (5.20) can be solved via a numerical spectral method [11], therefore it can be expressed by means on analysis in Fourier series:

$$\phi(\eta_i) = \sum_{n=1}^{N} A_n sin(2n\pi\eta_i) + B_n cos(2n\pi\eta_i) \tag{5.21}$$

The equation (5.21) satisfies the periodical conditions of the equation (5.20) and both are a mathematical closed problem. The solution is achieved using a LU decomposition to obtain A_n and B_n constants, thus ϕ and its derivatives can be obtained directly. The Gauss-Seidel method is employed to handle nonlinearity.

Orr-Sommerfeld and Free Surface Deflection equations may be consider equivalent, however it is much easier to handle numerically with the latter. Free Surface Deflection Equation uses spectral methods for its resolution, while OSE is an eigenvalue problem an it requires a tremendous amount of calculation.

All authors previously mentioned that solve vertical falling films under laminar wavy flow [16–18, 33–35, 45, 47, 48] assume functions in order to describe velocity fields. This fact yields into a pure heat and mass transfer problem. The mass species and energy equations and the appropriate boundary conditions are solved in parabolic way in order to perform the simulation of absorption under wavy falling film. At difference of the referred authors, this work obtains the velocity field by solving the equations (5.13) and (5.11) simultaneously. Another important difference is also the

solution of the equation (5.20): while Yang and Hirshburg assume the same wave profile for the entire domain, this work solves the equation (5.20) for each grid point in the falling film domain. Taking into account that mass absorbed along the process increases mass flow, is reasonable to assume that Re is changing as the aqueous solution is flowing down.

5.2.2 Coolant fluid domain

The coolant water in counter flow is solved numerically using the equations of conservation of mass, momentum and energy in its integral form.

$$\int_{SC} \rho(\vec{v}\cdot\vec{n})dS + \frac{\partial}{\partial t}\int_{VC}\rho dV = 0 \tag{5.22}$$

$$\int_{SC} \vec{v}\rho\,(\vec{v}\cdot\vec{n})\,dS + \frac{\partial}{\partial t}\int_{VC}\vec{v}\,\rho dV = \vec{F}_{sup} + \vec{F}_{mas} \tag{5.23}$$

$$\int_{SC} e\rho\,(\vec{v}\cdot\vec{n})\,dS + \frac{\partial}{\partial t}\int_{VC} e\rho dV = \dot{Q} - \dot{W} \tag{5.24}$$

where e is defined as:

$$e = \mathbf{u} + \frac{u^2}{2} + g\cdot y = h - \frac{P}{\rho} + \frac{u^2}{2} + g\cdot y \tag{5.25}$$

The coolant fluid domain is divided in concatenated control volumes where the governing equations are discretized as follows:

- Continuity Equation:

$$\dot{m}_{c,i} = \dot{m}_{c,i-1} - \frac{\bar{\rho}_c - \bar{\rho}_c^o}{\Delta t} S\Delta x \tag{5.26}$$

- Momentum Equation:

$$P_{c,i} = P_{c,i-1} - \left(\frac{\dot{m}_{c,i}}{S\rho_{c,i}}\right)^2 + \left(\frac{\dot{m}_{c,i-1}}{S\rho_{c,i-1}}\right)^2 - \left(\frac{\bar{\dot{m}}_c - \bar{\dot{m}}_c^o}{S\Delta t} + \frac{\bar{\tau}p}{S} + \bar{\rho}_c g sin(\theta)\right)\Delta x \tag{5.27}$$

- Energy Equation:

$$h_{c,i} = \frac{2\dot{Q} - \dot{m}_{c,i}a + \dot{m}_{c,i-1}b + \frac{S\Delta x}{\Delta t}c}{\frac{\bar{\rho}^o S\Delta z}{\Delta t} + \dot{m}_{c,i} + \dot{m}_{c,i-1}} \tag{5.28}$$

Where:

$$a = \frac{1}{2}\left(\frac{\dot{m}_{c,i}^2}{\rho_{c,i}^2 S^2} - \frac{\dot{m}_{c,i-1}^2}{\rho_{c,i-1}^2 S^2}\right) + (g sin(\theta)\Delta x - h_{c,i-1}) \tag{5.29}$$

$$b = \frac{1}{2}\left(\frac{\dot{m}_{c,i-1}^2}{\rho_{c,i-1}^2 S^2} - \frac{\dot{m}_{c,i}^2}{\rho_{c,i}^2 S^2}\right) + (-g sin(\theta)\Delta x + h_{c,i-1}) \tag{5.30}$$

$$c = \bar{\rho}_{c,i}^o(h_{c,i}^o + h_{c,i-1}^o - h_{c,i-1}) + [(P_{c,i-1} + P_{c,i}) - (P_{c,i-1}^o + P_{c,i}^o)] - \frac{\bar{\rho}_c^o}{2}\left(\frac{\dot{m}_{c,i-1}^2}{\rho_{c,i-1}^2 S^2} + \frac{\dot{m}_{c,i}^2}{\rho_{c,i}^2 S^2}\right) + \frac{\bar{\rho}_c^o}{2}\left(\frac{\dot{m}_{c,i-1}^{o2}}{\rho_{c,i-1}^{o2} S^2} + \frac{\dot{m}_{c,i}^{o2}}{\rho_{c,i}^{o2} S^2}\right) \tag{5.31}$$

The above equations are presented in transient formulation, but the resolution is performed in steady state. In the same way the terms of kinetic energy, (5.29) and (5.30) have a minimum contribution due to the density in the coolant fluid barely

has variation and therefore such terms are neglected. The resolution is achieved by solving consecutively the control volumes from the inlet of the tube to the outlet. The information obtained at each control volume is transferred to its neighbor following the flow direction (step-by-step resolution algorithm). At each control volume, the fluid formulation requires the use of empirical information in order to evaluate the following parameters:

- The averaged shear stress in each control volume ($\bar{\tau}_i$), which is related to the friction factor (f_i) ([7]):

$$\bar{\tau}_i = \frac{f_i}{4} \frac{\bar{\dot{m}}^2}{2\bar{\rho}_{c,i} S^2} \tag{5.32}$$

- The local heat transfer coefficient (α_i), which is used to evaluate the heat transfer between the tube and the fluid [12]:

$$\dot{q}_{c,i} = \alpha_i (T_{w,i} - \bar{T}_c) \tag{5.33}$$

Finally, the axial temperature field of the tube wall is obtained by integrating and discretizing energy equation which is solved using a TDMA solver [32]. Further information about coolant algorithm resolution can be consulted in [1, 9]

5.2.3 Resolution Procedure

Three different domains can be distinguished, see Fig.5.4: i) $LiBr - H_2O$ liquid falling film solution, ii) coolant fluid domain, and iii) wall tube (solid). Every domain is discretized and is solved independently, in the case of fluid domain the resolution is in flow direction (step-by-step resolution algorithm). In both fluid domains (i) and (ii) the interchange of information goes through the solid domain (iii). The complete resolution is achieved when temperature field in wall tube do not undergoes changes in its value between consecutive iterations. The complete algorithm resolution is as follows:

- Falling film domain see Fig. 5.5:
  1. Coupled resolution of momentum (5.11) and mass conservation (5.10) equations, for obtaining the values of the components of the velocity. Calculation of the boundary layer thickness considering a smooth film thickness.
  2. The Free Surface Deflection Equation (5.20) is solved in order to obtain wave profile which is function Re and the dimensionless surface tension parameter γ. The new boundary layer thickness as function of wave profile is calculated and introduced.

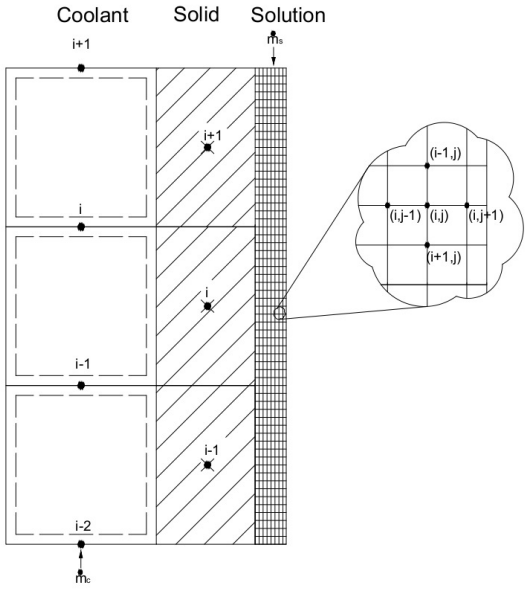

Figure 5.4: Discretization of $LiBr$ solution, solid and coolant domains (from right to left)

3. Coupled resolution of energy (5.12) and mass species conservation (5.13) equations.
4. Calculation of the mass absorbed by solving the equations: (5.17), (5.18) and (5.19)
5. Check if energy balance at interface is accomplished, $-\lambda\nabla T\cdot\vec{n} = h_{abs}\dot{m}_{abs_v} + h_l\dot{m}_{abs_l}$. If so, continue with the calculation, if not back to point 3.
6. Check if mass balance is accomplished $|\frac{\dot{m}_{abs}-\dot{m}_{abs_o}}{\dot{m}_{abs}}| \leq \varepsilon$. If so, go to the next row, if not, back to the point 1.

- Coolant fluid domain:

1. Calculation of fluid properties $(\rho, \mu, h \ldots)$ in function of T_c and P_c.
2. Resolution of mass conservation equation.
3. Resolution of momentum conservation equation in order to obtain P_i, factor friction is obtained using empirical correlations [38].

4. Resolution of energy conservation equation in order to obtain T_i, the heat transfer coefficients is obtained using empirical correlations [12].
5. Check if mass and energy balances are accomplished. If so, go to the next control volume, if not, back to the point 2.

- Wall tube:

1. Solve energy conservation equation in order to obtain field temperature along the wall tube Tw.
2. Evaluate $|\frac{T_w - T_w^o}{T_w}| \leq \varepsilon$, if the previous condition is not fulfilled back to calculate falling film domain.

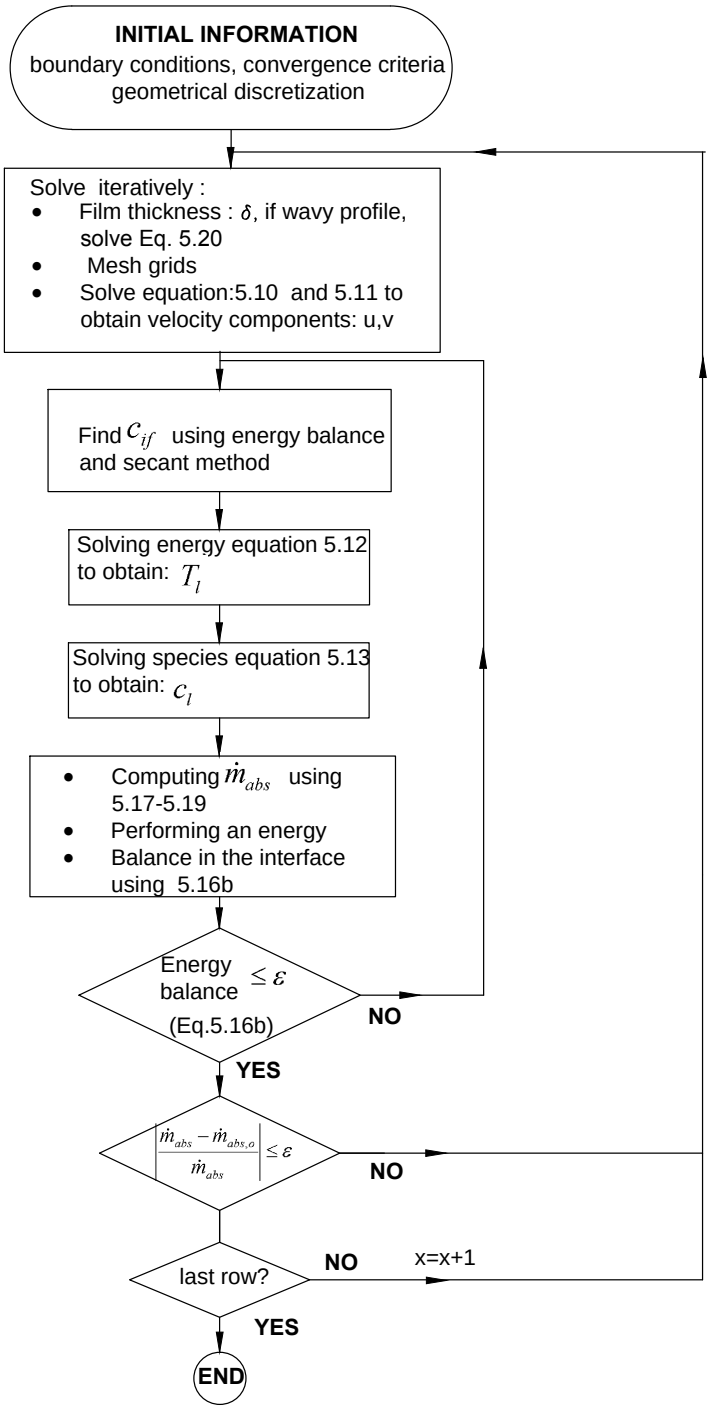

Figure 5.5: Resolution algorithm for boundary layer model falling film domain absorption.

5.3 Numerical verification

Likewise as described in section 4.3 in previous chapter, a numerical verification study is performed. Programing errors are evaluated by comparing the mathematical model described along this chapter against the 1-D model described in chapter 4. The characteristics of the benchmark case considered are the same as shown in table 4.1.

5.3.1 Programing Errors

For this test and absorption in non-isothermal wall which includes the solution of the coolant fluid is considered as baseline case. In the first instance, the Fig. 5.6 depicts the temperature profiles in dimensionless form for the boundary layer based model. The interface and bulk average temperatures in the film side, as well as wall solid and coolant fluid side temperatures along the absorber are plotted. The inlet coolant temperature has been used for obtaining the dimensionless quantities. The Fig. 5.7 depicts mass concentration profiles (bulk and interface). The dimensionless form is obtained using the inlet mass concentration. In addition, results for the 1D-dimensional model are shown in the Fig. 5.8 and the Fig. 5.9.

In order to close the numerical error's study, a last test has been performed using the same working conditions but varying the Re number. The table 5.3 resumes the results for both models at different Re numbers. The study show an acceptable agreement when $Re \approx 60$, however at higher Re numbers the boundary layer based model shows a decrease in mass and heat transfer rates, while the 1-D empirical model always shows a positive trend when Re increases. In Chapter 7 (Numerical Validation) it is demonstrated that there is an optimal Re number where mass and transfer rates are the optimal. Further increases of Re not necessarily increases the absorber's performance. The boundary layer based model seems to predict this fact, but it is not the same situation for 1D-empirical model.

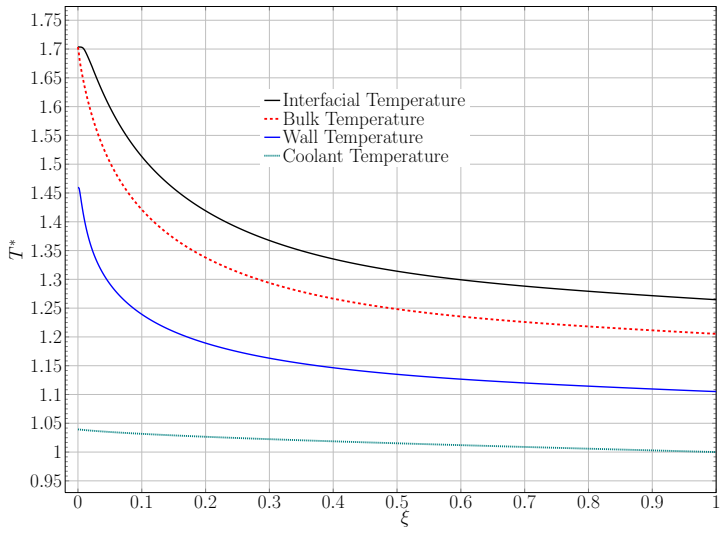

Figure 5.6: Dimensionless Temperature Profiles (Interfacial, Average Bulk, Wall and Coolant) along Vertical Tube Absorber. Boundary layer based model.

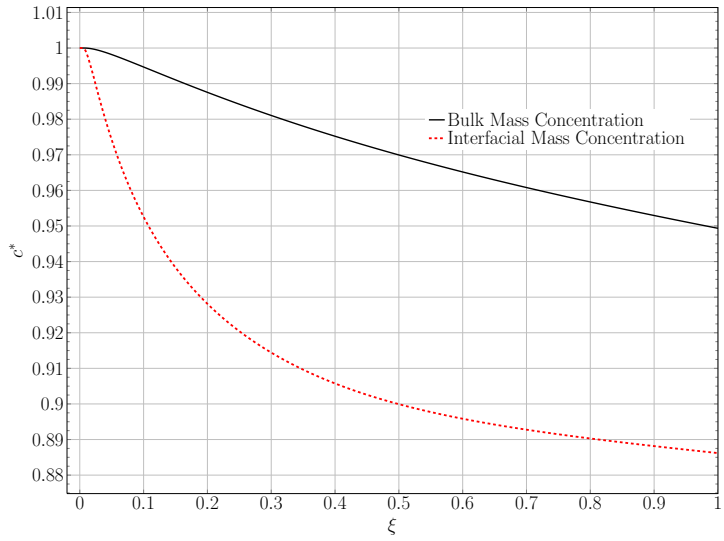

Figure 5.7: Dimensionless Mass Concentration Profiles (Interfacial and Average Bulk) along Vertical Tube Absorber. Boundary layer based model.

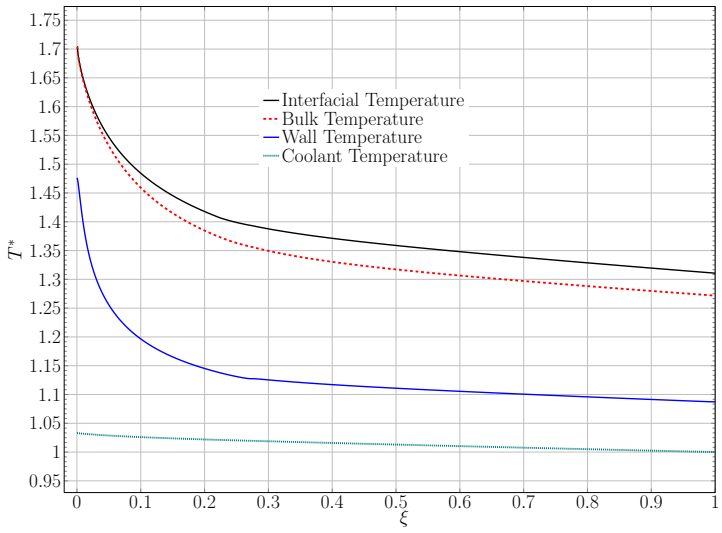

Figure 5.8: Dimensionless Temperature Profiles (Interfacial, Average Bulk, Wall and Coolant) along Vertical Tube Absorber. 1-D empirical model

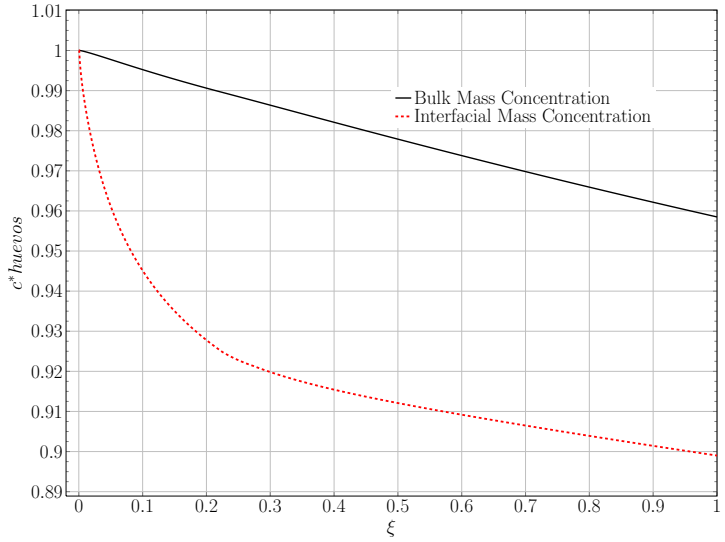

Figure 5.9: Dimensionless Mass Concentration Profiles (Interfacial and Average Bulk) along Vertical Tube Absorber. 1-D empirical model

$\dot{Q}_{abs,v}$ (W)		$\dot{Q}_{abs,c}$ (W)		$\dot{m}_{abs}$ $(kg \cdot s^{-1})$		c_{out} $(\%LiBr)$		T_{out} $(^{\circ}C)$	
BL	1D	BL	1D	BL	1D	BL	1D	BL	1D
$Re = 60$									
4.8703e+02	5.023412e+02	5.9649e+02	4.977e+02	1.8897e-04	1.948E-04	5.696e+01	5.750e+01	3.615e+01	3.815e+01
$Re = 100$									
4.5525e+02	5.4951e+02	6.4553e+02	5.9136e+02	1.7706e-04	2.129301E-04	5.808e+01	5.8343e+01	3.677192e+01	3.932e+01
$Re = 150$									
4.2383e+02	5.732e+02	6.9471e+02	6.6976e+02	1.6520e-04	2.221e-04	5.873e+01	5.881328e+01	3.768002e+01	4.0215e+01

Table 5.3: Comparison of Results Between Boundary Layer Based Model (BL) against 1D-Empirical (1D) Model at different Re Numbers

5.3.2 Convergence Errors

For the convergence error study let us refer to resolution algorithm (see Fig. 5.5) The convergence criteria to be evaluated are the following:

1. The relative error in the change of velocity between two consecutive iterations when momentum conservation and continuity equations are solved (ε_1).
2. The relative error in the change of the film thickness between two consecutive iterations (ε_2).
3. The heat imbalance at the interface (the coupling between energy and LiBr conservation equations) which is calculated using secant method (ε_3).
4. The relative error in the mass absorbed between two consecutive iterations at the interface (ε_4).

For this study is considered absorption in an isothermal wall, ($T_w = 33°$ C). The table 5.4 shows the results for the convergence criteria ε_1 and ε_2. The data computed are: heat load calculated in the film side ($\dot{Q}_{abs,c}$), energy input through the interface ($\dot{Q}_{abs,v}$), mass absorbed $\dot{m}$, outlet mass concentration c_{out}, outlet solution concentration T_{out}. The asymptotic results are achieved when $\varepsilon_1 = \varepsilon_2 \approx 1e^{-7}$.

The table 5.5 shows the results for the convergence criteria ε_3 and ε_4. The computed data as the same as describes in the table 5.4. The asymptotic results are achieved when $\varepsilon_3 = \varepsilon_4 \approx 1.0e^{-3}$. The mesh used in this test was $N_x = 800$ and $N_y = 250$.

5.3.3 Truncation Errors (Discretization)

The table 5.6 shows the results for the test of discretization errors. N_x and N_y represent the grid nodes along the x and y coordinates respectively. Δx and Δy are the steps calculations in the x and y directions. The rest of the data computed are the same as the table 5.4. The asymptotic result is almost reached when $N_x = 800$ and $N_y = 250$.

ε_1	ε_2	$\dot{Q}_{abs,c}$ (W)	$\dot{Q}_{abs,v}$ (W)	$\dot{m}_{abs}$ $(kg \cdot s^{-1})$	c_{out} $(\%LiBr)$	T_{out} $(^\circ C)$
1e-2	1e-2	7.806965e+02	6.098250e+02	2.372478e-04	5.816022e+01	3.752560e+01
1e-3	1e-2	7.807330e+02	6.098688e+02	2.372644e-04	5.816009e+01	3.752593e+01
1e-4	1e-2	7.807330e+02	6.098688e+02	2.372644e-04	5.816009e+01	3.752593e+01
1e-5	1e-2	7.808634e+02	6.100134e+02	2.373199e-04	5.815967e+01	3.752638e+01
1e-6	1e-2	7.810300e+02	6.101979e+02	2.373911e-04	5.815914e+01	3.752693e+01
1e-7	1e-2	7.809844e+02	6.101488e+02	2.373721e-04	5.815928e+01	3.752687e+01
1e-3	1e-3	7.404730e+02	5.570051e+02	2.164556e-04	5.831693e+01	3.688859e+01
1e-4	1e-3	7.406318e+02	5.572610e+02	2.165548e-04	5.831618e+01	3.689404e+01
1e-5	1e-3	7.406318e+02	5.572610e+02	2.165548e-04	5.831618e+01	3.689404e+01
1e-6	1e-3	7.406318e+02	5.572610e+02	2.165548e-04	5.831618e+01	3.689404e+01
1e-7	1e-3	7.406318e+02	5.572610e+02	2.165548e-04	5.831618e+01	3.689404e+01
1e-4	1e-4	7.434944e+02	5.614941e+02	2.182181e-04	5.830361e+01	3.696860e+01
1e-5	1e-4	7.525337e+02	5.746012e+02	2.233633e-04	5.826477e+01	3.718780e+01
1e-6	1e-4	7.055785e+02	5.112927e+02	1.985183e-04	5.845281e+01	3.633682e+01
1e-7	1e-4	7.056194e+02	5.113413e+02	1.985371e-04	5.845266e+01	3.633716e+01
1e-5	1e-5	7.078040e+02	5.141608e+02	1.996415e-04	5.844428e+01	3.636927e+01
1e-6	1e-5	7.060398e+02	5.118514e+02	1.987362e-04	5.845115e+01	3.634135e+01
1e-7	1e-5	7.056194e+02	5.113413e+02	1.985371e-04	5.845266e+01	3.633716e+01
1e-6	1e-6	7.057126e+02	5.114364e+02	1.985738e-04	5.845238e+01	3.633698e+01
1e-7	1e-6	7.060398e+02	5.118514e+02	1.987362e-04	5.845115e+01	3.634135e+01
1e-7	1e-7	7.057802e+02	5.115231e+02	1.986078e-04	5.845213e+01	3.633794e+01
1e-8	1e-8	7.058508e+02	5.116054e+02	1.986398e-04	5.845188e+01	3.633844e+01
1e-9	1e-9	7.058508e+02	5.116054e+02	1.986398e-04	5.845188e+01	3.633844e+01

Table 5.4: Convergence study depending on ε_1 (relative error in the change of velocity) and ε_2 (relative error in the change of the film thickness) for the boundary layer based model

ε_3	ε_4	$\dot{Q}_{abs,c}$ (W)	$\dot{Q}_{abs,v}$ (W)	$\dot{m}_{abs}$ $(kg \cdot s^{-1})$	c_{out} $(\%LiBr)$	T_{out} $(^\circ C)$
$1.0e^{-1}$	$1.0e^{-1}$	7.058532e+02	5.116078e+02	1.986393e-04	5.845189e+01	3.633845e+01
$1.0e^{-2}$	$1.0e^{-1}$	7.058510e+02	5.116056e+02	1.986397e-04	5.845188e+01	3.633844e+01
$1.0e^{-3}$	$1.0e^{-1}$	7.058508e+02	5.116054e+02	1.986398e-04	5.845188e+01	5.845188e+01
$1.0e^{-4}$	$1.0e^{-1}$	7.058508e+02	5.116054e+02	1.986398e-04	5.845188e+01	3.633844e+01
$1.0e^{-2}$	$1.0e^{-2}$	7.058510e+02	5.116056e+02	1.986397e-04	5.845188e+01	3.633844e+01
$1.0e^{-3}$	$1.0e^{-2}$	7.058508e+02	5.116054e+02	1.986398e-04	5.845188e+01	3.633844e+01
$1.0e^{-4}$	$1.0e^{-2}$	7.058508e+02	5.116054e+02	1.986398e-04	5.845188e+01	3.633844e+01
$1.0e^{-3}$	$1.0e^{-3}$	7.058508e+02	5.116054e+02	1.986398e-04	5.845188e+01	3.633844e+01
$1.0e^{-4}$	$1.0e^{-4}$	7.058508e+02	5.116054e+02	1.986398e-04	5.845188e+01	3.633844e+01

Table 5.5: Convergence study depending on ε_3 (heat imbalance at interface) and ε_4 (relative error in mass absorbed) for the boundary layer based model

N_x	N_y	Δx (m)	Δy (m)	$\dot{Q}_{abs,c}$ (W)	$\dot{Q}_{abs,v}$ (W)	$\dot{m}_{abs}$ $(kg \cdot s^{-1})$	c_{out} $(\%LiBr)$	T_{out} $(^{\circ}C)$
100	40	0.01	$9.3805e^{-6}$	7.215611e+02	5.280265e+02	2.051450e-04	5.840253e+01	3.633157e+01
200	40	$5e^{3}$	$9.3805e^{-6}$	7.222257e+02	5.287536e+02	2.053724e-04	5.840081e+01	3.633376e+01
400	40	$2.5e^{-3}$	$9.3805e^{-6}$	7.224186e+02	5.289769e+02	2.054804e-04	5.839999e+01	3.633485e+01
800	40	$1.25e^{-3}$	$9.3805e^{-6}$	7.225355e+02	5.291083e+02	2.055275e-04	5.839964e+01	3.633540e+01
1600	40	$6.25e^{-3}$	$9.3805e^{-6}$	7.226066e+02	5.291861e+02	2.055482e-04	5.839948e+01	3.633567e+01
3200	40	$3.125e^{-3}$	$9.3805e^{-6}$	7.226621e+02	5.292538e+02	2.055738e-04	5.839929e+01	3.633625e+01
100	80	0.01	$9.3805e^{-6}$	7.117411e+02	5.177068e+02	2.010529e-04	5.843357e+01	3.633249e+01
200	80	$5e^{3}$	$4.69025e-6$	7.122909e+02	5.183157e+02	2.012964e-04	5.843172e+01	3.633434e+01
400	80	$2.5e^{-3}$	$4.69025e-6$	7.125411e+02	5.185940e+02	2.013975e-04	5.843095e+01	3.633533e+01
800	80	$1.25e^{-3}$	$4.69025e-6$	7.126615e+02	5.187282e+02	2.014461e-04	5.843058e+01	3.633584e+01
1600	80	$6.25e^{-3}$	$4.69025e-6$	7.127307e+02	5.188034e+02	2.014671e-04	5.843043e+01	3.633605e+01
3200	80	$3.125e^{-3}$	$4.69025e-6$	7.127582e+02	5.188336e+02	2.014780e-04	5.843034e+01	3.633613e+01
6400	80	$1.562e{-}4$	$4.69025e-6$	7.128238e+02	5.189163e+02	2.015100e-04	5.843010e+01	3.633698e+01
100	160	0.01	$2.345125e-6$	7.067640e+02	5.125014e+02	1.989897e-04	5.844923e+01	3.633449e+01
200	160	$5e^{3}$	$2.345125e-6$	7.073071e+02	5.131014e+02	1.992317e-04	5.844739e+01	3.633621e+01
400	160	$2.5e^{-3}$	$2.345125e-6$	7.075569e+02	5.133783e+02	1.993333e-04	5.844662e+01	3.633713e+01
800	160	$1.25e^{-3}$	$2.345125e-6$	7.076561e+02	5.134910e+02	1.993857e-04	5.844622e+01	3.633758e+01
1600	160	$6.25e^{-3}$	$2.345125e-6$	7.077263e+02	5.135674e+02	1.994080e-04	5.844605e+01	3.633780e+01
3200	160	$3.125e^{-3}$	$2.345125e-6$	7.077471e+02	5.135903e+02	1.994191e-04	5.844597e+01	3.633784e+01
6400	160	$1.562e^{-4}$	$2.345125e-6$	7.077762e+02	5.136205e+02	1.994281e-04	5.844590e+01	3.633784e+01
200	250	$5e^{3}$	$1.50088e-6$	7.055009e+02	5.112153e+02	1.984853e-04	5.845306e+01	3.633710e+01
400	250	$2.5e^{-3}$	$1.50088e-6$	7.057090e+02	5.114505e+02	1.985935e-04	5.845224e+01	3.633797e+01
800	250	$1.25e^{-3}$	$1.50088e-6$	7.058508e+02	5.116054e+02	1.986398e-04	5.845188e+01	3.633844e+01
1600	250	$6.25e^{-3}$	$1.50088e-6$	7.059116e+02	5.116728e+02	1.986645e-04	5.845170e+01	3.633866e+01
3200	250	$3.125e^{-3}$	$1.50088e-6$	7.059325e+02	5.116957e+02	1.986754e-04	5.845161e+01	3.633870e+01
6400	250	$1.562e^{-4}$	$1.50088e-6$	7.059462e+02	5.117097e+02	1.986791e-04	5.845159e+01	3.633870e+01
12800	250	$7.812e^{-5}$	$1.50088e-6$	7.059560e+02	5.117209e+02	1.986833e-04	5.845155e+01	3.633876e+01

Table 5.6: Convergence study depending on N_x (grid along x coordinate)and N_y (grid along y coordinate) for the boundary layer based model

5.4 Conclusions

Along this chapter have been exposed the mathematical formulation and the numerical implementation of a semi-empirical model based on Navier Stokes equations together with energy and mass species simplified under the boundary layer hypotheses. The coupled equations are solved by means of finite difference method in a step by step procedure. In order to consider the wave regime, the Free Surface Deflection Equation is solved in each grid step for every Reynolds number, which is recalculated in function of mass absorbed. Special treatment in the liquid vapor interface has been implemented in order to consider the presence of mist flow. A numerical verification study has been performed. The 1-D mathematical model described in the chapter 4 has been used to evaluate programing errors. It has been observed some discrepancies between both models when $Re \approx 80$. For this reason such model is discarded in the experimental validation presented in chapter 7.

Nomenclature

A_n, B_n	coefficients in Fourier series
A	area, m^2
a	thermal diffusivity, $m^2\ s^{-1}$
c_p	specific heat capacity, $J\ kg^{-1}\ K^{-1}$
c	$LiBr$ mass fraction concentration
D	mass diffusivity, $m^2\ s^{-1}$
d	tube diameter, m
F_{sup}	superficial forces, $kg\ m\ s^{-2}$
F_{mas}	mass forces, $kg\ m\ s^{-2}$
f	friction factor
g	acceleration due to gravity, $m\ s^{-2}$
h	specific enthalpy, $J\ kg^{-1}$
L	tube length, m
M	heat capacity, $W\ K^{-1}$
$\dot{m}$	mass flow , $kg\ s^{-1}$
$\vec{n}$	unitary normal vector
p	perimeter, m
P	pressure, Pa
$\dot{Q}$	heat rate, W
$\dot{q}$	heat flux, $W\ m^{-2}$
r	tube radius, m
S	surface, cross section, m^2
T	temperature, K
t	time, s

U_o	mean characteristic velocity, $m\ s^{-1}$
V	volume, m^3
$\mathbf{u}$	internal energy, $J\ kg^{-1}$
u	velocity profile x axis direction, $m\ s^{-1}$
v	velocity profile y axis direction, $m\ s^{-1}$
$\dot{W}$	work, W
x	coordinate, m
y	coordinate, m
z	wave velocity, $m\ s^{-1}$
Z	dimensionless Wave velocity

Greek symbols

α	heat transfer coefficient, $W\ m^{-2}\ K^{-1}$
δ	film thickness, m
δ_o	mean film thickness, m
γ	nondimensional parameter for the surface tension
η	dimensionless x coordinate in wave profile
ε	convergence accuracy criterion
ξ	dimensionless, x coordinate
ζ	dimensionless, y coordinate
θ	inclination angle, rad
μ	dynamic viscosity, $kg\ m^{-1}\ s^{-1}$
ν	kinematic viscosity, $m^2\ s^{-1}$
Λ	wave length, m
λ	thermal conductivity, $W\ m^{-1}\ K^{-1}$
ρ	density, $kg\ m^{-3}$
τ	shear stress, Pa
ϕ	dimensionless y coordinate in wave profile
σ	surface tension, $N\ m^{-1}$
ψ	wave number

Dimensionless Groups

Fr	Froude Number, $Fr = \frac{g\delta_o}{V_o^2}$
Re	Reynolds Number, $Re = \frac{4\Gamma}{\mu}$
We	Weber Number, $We = \frac{\rho V_o^2 \delta_o}{\sigma}$

Subscripts

abs	absorption
c	coolant fluid
H_2O	related to water element
if	interface conditions
in	inlet conditions, inner
i	grid position in x direction
l	liquid phase in LiBr solution
out	outlet conditions, outer
t	total
v	vapor phase
w	wall solid tube

Superscripts

$\bar{}$	arithmetic average
o	previous step value

Bibliography

[1] N. Ablanque. *Numerical Simulation and Experimental Validation of Vapor Compression Refrigerating Systems. Special Emphasis on Natural Refrigerants.* PhD thesis, Universitat Politècnica de Catalunya, 2010.

[2] J. W. Andberg. *Absorption of Vapours into Liquid Films Flowing over Cooled Horizontal Tubes.* PhD thesis, University of Texas, 1986.

[3] B. E. Anshus. On the Asymptotic Solution to the Falling Film Stability Problem. *Industrial and Engineering Chemical Fundamentals*, 11(4):502–508, 1972.

[4] J. U. Brackbill, D. B. Kothe, and C. Zemach. Modelling of Wavy Flow in turbulent free falling films. *International Journal of Multiphase Flow*, 15(1): 505–520, 1989.

[5] N. Brauner, D. Moalem, and H. Meyerson. Coupled Heat condensation and mass absorption withcomparable concentrations of absorbate and absorbent. *International Journal of Heat and Mass Transfer*, 32(10):1897–1906, 1989.

[6] J. Castro. *Simulation of Heat and Mass Transfer Phenomena in the Critical Elements of H_2O-LiBr Absorption Cooling Machines. Experimental Validation and Application to Design.* PhD thesis, Universitat Politècnica de Catalunya, 2005.

[7] S. W. Churchill. Friction-factor equation spans all fluid-flow regimes. *Chemical Engineering*, 84(24):91–92, 1977.

[8] M. C. Chyu and A. E. Bergles. An Analytical and Experimental Study of Falling-Film Evaporation on a Horizontal Tube. *Journal of Heat Transfer - Transactions of ASME*, 109(4):983–990, 1987.

[9] O. García-Valladares. *Simulación numérica y validación experimental de evaporadores, condensadores y tubos capilares. integración en sistemas de refrigeración por compresión.* PhD thesis, Universitat Politècnica de Catalunya, 2000.

[10] M. S. Genk and H. H. Saber. An Investigation of the Breakup of an Evaporating Liquid Film, Falling Down a Vertical, Uniformly Heated Wall. *Journal of Heat Transfer - Transactions of ASME*, 124(1):39–49, 2002.

[11] C. F. Gerald. *Applied Numerical Analysis.* Addison-Wesley, 1978.

[12] V. Gnielinski. New equations for heat and mass transfer in turbulent pipe and channel flow. *International Chemical Engineering*, 16(2):359–368, 1976.

[13] K. Gommed, G. Grossman, and M. Koenig. Numerical Study of Absorption in a Laminar Falling Film of Ammonia-Water. *ASHRAE Transactions*, 107(1): 453–462, 2001.

[14] N. I. Grigoreva and V. Ye. Nakoyarkov. Exact Solution of Combined Heat and Mass Transfer during Film Absorption (in Russian). *Izv. Ross. Akad. Nauk, Mekh. Zhidk. Gaza*, 3(5):893–898, 1977.

[15] G. Grossman. Simultaneous Heat and Mass Transfer in Film Absorption Under Laminar Flow. *International Journal of Heat and Mass Transfer*, 26(3):357–371, 1983.

[16] R. I. Hirshburg. *Laminar Film FLow Phenomena, Theory and Application to the Two-Phase Closed Thermosyphon.* PhD thesis, Arizona State University, 1980.

[17] R. I. Hirshburg and L. W. Florschuetz. Laminar Wavy-Film Flow: Part I, Hydrodynamic Analysis. *ASME J. Heat Transfer*, 104(1):452–458, 1982.

[18] R. I. Hirshburg and L. W. Florschuetz. Laminar Wavy-Film Flow: Part II, Condensation and Evaporation. *ASME J. Heat Transfer*, 104(1):459–464, 1982.

[19] G. A. Ibrahim, B. W. Nabhan, and M. Z. Anabtawi. An Investigation into a Falling Film Type Cooling Tower. *International Journal of Refrigeration*, 18(8): 557–564, 1995.

[20] T. Y. Kang, A. Akisawa, and T. Kashiwagi. Analytical Investigation of two Different Absorption Modes: Falling Film and Bubble Types. *International Journal of Refrigeration*, 23(6):430–443, 2000.

[21] N. Kawae, T. Shigechi, K. Kanemaru, and T. Yamada. Water vapor evaporation into laminar film flow of a lithium bromide water solution (influence of variable properties and inlet film thickness on absorption mass transfer rate). *Renewable and Sustainable Energy Reviews*, 18(3):58–70, 1989.

[22] J. D. Killion and S. Garimella. A Critical Review of Models of Coupled Heat and Mass Transfer in Falling-Film Absorption. *International Journal of Refrigeration*, 24(8):755–797, 2001.

[23] J. D. Killion and S. Garimella. Simulation of Pendant Droplets and Falling Films in Horizontal Tube Absorbers. *Journal of Heat Transfer - Transactions of ASME*, 126(6):1003–1013, 2004.

[24] B. Kim. Heat and Mass Transfer in a Falling Film Absorber of Ammonia-Water Absorption Systems. *Heat Transfer Engineering*, 19(3):53–63, 1998.

[25] D. S. Kim and I. Ferreira. Air cooled LiBr water absorption chillers for solar air conditioning in extremely hot weathers. *Energy Conversion Management*, 50 (2009):1018–1025, 2007.

[26] J. Kim and K. Cho. Enhancement of Absorption Performance due to the Film Wave Formation on Vertical Absorber. In *3rd International Symposium on Two-Phase Flow Modelling and Experimentation.*, pages 1–5, 2004.

[27] M. Medrano, M. Bourouis, and A. Coronas. Absorption of water vapour in the falling film of water-lithium bromide inside a vertical tube at air-cooling thermal conditions. *Industrial and Engineering Chemical Fundamentals*, 31(2002):891–898, 2001.

[28] W. A. Miller and M. Keyhan. The Effect of Roll Waves on the Hydrodynamics of Falling Films Observed in Vertical Column Absorbers. In *Proceedings of the ASME Advanced Energy Systems Division 2001*, pages 1–12, 2001.

[29] W. A. Miller and H. Pérez-Blanco. Vertical-Tube Aqueous LiBr Falling Film Absorption Using Advanced Surfaces. In *Proceedings of the International Absorption Heat Pump Conference 1993*, pages 185–202, 1993.

[30] T. Ohuchi, M. Aizawa, R. Kawakami, A. Nishiguchi, T. Hatada, and Y. Kunugi. A Study on a Hot-Water Driven Air-Cooled Absorption Refrigerating Machine. In *Proceedings of the 1994 International Refrigeration Engineering Conference at Purdue*, pages 275–280, 1994.

[31] C. D. Park, T. Nosoko, S. Gima, and S. T. Ro. Wave-augmented mass tranfer in a liquid film falling inside a vertical tube. *International Journal of Heat and Mass Transfer*, 47(2004):2587–2598, 2003.

[32] S. V. Patankar. *Numerical Heat Transfer and Fluid Flow*. Hemisphere Publishing Corporation, 1980.

[33] V. Patnaik. *Combined Heat and Mass Transfer in Wavy-Film Absorption*. PhD thesis, Pennsylvania State University, 1994.

[34] V. Patnaik and H. Pérez-Blanco. Roll Waves in falling films:an approximate treatment of the velicity field. *International Journal of Heat and Fluid Flow*, 17 (1):63–70, 1995.

[35] V. Patnaik and H. Pérez-Blanco. A study of absorption enhancement by wavy film flows. *International Journal of Heat and Fluid Flow*, 17(1):63–70, 1995.

[36] F. W. Pierson and S. Whitaker. Some Theoretical and Experimental Observations of the Wave Structure of Falling Liquid Films. *Journal of Fluid Mechanics*, 16(4):401–407, 1977.

[37] H. Pérez-Blanco. A Model of an Ammonia-Water Falling Film Absorber. *ASHRAE Transactions*, 94(1):467–483, 1988.

[38] T.S. Ravigururajan and A. Bergles. Development and Verification of General Correlations for Pressure Drop and Heat Transfer in Singel-Phase Turbulent Flow in Enhanced Tubes. *Exp. Thermal and Fluid Science*, 13(1):55–70, 1996.

[39] H. Sabir, K. O. Suen, and G. A. Vinnicombe. Investigation of effects of wave motion on the performance of a falling film absorber. *International Journal of Heat and Mass Transfer*, 39(12):2463–2477, 1995.

[40] V. Ya. Shkadov. Wave Flow Regimes of Thin Layer of Viscous Fluid Subject to Gravity. *Fluid Dynamics*, 2(1):43–51, 1967.

[41] V. Ya. Shkadov. Wave Flow Theory for a Thin Viscous Liquid Layer. *Fluid Dynamics*, 3(2):12–15, 1968.

[42] V. Subramaniam and S. Garimella. From Measurements of Hydrodynamics to Computation of Species Transport in Falling Films. *International Journal of Refrigeration*, 32(6):607–626, 2009.

[43] C. Q. Wang, Z. Lu, D. Q. Li, B. Yu-Chi, and Y. G. Sun. Heat and Mass Transfer in Falling Film Generator of Lithium Bromide Absorption Refrigerating Machine. In *Proceedings of the 19th International Congress of Refrigeration*, pages 209–214, 1995.

[44] P. Wayne. Some Theorical and Experimental Observations of the Wave Structure of Falling Film Liquid Films. *Industrial and Engineering Chemical Fundamentals*, 16(4):401–406, 1977.

[45] R. Yang and D. Jou. Heat and Mass Transfer on Wavy Film Absorption Process. *Solar Energy*, 71(3):533–538, 1993.

[46] R. Yang and B. D. Wood. A numerical Modelling of an Absorption Process on a Liquid Falling Film. *Solar Energy*, 48(3):195–198, 1992.

[47] R. Yang and D. Wood. A Numerical Solution of the Wavy Motion on a Falling Liquid Film. *Solar Energy*, 69(1):723–728, 1991.

[48] Ru Yang. *Heat and Mass Transfer in Laminar Wavy Film Absorption with the Presence of Non-Absorbable Gases*. PhD thesis, Arizona State University, 1987.

[49] S. M. Yih and K. Y. Chen. Gas Absorption Into Wavy and Turbulent Falling Films in a Wetted-Wall Column. *Chemical Engineering*, 17(1):123–136, 1982.

[50] R. Zogg, M. Y. Feng, and D. Westphalen. Guide to Developing air-cooled LiBr absorption for light commercial combined heat and power applications. Technical report, United States Department of Energy, 2005.

Chapter 6

Absorption in Presence of Non-Absorbable Gases. Modelling and Numerical Implementation

ABSTRACT

One of the main reasons of the discrepancies between theoretical predictions of absorption phenomena made by mathematical models when they are compared against experimental results under real conditions, are the presence of non-absorbable gases. These non-absorbable gases are inside the shell of the absorption chiller mainly for two reasons: i) air leakages (Oxygen-Nitrogen); ii) gases produced by corrosion (Hydrogen). An experimental setup which reproduces absorption phenomena in vertical falling film has been design and built. In order to evaluate the presence of non-condensable gases, a mass spectrometric study has been performed. Paralelly, a mathematical model of falling film absorption of H_2O by $LiBr$ aqueous solutions which considers the influence of non-absorbable gases has been implemented. The model is semi-empirical, based on Navier Stokes equations together with energy and mass species simplified under the boundary layer hypotheses. Under such conditions, the system of equations in partial derivatives, becomes parabolic and could be solved by means of finite difference method in a step by step procedure. The principles of conservation (mass, momentum, energy and mass species) are applied in both domains (liquid and vapor side). Detailed heat and mass transfer balances are applied at the interface to specify the boundary conditions between liquid and gas phases. Numerically the presence of air results in a pressure drop of water vapor in the interface and consequently it produces a reduction in the heat and mass transfer rates.

6.1 Introduction

Air intrusions into absorption machine can cause unacceptable corrosion problems due to Oxygen (O_2). Therefore, a $LiBr - H_2O$ absorption machine must be essentially hermetic in design, due to the sub-atmospheric working pressures. As we know, working pressures are determined by the vapor pressure characteristics of the working fluids. When no air is present, we can assume that $Pa = 0$ and $P_{H_2O,v}$ is almost constant throughout the vapor zone. However, when non-condensable gases are present, they tend to get swept toward the vapor-liquid interface by the bulk motion of the vapor, and it causes a higher concentration of air in interface more than in bulk. As a consequence of mass-fractions concentrations of air there exists a pressure gradient between interface and bulk vapor side, therefore absorption pressure is reduced to partial water vapor pressure in the interface which significantly reduces the rate of absorption.

The mathematical model described along this chapter is an extension of that one presented in chapter 5. The same set of equations and numerical implementation is used for the coolant fluid, tube wall and falling film domains. The novelty in this model is the addition of the set of equations (5.1-5.4) in the vapor side. Thereby, the mass concentration in the water vapor and air is taken into consideration. Special attention has been paid in applying and conservation of mass and energy balances in the interface that includes both domains (liquid and vapor).

The influence of non-absorbable has been studied experimentally by some authors. Kim et al. [7] did not use any experimental technique in order to evaluate the quantity of non-absorbable gases but they estimate them in an indirect way. The authors use the experimental results of the influence of the inlet solution temperature in the form of Sherwood number combined with the values of the logarithmic mean concentration difference. They conclude that the Sherwood number decreases about 20% when air content increases form 0.5 to 15%. Kim et al. [8] in a later work use two different methods in order to evaluate the volumetric concentration in the absorber. On the one hand, they utilized a mass spectrometer gas analyzer to determine the individual gas species contained in the vapor phase, on the other hand, they used a second method called the "freezing out method" which consists in a sampler container in which the temperature and pressure were measured before and after that the enclosed water vapor was condensed. However results from the mass spectrometry study were discarded from the authors due to inconsistencies in their measures and misinterpretation in their results. The authors conclude that the mass transfer is decreased as much as 20% since the air concentration increase from 0.5 to 14%. Ameel et al. [1] reported experimental results of absorption of water vapor in a vertical liquid film in a solar cooling system. The authors also dismiss the mass spectrometer analysis and they use the "freezing out method" in order measure the air percentage in the vapor phase which varies from 0 to 7% and it has a maximum decrement in the mass

transfer rate of the 35% approximately. Byongjoo and Chunkyu [4] developed an experimental study for horizontal falling film absorbers. The authors reported a variation of non-absorbable gases from 0.17% to 10%. They conclude that the presence of 2% volumetric concentration of air resulted in a 25% reduction in the Nusselt number and 41% reduction in the Sherwood number. As the previous referred authors, Byongjoo and Chunkyu [4] also use the "freezing out method" in order to evaluate the quantity of non-absorbable gases. Yang [14] in his dissertation carry into effect a study of the influence of non absorbable gases using a mass spectrometry study. He reported air concentrations from 4% until 30%. The heat and mass transfer reductions are 50% and 75% respectively when the air concentration is 30%. The table 6.1 shows a summary of the experimental investigation of non-absorbable gases for different authors.

w_{air} %	Percentages of rate absorption reduction (R %)				
	Kim et al. [7]	Kim et al. [8] $\star\star$	Ameel $\star$	Byongjoo $\star$	Yang $\star\star$
0.17				10	
2.0				25	
4.0					30
7.0			35		
10.0	15				
15.0		20			
30.0					50

Table 6.1: Comparison of percentages of rate absorption reduction (R) at different air concentrations for different authors. The symbol $\star$ refers to freezing out method and $*$ refers to mass spectrometry analysis.

On the other hand, the influence of non-absorbable has been also studied numerically. Sabir et al. [10] developed a mathematical model based on energy and mass balances, also they reported that the presence of only 2 % of air causes a reduction of more than six times on the overall effectiveness. Ameel et al. [1] presented analytical methods to estimate the reduction in the absorption phenomena, but it is restricted only in the entrance region of the falling film, where an analytical solution to the governing partial differential equations is possible. Yang and Chen [12] developed a mathematical model for smooth falling film absorption. These authors used set of partial differential equations in its parabolic form and considering only velocity components in the x-direction, such equations are applied in both liquid film and vapor side, they reported that 0.01% reduces drastically (about 95%) the rates of heat and mass transfer. Yang and Wood [13] developed a mathematical model for wavy flow in vertical film absorption. In spite of their results show an improvement respect to the smooth falling film model, the effects of non-absorbable gases in absorption

performance were still severe. The authors reported that only 0.01 % reduces 65% the rates of heat and mass transfer. Medrano et al. [9] proposed an one dimensional empirical model based in three ordinary differential equations. The authors evaluate the influence of the purge velocity during the absorber performance in presence of non-absorbable gases. They reported a 61 % reduction in mass absorption flux when there is an 20 % of air concentration and the maximum purge velocity (30 $m \cdot s^{-1}$). However if purge velocity is null, the reduction in mass absorption flux is about 90 % with the same air concentration. Grossman and Gommed [6] developed a mathematical model based in the energy and diffusion equations that are solved analytically in the entrance region in both the liquid and gas phases. The authors found that 0.1% of air results in 73% of the reduction in the absorption rates. This author performed a previous attempt of a mathematical model [5] of falling film absorption of H_2O by $LiBr$. The model is semi-empirical, based on Navier Stokes equations together with energy and mass species simplified under the boundary layer hypotheses. In order to calculate gradient of air at the interface, the penetration theory was applied in order to avoid a detailed calculation of the gas phase. It was detected that 0.01% of air results in 93.5% of reduction in absorption rate. The table 6.2 shows a summary of the results of the numerical investigations for different authors.

w_{air} %	Percentages of rate absorption reduction (R %)					
	Sabir	Ameel	Yang	Medrano	Grossman	García
0.01			84.96			
0.1					73	93.5
1.0			85.32	18.18	90	93.74
2.0	48					
5.0			85.76	63.63	96.6	94.51
8.0		20				
10.0		26	86.37	81.81		95.37
15.0	53					
20.0				94.44	98.67	
30.0			88.75			99.64
48.0	69					
85.0	80					

Table 6.2: Comparison of percentages of rate absorption reduction (R) at different air concentrations for different authors (Numerical Research).

This chapter presents a new mathematical model that predicts the effects of non-absorbable gases on the performance of the absorption systems. The model is semi-empirical, based on Navier Stokes equations together with energy and mass species simplified under the boundary layer hypotheses. The coupled equations are solved by means of finite difference method in a step by step procedure, and are solved in both the liquid and gas phases. A detailed treatment of the liquid-vapor interface

boundary conditions for the $LiBr$ and H_2O has been implemented (energy and mass balances). The diffusion coefficient for the vapor side was taken from [2, 3, 11].

6.2 Mathematical model

The mathematical model is an extension of that one presented in section 5.2. The same set of equations are discretized in both domains, liquid and vapor. The wavy regime is introduced by solving the Free surface Deflection Equation (see 5.2.1). The Fig. 6.1 shows details of the vertical falling film and its boundary conditions. This mathematical model does not consider the presence of mist flow. All the experimental data has been carefully selected ($Re < 150$) in order to avoid the influence of mist flow.

The following hypotheses are assumed:

i Steady state flow.

ii Physical properties variable only in the flow direction (liquid and vapor).

iii There is no shear stress at the interface.

iv Thermodynamic equilibrium at the interface.

v The flow is laminar or wavy laminar and incompressible (liquid and vapor).

vi The diffusion terms are negligible in the flow direction (liquid and vapor).

vii The convection terms are negligible in the direction orthogonal to the flow.

viii The pressure gradients are negligible (liquid an vapor).

ix The initial velocity in liquid side considered corresponds to fully developed flow.

x The initial velocity in vapor side corresponds a parabolic profile which is function of interfacial velocity.

xi Dufour and Soret effects have not been considered.

xii The domain vapor side behaves like a boundary layer.

xiii The concentration of air at the liquid-vapor interface is dependent of the stream wise coordinate.

xiv Curvature effects due to wavy flow are neglected (capillary waves).

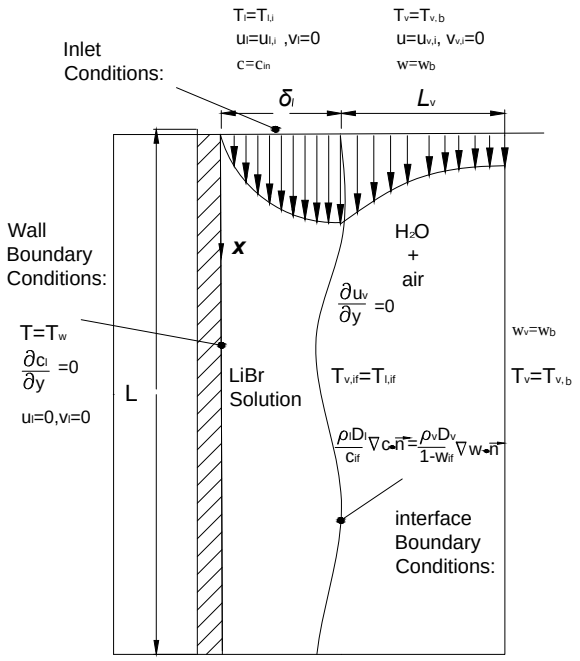

Figure 6.1: Schematic representation of the vertical falling film absorption in presence of non-absorbable gases.

The set of equations in the liquid film side are the same as described in section 5.2, here are rewritten:

$$\frac{\partial u_l}{\partial x} + \frac{\partial v_l}{\partial y} = 0 \tag{6.1}$$

$$u_l \frac{\partial u_l}{\partial x} + v_l \frac{\partial v_l}{\partial y} = gcos(\theta) + \nu_l \frac{\partial^2 u_l}{\partial y^2} \tag{6.2}$$

$$u_l \frac{\partial T_l}{\partial x} + v_l \frac{\partial T_l}{\partial y} = a_l \frac{\partial^2 T_l}{\partial y^2} \tag{6.3}$$

$$u_l \frac{\partial c}{\partial x} + v_l \frac{\partial c}{\partial y} = D_l \frac{\partial^2 c}{\partial y^2} \tag{6.4}$$

And the boundary conditions,

$$x = 0 \begin{cases} T_l = T_{l,in} & (a) \\ c = c_{in} & (b) \\ u_l = u_{l,in} & (c) \\ v_l = 0 & (d) \end{cases} \tag{6.5}$$

$$y = 0 \begin{cases} T = T_w & (a) \\ \nabla c \cdot \vec{n} = 0 & (b) \\ u = 0 & (c) \\ v = 0 & (d) \end{cases} \tag{6.6}$$

$$y = \delta_l \begin{cases} T_{l,if} = f(P_{H_2O,if}, c_{if}) & (a) \\ -\lambda_l \nabla T_l \cdot \vec{n} = h_{abs} \dot{m}_{abs_v} + \lambda_v \nabla T_v \cdot \vec{n} & (b) \\ \frac{\partial u_l}{\partial x} = 0, v = 0 & (c) \end{cases} \tag{6.7}$$

The governing equations in vapor side are:

$$\frac{\partial u_v}{\partial x} + \frac{\partial v_v}{\partial y} = 0 \tag{6.8}$$

$$u_v \frac{\partial u_v}{\partial x} + v_v \frac{\partial v_v}{\partial y} = gcos(\theta) + \nu_v \frac{\partial^2 u_v}{\partial y^2} \tag{6.9}$$

$$u_v \frac{\partial T_v}{\partial x} + v_v \frac{\partial T_v}{\partial y} = a_v \frac{\partial^2 T_v}{\partial y^2} \tag{6.10}$$

$$u_v \frac{\partial w}{\partial x} + v_v \frac{\partial w}{\partial y} = D_v \frac{\partial^2 w}{\partial y^2} \tag{6.11}$$

and the corresponding boundary conditions,

$$x = 0 \begin{cases} T_v = T_{v,b} & (a) \\ w = w_b & (b) \\ u_v = u_{v,in} & (c) \\ v_v = 0 & (d) \end{cases} \tag{6.12}$$

$$y = \delta \begin{cases} T_{v,if} = T_{l,if} & (a) \\ -\frac{\rho_l D_l}{c_{if}} \nabla c \cdot \vec{n} = -\frac{\rho_v D_v}{(1-w_{if})} \nabla w \cdot \vec{n} & (b) \\ u_{v,if} = u_{l,if} & (c) \\ v = 0 & (d) \end{cases} \tag{6.13}$$

$$y = \delta_v \begin{cases} T_v = T_{v,b} & (a) \\ w = w_b & (b) \\ \frac{\partial u_v}{\partial n} = 0 & (c) \end{cases} \tag{6.14}$$

The equations are of liquid and vapor respectively: mass conservation (6.1) and (6.8), momentum conservation (6.2) and (6.9) , energy conservation (6.3) and (6.10) and species conservation (6.4) and (6.11). The equations system in partial differential is solved by means of a change of coordinates taking into account the variation of the thickness of the falling film in the case of the liquid film $\zeta_l = \frac{y_l}{\delta_l}$, and using an appropriate thickness (L_v) in the vapor side domain $\zeta_v = \frac{L_v}{\delta_v}$.

In order to determine the domain in the vapor side, an evaluation of the Pr_v and Sc_v numbers (see section 2.3.3) was performed. The following expression are used in order to evaluate the relation between the boundary layers (momentum, thermal and concentration) [11],

$$\frac{\delta_v}{\delta_{v,c}} = Sc^{1/3} \tag{6.15}$$

$$\frac{\delta_v}{\delta_{v,t}} = Sh^{1/3} \tag{6.16}$$

In the case of vapor phase, $Pr_v > 1$ and $Sc_v < 1$, then $\delta_{t,v} < \delta_v$ and $\delta_{c,v} > \delta_v$. Therefore the domain's length in the vapor side should be $L_v \geq \delta_{c,v}$.

The boundary conditions (6.5) and (6.6) are the same as described in chapter 5. The equation (6.7 a) refers to the equilibrium condition in liquid-vapor interface. Notice that the term $P_{H_2O,if}$ varies its value along the stream-wise direction, (6.7 b) represents the energy balance in the interface, the equation (6.7 c) means null derivative in normal velocity.

The boundary conditions are: equations (6.12 a-d), represents the entry conditions in vapor side for the temperature, concentrations and velocity components, respectively; the equation (6.13 a) represents the temperature of vapor in the interface equal

to temperature of liquid in the interface, the equation (6.13 b) represents the water vapor absorbed through the interface, it is expressed by means the Fick's law in both, liquid and vapor sides, the equation (6.13 c) represents the vapor interface velocity equal to liquid interface velocity; the equation (6.14 a) refers to vapor temperature in bulk, the equation (6.14 a-c) refers to the boundary conditions of the limit of the potential zone in the vapor: temperature and water vapor concentration are known, and null derivative of the velocity normal to boundary layer in vapor side. In order to explain the mechanism by which the presence of non-absorbable gases affects the performance of a vertical falling film absorbers, a schematic representation are depicted in the Fig. 6.3 and the Fig. 6.2. When there is not non-absorbable gases $w_{air} = 0$ then is assumed that $P_{air} = 0$ and then $P_{H_2O,if} = P_{abs}$. However, when non-absorbable gases are present then the total pressure of the absorber is equals the sum of the partial pressures of each of the components $P_t = P_{H_2O} + P_{air}$. Figure 6.2 depicts the pressure gradients in both the bulk vapor phase and the liquid-vapor interface. Notice that $P_{air,if} > P_{air,b}$, this is due to partial pressure depends directly from both the mass concentration and the molecular mass of the species in question (H_2O or air).

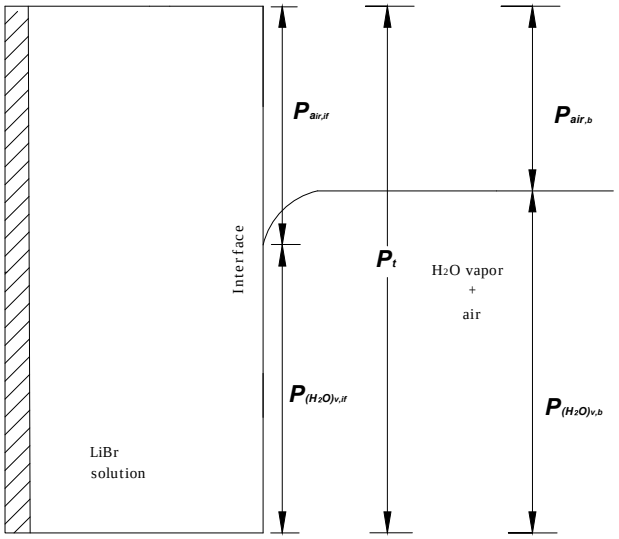

Figure 6.2: Pressure gradients in vapor side along a vertical falling film,(bulk and interface)

The Fig. 6.3 depicts the mass concentrations gradients in both the bulk vapor phase and the liquid-vapor interface. When the absorption is carried out non-absorbable gases into absorbable vapor tends to emigrate from the bulk to the interface due to the bulk motion of the vapor. However, because the gas is not absorbed, it accumulates in the vapor-liquid interface. The expression which relates the mass concentration with the partial pressure in the vapor phase are given by,

$$w_b = \frac{P_{H_2O,b} N_{H_2O}}{P_{H_2O,b} N_{H_2O} + P_{air,b} N_{air}} \tag{6.17}$$

$$w_{if} = \frac{P_{H_2O,if} N_{H_2O}}{P_{H_2O,if} N_{H_2O} + P_{air,if} N_{air}} \tag{6.18}$$

$$P_t = P_{H_2O,b} + P_{a,b} \tag{6.19}$$

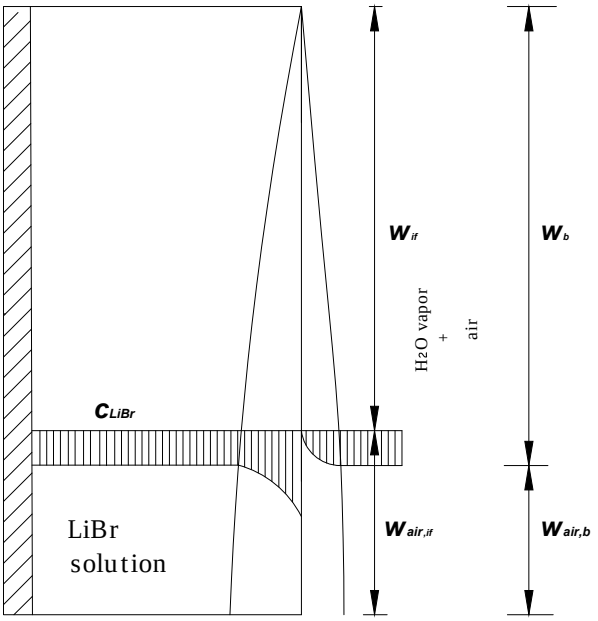

Figure 6.3: Mass concentrations gradients in vapor side along a vertical falling film (bulk and interface)

The set of conservations equations for liquid are (6.1)-(6.4), for vapor (6.8)-(6.11) and the relations (6.17)-(6.19) and the appropriate boundary conditions (6.5)-(6.7) and (6.12)-(6.14) are solved a step-by-step procedure due to the parabolic structure of the equations.

6.2.1 Resolution Procedure

The resolution algorithm for the falling film absorption model based on boundary layer hypotheses in presence of non absorbable gases is described below.

1. Coupled resolution of momentum (6.2) and mass (6.1) conservation equations, for obtaining the values of the components of the velocity. Calculation of the boundary layer thickness considering a smooth film thickness.
2. The Free Surface Deflection Equation is solved in order to obtain wave profile which is function Re and dimensionless surface tension parameter γ. The new boundary layer thickness as function of wave profile is calculated and introduced.
3. Calculation of $c_{l,if}$ based on a mass balance the equation (6.13 b) and using secant method.
4. Calculation of w_{if} based on a energy balance the equation (6.6 b) and using secant method.
5. Calculation of temperatures fields T_l and T_v using equations (6.3) and (6.10) respectively, as well as concentration field in vapor side w using equation (6.11).
6. Calculation of the mass absorbed from the point of view of the vapor side ($\dot{m}_{abs,v}$ right side of equation 6.13 b), calculation the energy balance at the interface using equation ((6.7 b)).
7. Check if energy balance is accomplished, the equation ((6.7 b)). If so, go to the next step, if not back to the point 4.
8. Calculation of concentration field in liquid side c_l using the equation (6.4).
9. Calculation of the mass absorbed from the point of view of the liquid side $\dot{m}_{abs,l}$ (left side of equation (6.13b)), calculation the energy balance at the interface using equation (6.7 b).
10. Check if mass balance in the interface is accomplished, (see the equation 6.13 b),
    $\left| \frac{\rho_l D_l}{c_{if}} \nabla c \cdot \vec{n} - \frac{\rho_v D_v}{(1-w_{if})} \nabla w \cdot \vec{n} \right| < \varepsilon$. If so, go to the next step, if not back to the point 3.

11. Check if mass absorbed between two consecutive iterations has not variation $|\frac{\dot{m}_{abs}-\dot{m}_{abs_o}}{\dot{m}_{abs}}| \leq \varepsilon$. If so, go to the next row, if not back to the point 1.

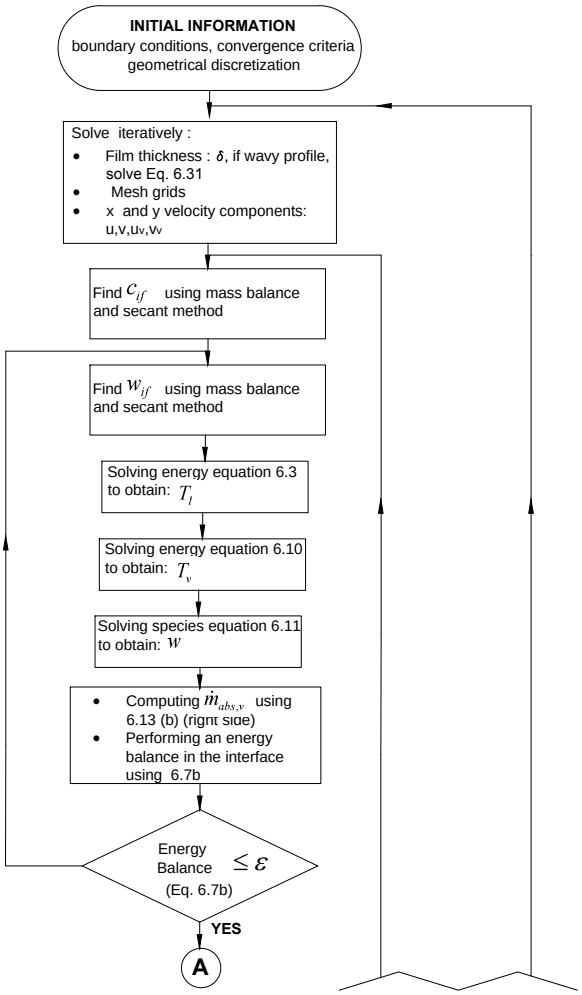

Figure 6.4: Resolution algorithm for boundary layer mathematical model falling film absorption in presence of non absorbable gases (A).

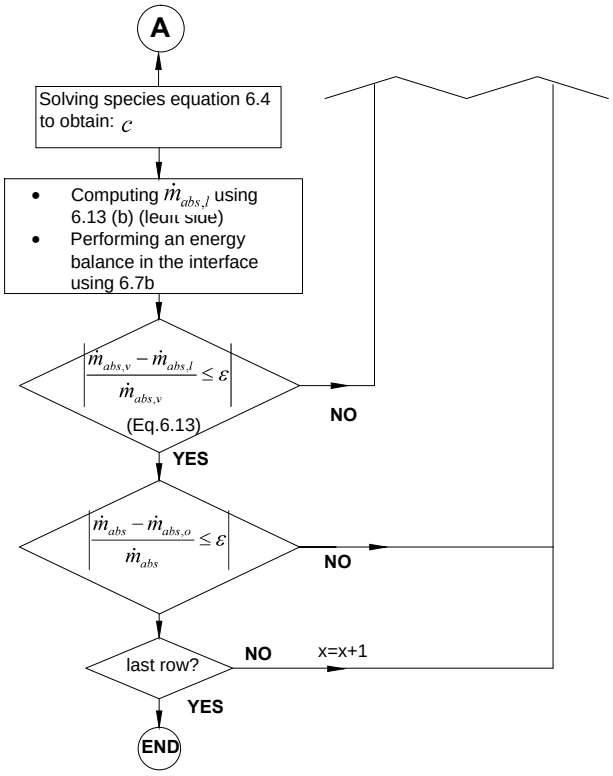

Figure 6.5: Resolution algorithm for boundary layer mathematical model falling film absorption in presence of non absorbable gases (B).

6.2.2 Mass Diffusivity in the Water-Vapor Mixture

Unlike the other two molecular transport coefficients for gases, the viscosity and thermal conductivity, the gas-phase diffusion coefficient is dependent on the pressure and the temperature. Specifically, the gas-phase diffusion coefficient is an inverse function of total system pressure $D_v \propto \frac{1}{P_v}$ and a $\frac{3}{2}$ power-law function of the absolute temperature $D_v \propto T_v^{\frac{3}{2}}$. Since the working pressures in $LiBr$ absorbers are relative low (see Fig. 2.3), it is expected that D_v values were higher in $H_2O - LiBr$ solution

than in atmospheric pressure. The diffusion coefficient of the mixture water vapor-air is obtained from [2, 11], using the expression proposed by Hireschfelder,

$$D_v = \frac{0.001858 T_v \frac{3}{2} \left[\frac{1}{N_{air}} + \frac{1}{N_{H_2O}} \right]^{1/2}}{P r_{AB}^2 \Omega_D} \tag{6.20}$$

The above equation is used for extrapolating experimental data and for moderate ranges of pressure, up to 25 atm. For lower pressures the following expression is used:

$$D_{v,T_2,P_2} = D_{v,T_1,P_1} \left(\frac{P_1}{P_2} \right) \left(\frac{T_1}{T_2} \right)^{\frac{3}{2}} \frac{\Omega_{D|T_1}}{\Omega_{D|T_2}} \tag{6.21}$$

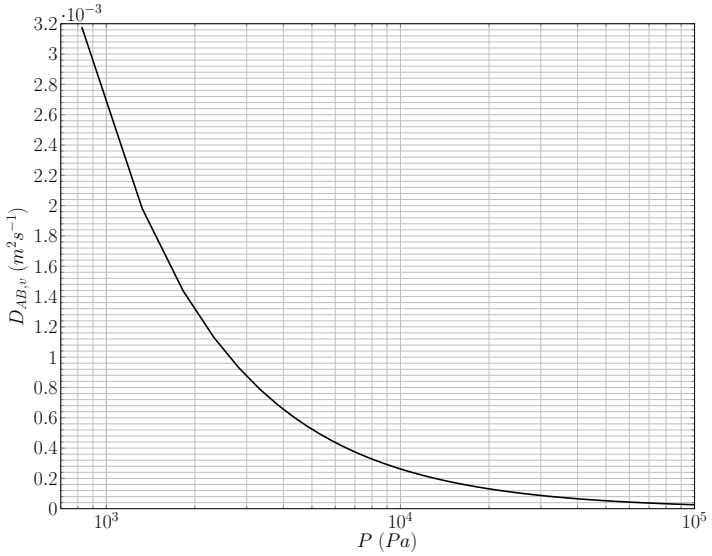

Figure 6.6: Vapor-air mass diffusivity values against pressure at constant temperature

The values of the mass diffusion D_v of water vapor into air is about two orders of magnitude higher than the diffusion at atmospheric pressure (see Fig 6.6, $D_{AB,v} =$

$2.588e^{-5}$ at $P_v = 1$ ata and $D_v = 1.9794^{-3}$ at $P_v = 1300$ Pa) and six orders of magnitude higher than the mass diffusion coefficient in $H_2O - LiBr$ in liquid film $\left(\frac{D_L}{D_v}\right) \approx 7.42e^{-7}$.

6.3 Numerical verification

Likewise that in sections 4.3 and 5.3 a numerical verification study has been performed. The convergence and truncation errors are evaluated. The working conditions are the same as used in table 4.1. The air concentration used in this test is $w_{air} = 0.1\%$.

6.3.1 Convergence Errors

Since the mathematical model presented in this chapter is an extension of that one presented in chapter 5 some of the convergence criteria already have been tested. In this section are evaluated the new convergence criteria that are included in the new algorithm resolution.

1. The relative error in the change of velocity in the vapor side between two consecutive iterations when momentum conservation and continuity equations are solved ε_1.
2. The mass imbalance at the interface between the values of $\dot{m}_{abs,l}$ and $\dot{m}_{abs,s}$ (see equation (6.13 b)), ε_2.
3. The relative error in the mass absorbed between two consecutive iterations at the interface ε_3.

The table 6.3 shows the results for the ε_1 criteria, The asymptotic results are achieved when $\varepsilon_1 \approx 1e-7$.

The table 6.4 shows the results for the ε_2 and ε_3 criteria. The asymptotic results are achieved when $\varepsilon_2 \approx 1e-4$ and $\varepsilon_3 \approx 1e-5$.

6.3.2 Truncation Errors (Discretization)

The table 6.5 shows the results for the test of discretization errors. N_x represents the grid nodes along the x coordinate (x coordinate are the same in liquid an vapor sides). $N_{y,v}$ represents the grid nodes along the y_v coordinate in vapor side. Δx and Δy_v are the steps calculations in the x and y_y directions. The asymptotic result is almost reached when $N_x = 1600$ and $N_{y,v} = 600$.

ε_1	$\dot{Q}_{abs,c}$ (W)	$\dot{Q}_{abs,v}$ (W)	$\dot{m}_{abs}$ $(kg \cdot s^{-1})$	c_{out} $(\%LiBr)$	T_{out} $(^\circ C)$
1e-1	1.0873E+003	5.9028E+002	2.3035E-004	5.9477E+001	3.7909E+001
1e-2	1.0874E+003	5.9032E+002	2.3037E-004	5.9477E+001	3.7909E+001
1e-3	1.0874E+003	5.9032E+002	2.3037E-004	5.9477E+001	3.7909E+001
1e-4	1.0876E+003	5.9046E+002	2.3042E-004	5.9477E+001	3.7909E+001
1e-5	1.0878E+003	5.9064E+002	2.3049E-004	5.9476E+001	3.7910E+001
1e-6	1.0877E+003	5.9059E+002	2.3047E-004	5.9476E+001	3.7910E+001
1e-7	1.0313E+003	5.3915E+002	2.1016E-004	5.9638E+001	3.7265E+001
1e-8	1.0315E+003	5.3940E+002	2.1026E-004	5.9637E+001	3.7271E+001
1e-9	1.0315E+003	5.3940E+002	2.1026E-004	5.9637E+001	3.7271E+001

Table 6.3: Convergence study depending on ε_1 (change of velocity in vapor side) for the boundary layer based model in presence of non-absorbable gases

ε_2	ε_3	$\dot{Q}_{abs,c}$ (W)	$\dot{Q}_{abs,v}$ (W)	$\dot{m}$ $(kg \cdot s^{-1})$	c_{out} $(\%LiBr)$	T_{out} $(^\circ C)$
$1.0e^{-1}$	$1.0e^{-1}$	1.031598e+03	5.394943e+02	2.102967e-04	5.963670e+01	3.727162e+01
$1.0e^{-2}$	$1.0e^{-1}$	1.031550e+03	5.394103e+02	2.102635e-04	5.963680e+01	3.727064e+01
$1.0e^{-3}$	$1.0e^{-1}$	1.031549e+03	5.394105e+02	2.102636e-04	5.963680e+01	3.727067e+01
$1.0e^{-4}$	$1.0e^{-1}$	1.031544e+03	5.394031e+02	2.102607e-04	5.963681e+01	3.727062e+01
$1.0e^{-5}$	$1.0e^{-1}$	1.031540e+03	5.393966e+02	2.102582e-04	5.963682e+01	3.727055e+01
$1.0e^{-1}$	$1.0e^{-2}$	1.031598e+03	5.394943e+02	2.102967e-04	5.963670e+01	3.727162e+01
$1.0e^{-2}$	$1.0e^{-2}$	1.031550e+03	5.394103e+02	2.102635e-04	5.963680e+01	3.727064e+01
$1.0e^{-3}$	$1.0e^{-2}$	1.031549e+03	5.394105e+02	2.102636e-04	5.963680e+01	3.727067e+01
$1.0e^{-4}$	$1.0e^{-2}$	1.031544e+03	5.394031e+02	2.102607e-04	5.963681e+01	3.727062e+01
$1.0e^{-5}$	$1.0e^{-2}$	1.031540e+03	5.393966e+02	2.102582e-04	5.963682e+01	3.727055e+01
$1.0e^{-1}$	$1.0e^{-3}$	1.031598e+03	5.394949e+02	2.102969e-04	5.963670e+01	3.727164e+01
$1.0e^{-2}$	$1.0e^{-3}$	1.031550e+03	5.394111e+02	2.102638e-04	5.963680e+01	3.727065e+01
$1.0e^{-3}$	$1.0e^{-3}$	1.031549e+03	5.394113e+02	2.102639e-04	5.963680e+01	3.727069e+01
$1.0e^{-4}$	$1.0e^{-3}$	1.031544e+03	5.394038e+02	2.102610e-04	5.963681e+01	3.727064e+01
$1.0e^{-5}$	$1.0e^{-3}$	1.031540e+03	5.393973e+02	2.102585e-04	5.963682e+01	3.727057e+01
$1.0e^{-1}$	$1.0e^{-4}$	1.031597e+03	5.394963e+02	2.102975e-04	5.963670e+01	3.727168e+01
$1.0e^{-2}$	$1.0e^{-4}$	1.031550e+03	5.394111e+02	2.102639e-04	5.963680e+01	3.727066e+01
$1.0e^{-3}$	$1.0e^{-4}$	1.031549e+03	5.394113e+02	2.102640e-04	5.963680e+01	3.727069e+01
$1.0e^{-4}$	$1.0e^{-4}$	1.031544e+03	5.394039e+02	2.102610e-04	5.963681e+01	3.727064e+01
$1.0e^{-5}$	$1.0e^{-4}$	1.031540e+03	5.393974e+02	2.102585e-04	5.963682e+01	3.727057e+01
$1.0e^{-1}$	$1.0e^{-5}$	1.031597e+03	5.394963e+02	2.102975e-04	5.963670e+01	3.727168e+01
$1.0e^{-2}$	$1.0e^{-5}$	1.031550e+03	5.394111e+02	2.102639e-04	5.963680e+01	3.727066e+01
$1.0e^{-3}$	$1.0e^{-5}$	1.031549e+03	5.394113e+02	2.102640e-04	5.963680e+01	3.727069e+01
$1.0e^{-4}$	$1.0e^{-5}$	1.031544e+03	5.394039e+02	2.102610e-04	5.963681e+01	3.727064e+01
$1.0e^{-5}$	$1.0e^{-5}$	1.031540e+03	5.393974e+02	2.102585e-04	5.963682e+01	3.727057e+01

Table 6.4: Convergence study depending on ε_2 (mass imbalance in the interface) and ε_3 (relative error in mass absorbed) for the boundary layer based model

N_x	$N_{y,v}$	Δx (m)	Δy_v (m)	$\dot{Q}_{abs,c}$ (W)	$\dot{Q}_{abs,v}$ (W)	$\dot{m}_{abs}$ $(kg \cdot s^{-1})$	c_{out} $(\%LiBr)$	T_{out} $(^\circ C)$
100	300	0.01	$9.3805e^{-6}$	1.033256e+03	5.428663e+02	2.116410e-04	5.963264e+01	3.731100e+01
200	300	$5e^3$	$9.3805e^{-6}$	1.034954e+03	5.446131e+02	2.123166e-04	5.963059e+01	3.731005e+01
400	300	$2.5e^{-3}$	$9.3805e^{-6}$	1.034777e+03	5.443115e+02	2.121959e-04	5.963096e+01	3.730723e+01
800	300	$1.25e^{-3}$	$9.3805e^{-6}$	1.031778e+03	5.400071e+02	2.104976e-04	5.963610e+01	3.727933e+01
1600	300	$6.25e^{-3}$	$9.3805e^{-6}$	7.226066e+02	5.291861e+02	2.055482e-04	5.839948e+01	3.633567e+01
3200	300	$3.125e^{-3}$	$9.3805e^{-6}$	1.011260e+03	5.153598e+02	2.007833e-04	5.966551e+01	3.720517e+01
100	600	0.01	$9.3805e^{-6}$	1.033255e+03	5.428640e+02	2.116402e-04	5.963264e+01	3.731098e+01
200	600	$5e^3$	$4.69025e-6$	1.034950e+03	5.446045e+02	2.123133e-04	5.963060e+01	3.730992e+01
400	600	$2.5e^{-3}$	$4.69025e-6$	1.034755e+03	5.442513e+02	2.121725e-04	5.963103e+01	3.730634e+01
800	600	$1.25e^{-3}$	$4.69025e-6$	1.031521e+03	5.393461e+02	2.102384e-04	5.963688e+01	3.726979e+01
1600	600	$6.25e^{-3}$	$4.69025e-6$	9.960461e+03	4.823591e+02	1.935587e-04	5.97510e+01	3.70953e+01
3200	600	$3.125e^{-3}$	$4.69025e-6$	9.968851e+02	4.875458e+02	1.898659e-04	5.969860e+01	3.689539e+01
6400	600	$1.562e{-}4$	$4.69025e-6$	9.968629e+02	4.877287e+02	1.893652e-04	5.963653e+01	3.689976e+01
100	800	0.01	$2.345125e-6$	1.033254e+03	5.428634e+02	2.116400e-04	5.963264e+01	3.731097e+01
200	800	$5e^3$	$2.345125e-6$	1.034950e+03	5.446026e+02	2.123126e-04	5.963060e+01	3.730989e+01
400	800	$2.5e^{-3}$	$2.345125e-6$	1.034751e+03	5.442394e+02	2.121678e-04	5.963104e+01	3.730615e+01
800	800	$1.25e^{-3}$	$2.345125e-6$	1.031476e+03	5.392160e+02	2.101875e-04	5.963703e+01	3.726778e+01
1600	800	$6.25e^{-3}$	$2.345125e-6$	9.950026e+03	4.8212908e+02	1.891397e-04	5.989837e+01	3.682462e+01
3200	800	$3.125e^{-3}$	$2.345125e-6$	9.937293e+02	4.808918e+02	1.872568e-04	5.970651e+01	3.681388e+01
6400	800	$1.562e^{-4}$	$2.345125e-6$	9.937799e+02	4.808905e+02	1.872795e-04	5.976869e+01	3.681372e+01
200	1100	$5e^3$	$1.50088e-6$	1.034949e+03	5.446011e+02	2.123121e-04	5.963060e+01	3.730987e+01
400	1100	$2.5e^{-3}$	$1.50088e-6$	1.034748e+03	5.442305e+02	2.121644e-04	5.963105e+01	3.730600e+01
800	1100	$1.25e^{-3}$	$1.50088e-6$	1.031445e+03	5.391223e+02	2.101508e-04	5.963715e+01	3.726628e+01
1600	1100	$6.25e^{-3}$	$1.50088e-6$	9.9339739e+03	4.805712e+02	1.88576e-04	5.975923e+01	3.681444e+01
3200	1100	$3.125e^{-3}$	$1.50088e-6$	9.937799e+02	4.808559e+02	1.8725688e-04	5.970651e+01	3.6813887e+01
6400	1100	$1.562e^{-4}$	$1.50088e-6$	9.934073e+02	4.803487e+02	1.876315e-04	5.979651e+01	3.687237e+01

Table 6.5: Convergence study depending on N_x (grid nodes in x direction) and N_y (grid nodes in y direction) for the boundary layer based model

6.4 Conclusions

A mathematical model has been implemented in order to evaluate the presence of non-absorbable gases into the absorption performance. This model is an extension of that one presented in chapter 5. The same set of equations have been implemented in the vapor side. Special attention has been paid in the following aspects:

- It has been applied detailed heat and mass transfer balances at the interface to specify the boundary conditions between liquid and gas phases.
- The calculation of the mass diffusivity in the vapor side ($D_{AB,v}$) at sub-atmospheric pressures is an important issue, since the value of D_{AB} is inversely proportional to the value of P_t.

Nomenclature

a	thermal diffusivity, $m^2\ s^{-1}$
c	$LiBr$ mass fraction concentration
D	mass diffusivity, $m^2\ s^{-1}$
g	acceleration due to gravity, $m\ s^{-2}$
h	specific enthalpy, $J\ kg^{-1}$
L_v	thickness in vapor domain, m
$\dot{m}$	mass flow , $kg\ s^{-1}$
N	molecular mass, $mol\ kg^{-1}$
P	pressure, Pa
R	percentage of reduction in absorption rate, %
r_{AB}	collision diameter, $\AA$
T	temperature, K
u	velocity profile x axis direction, $m\ s^{-1}$
v	velocity profile y axis direction, $m\ s^{-1}$
w	H_2O mass fraction concentration in vapor side
x	coordinate, m
y	coordinate, m

Greek symbols

δ	hydrodynamic film thickness, m
δ_t	thermal film thickness, m
δ_c	concentration film thickness, m
ε	convergence accuracy criterion

ζ	dimensionless y coordinate
θ	inclination angle, rad
ν	kinematic viscosity, $m^2\ s^{-1}$
λ	thermal conductivity, $W\ m^{-1}\ K^{-1}$
Ω_D	collision integral, $kg\ m^{-3}$

Dimensionless Groups

Pr	Prandlt Number, $Pr = \frac{Cp\mu}{\lambda}$
Sh	Sherwood Number, $Sh = \frac{\kappa\delta}{D}$
Sc	Sherwood Number, $Sc = \frac{\nu}{D}$

Subscripts

air	air component
abs	absorption
b	bulk
c	coolant fluid
H_2O	water component
if	interface conditions
in	inlet conditions, inner
l	liquid phase in LiBr solution
out	outlet conditions, outer
t	total
v	vapor phase
W	wall solid tube

Bibliography

[1] T. A. Ameel, H. M. Habib, and B. D. Wood. Effects of Nonabsorbable Gas on Interfacial Heat and Mass Transfer for the Entrance Region of a Falling Film Absorber. *Journal of Solar Energy Engineering*, 118(1996):45–49, 1996.

[2] C. O. Bennett and J. E. Myers. *Momentum, Heat, and Mass Transfer.* McGraw-Hill, 1975.

[3] R. B. Bird, W. E. Stewart, and E. N. Lightfoot. *Fenómenos de Transporte.* REVERTÉ, 1973.

[4] K. Byongjoo and L. Chunkyu. Non-Absorbable Gas Effects on Heat and Mass Transfer in Falling Film Absorption. *Journal of Mechanical Science and Technology*, 17(4):581–589, 2003.

[5] E. García-Rivera, J. Castro, J. Farnós, and A. Oliva. Modelling of Absorption of H2O Vapor in Falling Film of LiBr Aqueous Solution in Vertical Tubes with Presence of Non-Condensables. In *Proceedings of the 10th IIR Gustav Lorentzen Natural Working Fluids Conference*, pages 263–270, 2012.

[6] G. Grossman and K. Gommed. Heat and mass transfer in film absorption in the presence of non-absorbable gases. *International Journal of Heat and Mass Transfer*, 40(15):3595–3606, 1997.

[7] K. J. Kim, N. S. Berman, D. S. C. Chau, and B. D. Wood. Absorption of Water vapour into falling films of aqueous lithium bromide. *International Journal of Refrigeration*, 18(7):486–494, 1995.

[8] K. J. Kim, T. A. Ameel, and B. D. Wood. Performance Evaluations of LiCl and LiBr Absorber Design Applications in the Open Cycle Absorption Refrigeration System. *Journal of Solar Energy Engineering*, 119(1997):165–173, 1996.

[9] M. Medrano, M. Bourouis, H. Perez-Blanco, and A. Coronas. A simple model for falling film absorption on vertical tubes in the presence of non-absorbables. *Industrial and Engineering Chemical Fundamentals*, 26(2003):108–116, 2003.

[10] H. Sabir, K. O. Suen, and G. A. Vinnicombe. Investigation of effects of wave motion on the performance of a falling film absorber. *International Journal of Heat and Mass Transfer*, 39(12):2463–2477, 1995.

[11] J. R. Welty, C. E. Wicks, R. E. Wilson, and G. L. Rorrer. *Fundamentals of momentum, Heat and Mass Transfer.* Willey, 2008.

[12] R. Yang and J. H. Chen. A Numerical Solution of the non-absorbable effects on the falling liquid film absorption. *Wärme und Stoffübertragung*, 26(1991): 219–223, 1991.

[13] R. Yang and D. Wood. A Numerical Solution of the Wavy Motion on a Falling Liquid Film. *Solar Energy*, 69(1):723–728, 1991.

[14] Ru Yang. *Heat and Mass Transfer in Laminar Wavy Film Absorption with the Presence of Non-Absorbable Gases.* PhD thesis, Arizona State University, 1987.

Chapter 7

Experimental Validation

ABSTRACT

In this chapter are shown the experimental results and its comparison against the numerical results. The chapter is divided in two main parts: i) the first part deals with the validation of the falling film absorption in vertical tubes in presence of wavy regime and mist flow. In this section a parametric study of the influence of governing variables during absorption phenomena has been performed; ii) the second part deals with the experimental validation of falling film absorption in vertical tubes in presence of wavy regime and non-absorbable gases. In this second part a parametric study has been performed by evaluating the influence of different air concentrations in the absorber performance. The studies results in each of the sections are widely discussed.

7.1 Introduction

The first part of the experimental results presented along this chapter were obtained by performing a parametric study. The influence of the principal variables that determine the absorption performance were evaluated. Most of the experimental points have been obtained free of mist flow except inlet mas flow and inlet $LiBr$ concentrations studies (mist flow is present when $Re > 150$, see chapter 3.4.4).

The variables that have been considered are as follows:

- The influence of the inlet mass flow ($\dot{m}_{l,in}$). Since the rest of the inlet condition remains constant the Re number changes as $\dot{m}_{l,in}$. During this test it can be appreciated the behavior of the mist flow.
- The influence of absorption pressure (P_{abs}). It is controlled through the generation process (see chapter 3.2). This test is free of mist flow since $Re \approx 100$.
- The influence of inlet solution concentration ($T_{l,in}$). Two different test have been performed at different Reynolds numbers. $Re \approx 250$ (mist flow is present) and $Re \approx 140$ (free of mist flow).
- The influence of inlet coolant solution ($T_{c,in}$). This test is performed using $Re \approx 115$ (free of mist flow).
- The influence of inlet mass concentration ($c_{l,in}$). This test is performed using $Re \approx 120$ (free of mist flow).
- A final set of experimental data has been obtained at different $Re = 90 \div 200$ number and different inlet mass concentration $c_{l,in} = 57.3\% \div 61\%$. This data were used in order to perform the fully validation of the numerical models. Mist flow was present when $Re > 150$.

The experimental data obtained in the above point were used for validating the numerical model described in the chapter 5. The experimental validation is performed by comparing wavy and smooth numerical solutions (smooth numerical solution does not include the solution of the equation (5.20)). The mathematical model described in section 4.2 (1D-empirical model) has not been evaluated in this chapter. The main reason is that such mathematical model does not predicts satisfactory the absorption phenomena when $Re > 80$.

The second part of the experimental investigation is focused in the influence of the non-absorbable gases in the absorption performance.

The experimental study is described as follows:

- Numerical results at different air concentrations $w_{air} = 1.98\% \div 37.31\%$ and different Reynolds $Re = 85 \div 145$ number. All the data presented in this study are free of mist flow.
- The influence of inlet coolant solution ($T_{c,in}$) under the influence of non-absorbable gases. This test was performed ta $Re \approx 78$(free of mist flow).

The experimental data obtained in the first point of the above list were used for validating the numerical model described in chapter 6. The experimental validation is performed against wavy numerical model.

7.1.1 Falling film mass flow rate effect

In order to evaluate the effects of solution mass flow in the absorption performance the rest of influential variables have been set as follows: $T_{l,in} = T_{l,sat}$, $P_{abs} = 1300$ Pa, $c_{in} = 60.3\%$, $T_{c,in} = 32.5^{o}C$. Relatively high inlet coolant temperatures are selected in order to simulate air-cooling thermal conditions. The coolant mass flow rate ($\dot{m}_{c,in}$) is large enough ($700\% - 1000\%$) with respect to solution inlet mass flow rate ($\dot{m}_{l,in}$) in order to provide enough cooling capacity.

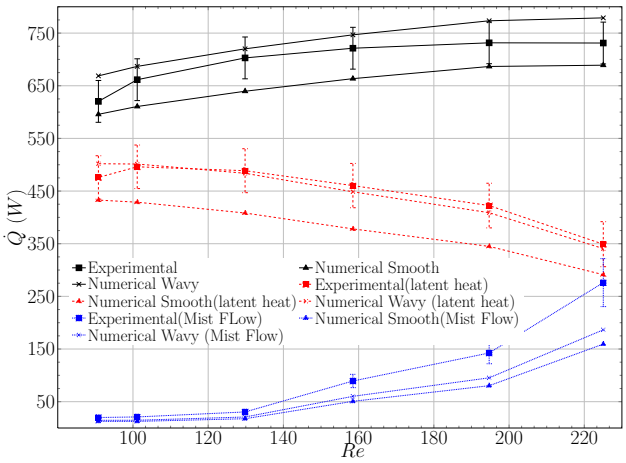

Figure 7.1: Effects of the inlet mass flow rate ($\dot{m}_{l,in}$) in heat load ($\dot{Q}_{abs,c}$, black dots), energy input through the interface ($\dot{Q}_{abs,v}$, red dots) and enthalpy contribution of mist flow ($\dot{Q}_{abs,l}$, blue dots) transfer rates. Experimental and numerical results (smooth and wavy models).

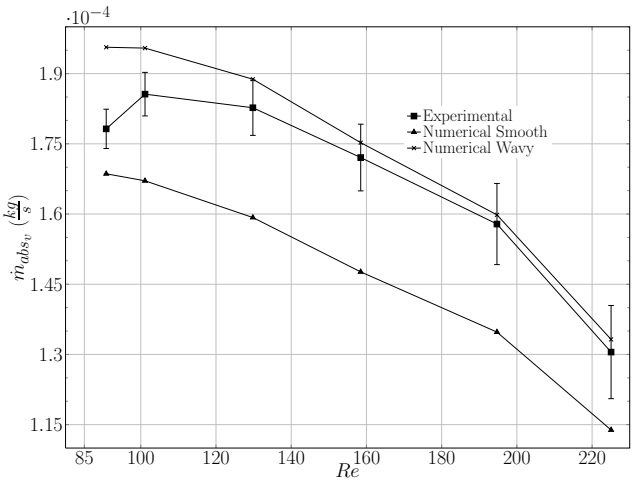

Figure 7.2: Effects of inlet solution mass flow rate ($\dot{m}_{l,in}$) in the mass of absorption transfer rate ($\dot{m}_{abs,l}$). Experimental and numerical results (smooth and wavy models).

The Reynolds number in falling film is manipulated by increasing or decreasing the inlet mass flow. This work presents Re numbers between $90 - 250$, which are the expected values in absorption machines. Re influence on heat and mass transfer rates are shown in Fig. 7.1 and Fig. 7.2 respectively.

The graph in Fig. 7.2 represent the influence of Re number in mass absorption rate. Experimentally the mass absorbed presents its maximum value at $Re \approx 100$, from this point the higher is the Re, the less is the mass absorbed. Numerical results presents similar tendency. The wavy numerical model matches better than the smooth model. Other experimental investigations [25-27] show that increasing slope reaches its maximum value about $Re \approx 70$ in a range of $Re = 15 \div 100$.

The graph in Fig. 7.1 represents the influence of Re number in heat rate of absorption. The graph represents the following results:

1. The heat contribution due to mist flow ($\dot{Q}_{abs,l}$) increases with Re number (see section 3.4.4). While the Re values are between $160 - 240$ the two numerical models underestimate the experimental data. However as from $Re \approx 130$ numerical and experimental results matches very well.

2. Energy input through the interface in the film interface side ($\dot{Q}_{abs,v}$) decreases as Re increases and it presents its maximum value when $Re \approx 100$. (This

heat contribution depends directly from the mass absorbed). The wavy model matches with experimental data, while smooth model results are below the experimental data.

3. The heat load removed directly for the coolant fluid ($\dot{Q}_{abs,c}$) increases as Re increases while $Re = 90 \div 160$, from values about $Re \approx 160$ heat load keeps almost constant, this is due to heat contribution of the mist flow. The wavy model slightly overestimates experimental results, while smooth model results are below the experimental data.

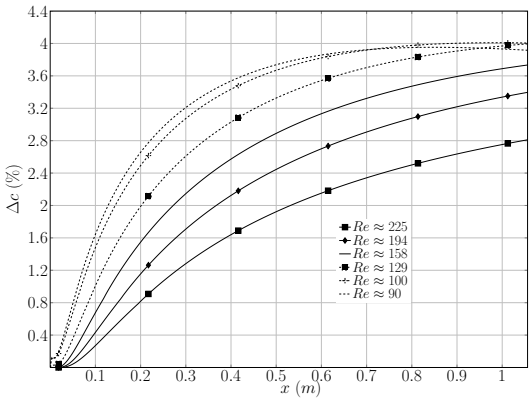

Figure 7.3: Numerical results of concentration Driving Potential (Δc) evolution along falling film at different Re number.

The above results show that there is an optimal Reynolds number where heat and mass transfer rates are maximum. Higher values of Re than the optimal, entails in a decrement in absorption performance. In order to explain this phenomena a numerical study is presented in the Figs. 7.3, 7.4 and 7.5.

The Fig. 7.3 and the Fig. 7.4 represents the concentration and pressure driving potentials along the falling film, respectively. Both graphs present a similar behavior. The driving potentials decreases as the Re increases. The trend changes when $Re \approx 90 \div 100$, when both graphs intersect each other. When increasing the Re number, it results also an increase of the interface velocity of the film. As consequence, there is a reduction in the exposure time between liquid film and gas phase and a reduction of the absorption phenomena. This agree with to the penetration theory [1], which states that the mass transfer coefficient is directly inversely proportional to the exposure time. The Fig. 7.5 represents the concentration boundary layer thickness (y_{δ_c}) along

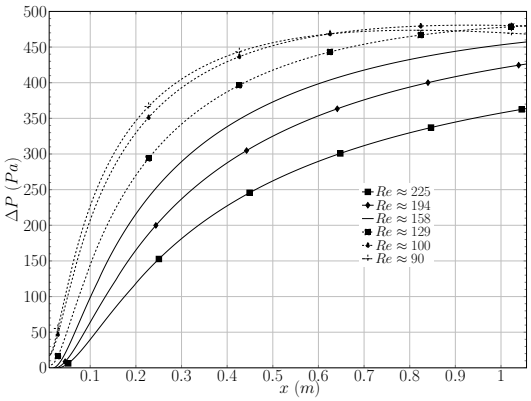

Figure 7.4: Numerical results of pressure Driving Potential (ΔP) evolution along falling film at different Re number.

the falling film. y_{δ_c} is defined as the distance from the film surface where the following relation is accomplished:

$$\frac{c - c_{if}}{c_w - c_{if}} = 0.99 \tag{7.1}$$

The more is the δ_c thickness, the higher is the mass absorbed. Notice that from values of $Re \approx 150$ the value of δ_c decreases and this trend is augmented at higher values of Re.

(7.2)

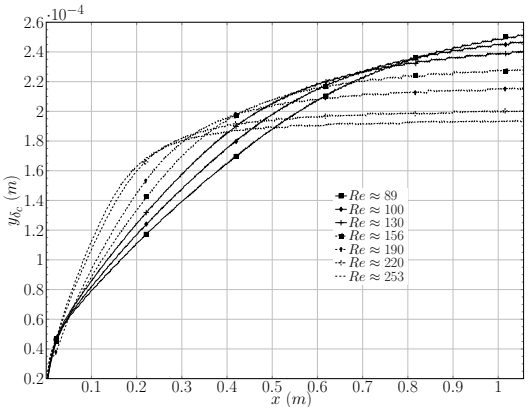

Figure 7.5: Numerical results of maximum concentration distance (y_{δ_c}) along falling film.

7.1.2 Absorption pressure effects

The driving force for mass transfer through the vapor-liquid interface can be expressed as the difference between the partial pressure of water vapor in the vapor side of interface (the gas phase is composed of water vapor and an unknown amount of non-absorbable gases) and the equilibrium pressure in the bulk solution at the given temperature and concentration $P_{l,b} = f(T_{l,b}, c_{l,b})$. If it is assumed that there is no presence of non-absorbable gases, the pressure vapor keeps constant along to all the vapor domain (bulk and interface vapor sides). Then, the pressure driving force can be expressed by,

$$\Delta P = P_{abs} - P_{l,b} \tag{7.3}$$

Notice that the second term of the right hand side of the equation (7.3) ($P_{l,b}$) varies its value along the falling film, therefore the higher is the absorption pressure, the greater is the potential for vapor transfer to the falling film.

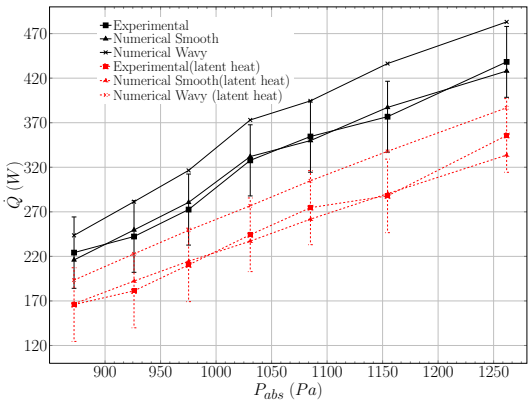

Figure 7.6: Influence of absorption pressure (P_{abs}) in both heat load ($\dot{Q}_{abs,c}$, black dots) and energy input through the interface ($\dot{Q}_{abs,v}$, red dots) transfer rates. Experimental and numerical results (smooth and wavy models).

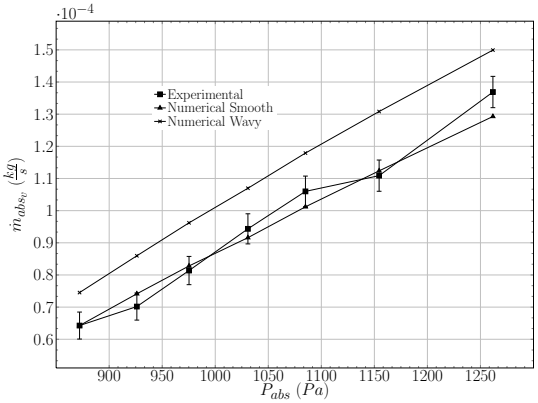

Figure 7.7: Influence of the absorption pressure (P_{abs}) in the mass of absorption transfer rate ($\dot{m}_{abs,v}$). Experimental and numerical results (smooth and wavy models)

The following conditions are fixed $T_{s,in} \approx T_{sat}$, $Re \approx 100$, $c_{in} = 57.3\%$, $T_c \approx 32°C$, the absorption pressure (P_{abs}) varies from 850 to 1260 Pa. In this situation there is no presence of mist flow ($Re < 150$).

The Fig. 7.6 shows the influence of absorption pressure in the heat load rates ($\dot{Q}_{abs,c}$) and the energy input through the interface ($\dot{Q}_{abs,v}$).

The absorber pressure varies from 850 to 1260 Pa and as a consequence there is an increment in the values of $\dot{Q}_{abs,c}$ from 224 to 438 W (95%) and a increment in the values of $\dot{Q}_{abs,v}$ from 165 to 355 W (115%). On the other hand, the Fig. 7.7 represents the influence of absorption pressure in the mass transfer rates ($\dot{m}_{abs,v}$). As expected, the flux mass has the same tendency as the energy input through the interface. Both Numerical models follow the same behavior than experimental data. Wavy model tends to over-predict the experimental data in this test. (between $8-16\%$ in $\dot{Q}_{abs,c}$ and $8-22\%$ for $\dot{Q}_{abs,v}$). As mentioned before mass and heat fluxes depend largely of the driving forces, that is why is always interesting to observe their behavior. The Fig. 7.8 and the Fig. 7.9 represent the experimental driving potential forces for the pressure and concentrations. As expected both graphics show a positive tendency when absorption pressure is increased.

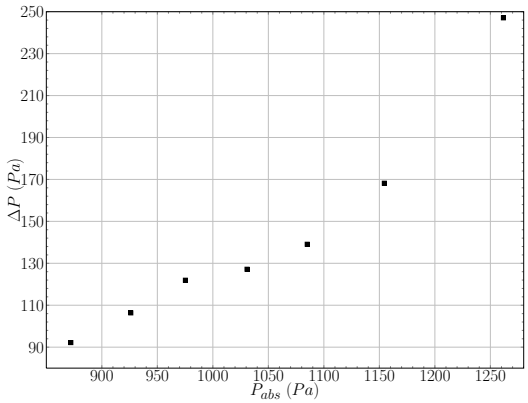

Figure 7.8: Influence of the absorption pressure in the pressure (P_{abs}) driving potential (ΔP) for experimental data.

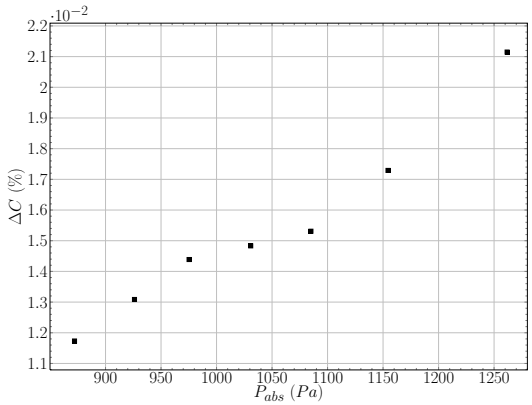

Figure 7.9: Influence of the absorption pressure (P_{abs}) in the concentration driving potential (Δc) for the experimental data.

7.1.3 Inlet solution temperature effects

All experimental tests so far were performed by approximating the inlet solution temperature to the equilibrium conditions ($T_{l,in} \approx T_{sat}$). The equilibrium solution inlet temperature depends of both mass solution concentration and absorption pressure $T_{l,in} = f(c_{in}, P_{abs})$. Theoretically any variation above or below (subcooling or super heating) from equilibrium conditions should be reflected in the performance of the absorber. In this section the subcooling effects have been taken into account. During the absorption process in a falling film it is assumed that the interface liquid-vapor is under equilibrium conditions. It means that $LiBr$ concentration and temperature at the interface are such that the vapor pressure of water in the solution is always equal to the partial pressure of H_2O vapor in the vapor phase.

When the inlet temperature solution is approximately equal to the saturation temperature ($T_{l,in} \approx T_{sat}$) equilibrium conditions at interface are reached early. In contrast when there is a subcooling degree, in which there is a process of reaching equilibrium that promotes the absorption of water vapor into the liquid interface.

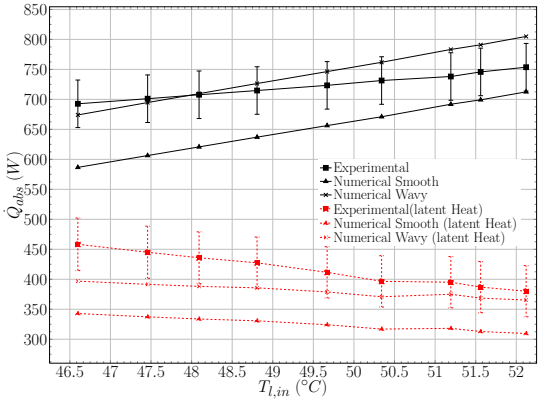

Figure 7.10: Influence of the inlet solution temperature ($T_{l,in}$) in both heat load ($\dot{Q}_{abs,c}$, black dots) and energy input through the interface ($\dot{Q}_{abs,v}$, red dots) transfer rates for $Re \approx 250$. Experimental and numerical results (smooth and wavy models).

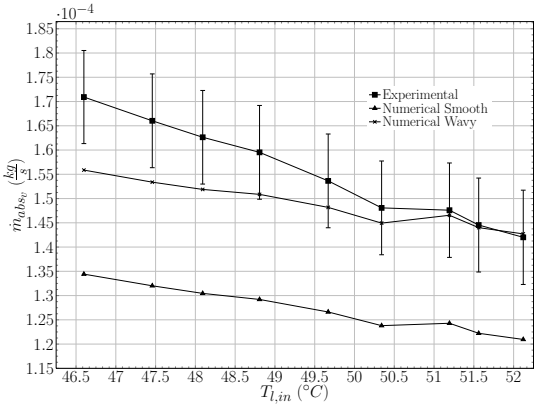

Figure 7.11: Influence of inlet solution temperature ($T_{l,in}$) in the mass absorption transfer rate ($\dot{m}_{abs,v}$) for $Re \approx 250$. Experimental and numerical results (smooth and wavy models).

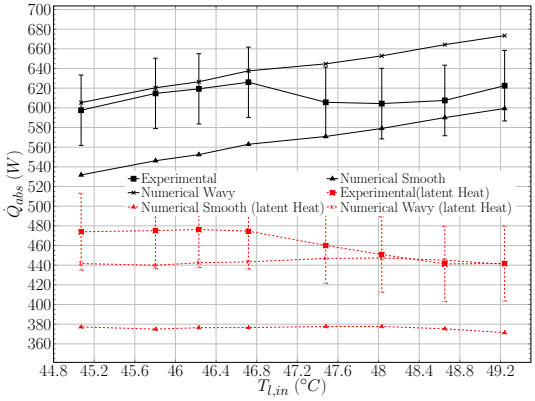

Figure 7.12: Influence of the inlet solution temperature ($T_{l,in}$) in both heat load ($\dot{Q}_{abs,c}$, black dots) and energy input through the interface ($\dot{Q}_{abs,v}$, red dots) transfer rates for $Re \approx 140$. Experimental and numerical results (smooth and wavy models).

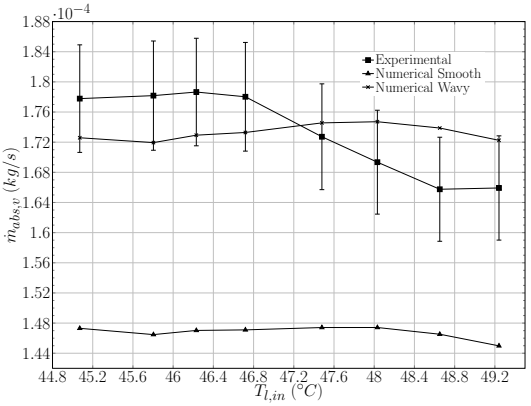

Figure 7.13: Influence of the inlet solution temperature ($T_{l,in}$) in the mass absorption transfer rate ($\dot{m}_{abs,v}$) for $Re \approx 140$. Experimental and numerical results (smooth and wavy models).

The Fig. 7.10 and the Fig. 7.11 depict experimental and numerical results in the heat and mass transfer rates under the influence of subcooling effects. Both graphics show a marked improvement in the absorption process: the mass and heat absorbed

present about 20% of increment. The heat load present a opposite trend, it decreases as $T_{l,in}$ decreases. This is due to the more is the subcooling degree, the less is the sensible heat in the liquid that is entering in the absorber. In spite of the energy input through the interface is increasing this is not large enough to revert this tendency.

Nevertheless the Fig. 7.12 and the Fig. 7.13 describe a different behavior when subcooling grade is manipulated. It hardly show variations in the heat and mass transfer rates. It is also interesting to punctuate that the numerical results also predict this behavior. The only difference between both tests is the Re number ($Re \approx 200$ for the Fig. 7.10 and $Re \approx 140$ for the Fig. 7.12). However, the experimental data with $Re > 150$ has presence of mist flow, and this fact could be give an erratic interpretation of the results. In other words, the enhancement of the absorption process could be due to the presence of mist flow, rather than an increment of Re. In order to solve this ambiguity a numerical study is performed. The Fig. 7.14 and the Fig. 7.15 depict numerical simulations under the influence of subcooling, in a range of Re and non-presence of mist flow. The results of the numerical study show that the influence of the subcooling is conditioned by the regime flow. Flow regimes between $Re \div 70 - 140$ show a negative tendency when increasing the subcooling degree, this is not only useless for the enhancement of the absorption rates, but also it seems to degrade the absorption performance. Such tendency is reverted starting from $Re > 140$. From this point subcooling has a positive influence in the absorption rates.

Through this study there are some points worth of accentuating: a) the subcooling has a positive influence of the absorber performance when $Re \geq 140$, b) in spite of the positive influence of subcooling degree as from $Re > 140$ it can be seen that the influence of flow regime is greater than the influence of subcooling, see the plots for $Re \approx 170, 220$ and 250, where the maximum mass absorbed is plotted at $Tl, in \approx 45.5°C$ and $Re \approx 170$.

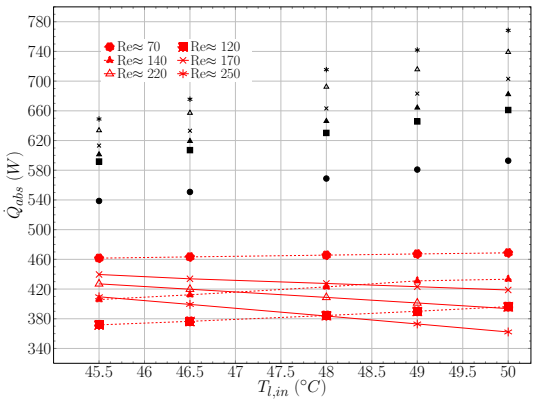

Figure 7.14: Numerical study of the influence of the inlet solution temperature (Tl, in) in both heat load ($\dot{Q}_{abs,c}$, black dots) and energy input through the interface ($\dot{Q}_{abs,v}$, red dots) transfer rates at different flow regimes.

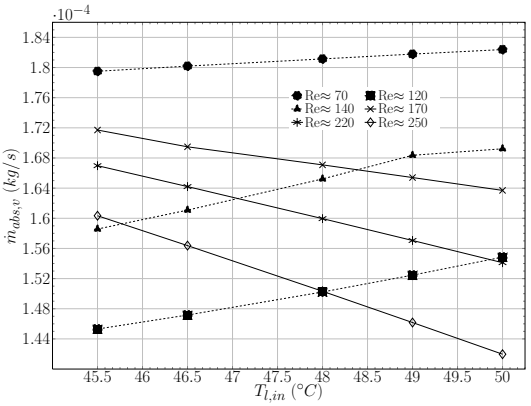

Figure 7.15: Numerical study of the influence of the inlet solution temperature (Tl, in) in mass absorption rates ($\dot{m}_{abs,v}$) at different flow regimes.

7.1.4 Inlet coolant temperature effects.

The coolant temperature ($T_{c,in}$) plays an important role in the performance of the absorber on an air-cooled absorption chiller. Tis temperature ($T_{c,in}$) and absorber pressure (P_{abs}) are directly related to each other, therefore if the value of ($T_{c,in}$) is

close to the value of ($T_{l,out}$) the absorber loses capacity of removing heat.

The variables used for evaluating coolant temperature effects are: $P_{abs} \approx 1200$ Pa, $Re \approx 115$, $c_{l,in} \approx 59.50\%$, $T_{c,in} \approx 30.1 - 41.7^{o}C$. The Fig. 7.16 shows the behavior of both, the heat load ($\dot{Q}_{abs,c}$) and the energy input through the interface ($\dot{Q}_{abs,v}$): when the value of $T_{c,in}$ decreases the values of $\dot{Q}_{abs,c}$ and $\dot{Q}_{abs,v}$ increase. The mass transfer rates ($\dot{m}_{abs,v}$) exhibit the same tendency of the energy input through the interface, see the Fig. 7.17, it increases its value as $T_{c_{in}}$ decreases. The agreement between experimental data and numerical results is quite acceptable, however numerical results of the wavy model show a better matching.

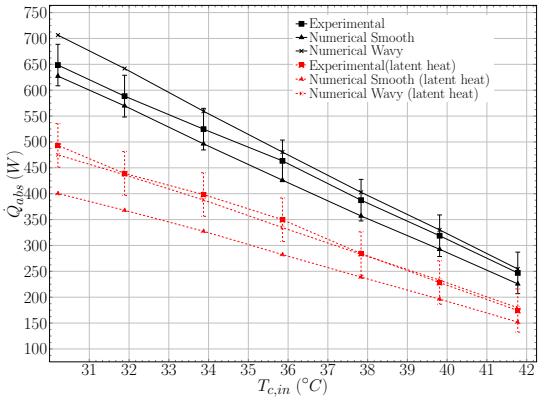

Figure 7.16: Influence of inlet the coolant temperature ($T_{c,in}$) in both heat load ($\dot{Q}_{abs,c}$, black dots) and energy input through the interface ($\dot{Q}_{abs,v}$, red dots) transfer rates. Experimental and numerical results (smooth and wavy models).

The Fig. 7.18 and the Fig. 7.19 show the influence of inlet coolant temperature ($T_{c,in}$) in pressure and concentration driving potentials. As mentioned in the previous paragraph, the value of $T_{c,in,}$ is closely related with the the value of P_{abs}. The lower is the value of $T_{c,in}$ the higher is the capacity of removing heat from the liquid film. Therefore temperature profile in liquid film also decreases due to the heat removed. This causes that the equilibrium pressure in the bulk film also decreases and the capacity of absorption is augmented, however this increment in the driving potential pressure is transitory due to the more vapor water is absorbed, the less is the pressure in the absorber. The inlet coolant temperature ($T_{c,in}$) is advantageous for the performance of the absorber as long as it is accompanied by an increase of the vapor generation that compensates the extra water vapor that has been absorbed and keeps the absorption pressure constant.

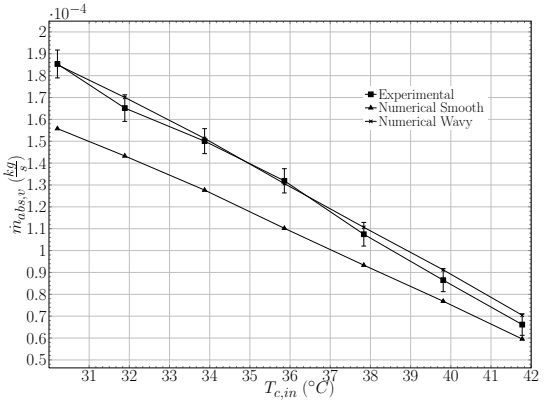

Figure 7.17: Influence of the inlet coolant temperature ($T_{c,in}$) in the mass absorption transfer rate ($\dot{m}_{abs,v}$). Experimental and numerical results (smooth and wavy models).

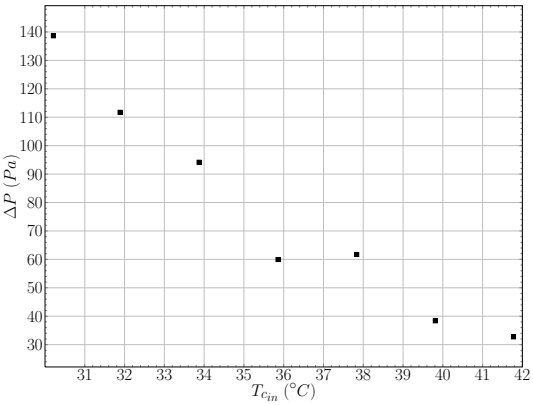

Figure 7.18: Influence of the coolant inlet temperature ($T_{c,in}$) in the pressure driving force (ΔP), experimental results.

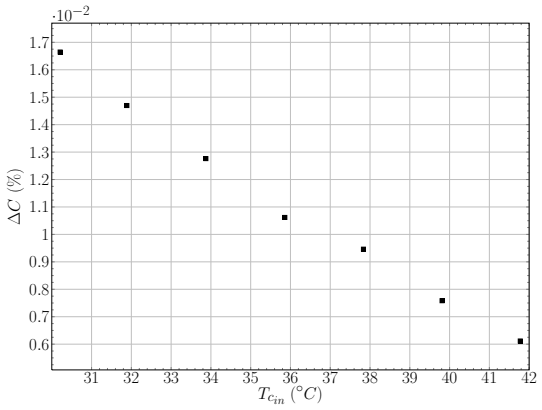

Figure 7.19: Influence of the coolant inlet temperature ($T_{c,in}$) in the concentration driving force (ΔP), experimental results.

7.1.5 Mass concentration effects

The mass concentration is a variable that can not be directly settled in a absorption machine, but it is settled as a consequence of the equilibrium and performance of the rest of the components. The variables used for evaluating coolant temperature effects are: $P_{abs} \approx 1300$ Pa, $Re \approx 125$, $T_{c,in} \approx 30.0°C$.

The variation of the inlet solution concentration ($c_{l,in}$) and its effect to the mass and the heat transfer rates, respectively are shown in the Fig. 7.20 and the Fig. 7.21. When increasing concentration in a mixture, the equilibrium pressure decreases, which produces higher driving forces, see the Fig. 7.22 and the Fig. 7.23. The final conclusion is that the higher is the inlet mass concentration, the best performance of the absorber, however too high concentrations ($c_{l,in} > 61$) also entail a higher crystallization risks.

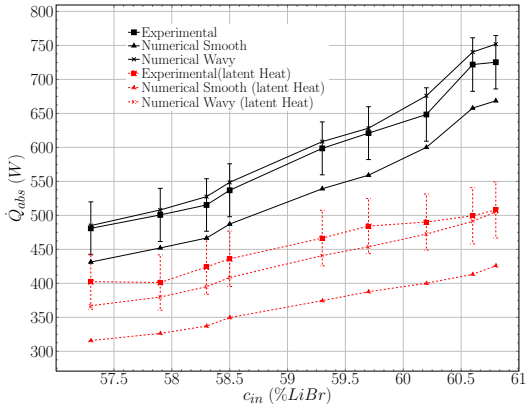

Figure 7.20: Influence of the inlet solution concentration ($c_{l,in}$) in both heat load ($\dot{Q}_{abs,c}$, black dots) and energy input through the interface ($\dot{Q}_{abs,v}$, red dots) transfer rates. Experimental and numerical results (smooth and wavy models).

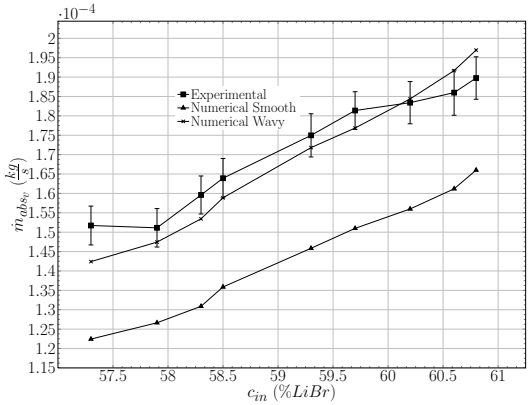

Figure 7.21: Influence of the inlet solution concentration ($c_{l,in}$) in the mass absorption transfer rate ($\dot{m}_{abs,l}$). Experimental and numerical results (smooth and wavy models).

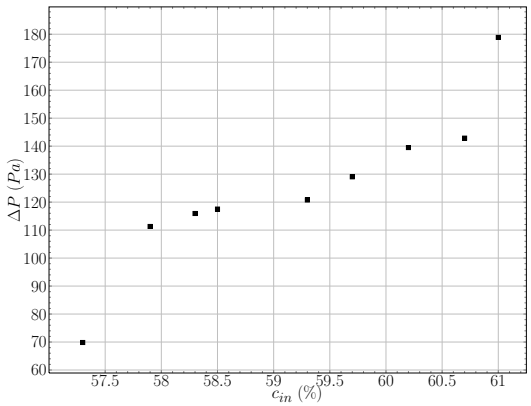

Figure 7.22: Influence of the inlet mass concentration ($c_{l,in}$) in the pressure driving force (ΔP), experimental data.

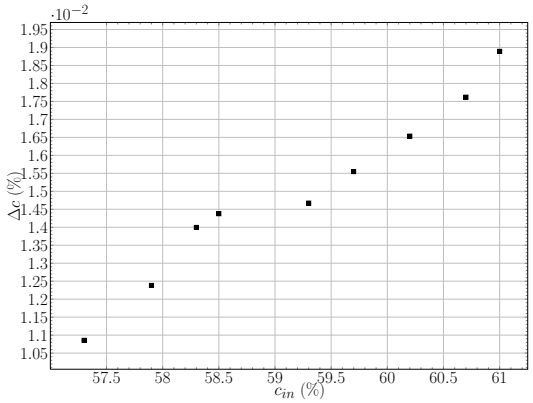

Figure 7.23: Influence of the inlet mass concentration ($c_{l,in}$) in the concentration driving force (Δc), experimental data.

7.1.6 Experimental Results for the Fully Validation of the Numerical Model

In the above sections 7.1.1-7.1.5 all the experimental results have been carefully performed in order to obtain vapor water with no presence of mist flow (when it was possible). However the mathematical model described on section 5.2 has been modi-

fied on order to consider the presence of mist flow. A set of experimental tests have been carried out under a wide range of flow regimes $Re \approx 70 \div 250$ and concentrations $c_{l,in} \approx 57 - 61\%$.

The Fig. 7.24 shows the comparison of the heat load ($\dot{Q}_{abs,c}$) between experimental data and numerical results (wavy and smooth models). The red errors lines represents the maximum error calculated in the uncertainty analysis ($\pm 8\%$). However not all the points are inside this range of errors. The blue errors lines represent the maximum error between experimental and numerical wavy model ($\pm 14\%$). The experimental data compared against the wavy mathematical model shows the following errors: maximum error 14%, minimum error 0.490% and average error 6.68%. In contrast the smooth shows the following errors: maximum error 11.12%, minimum error 0.3% and average error 5.29%.

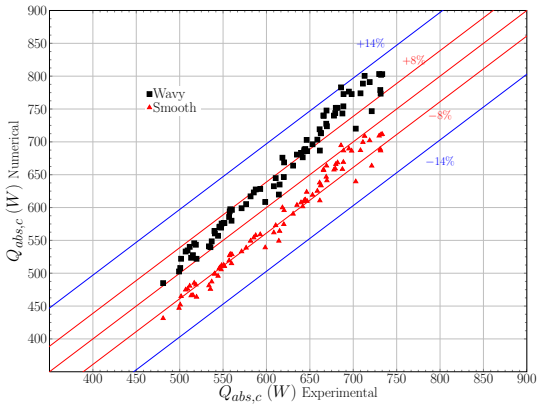

Figure 7.24: Comparison of the heat load ($\dot{Q}_{abs,c}$) between numerical and experimental results at different flow regimes and different inlet solution mass concentration (red dots refers smooth model, black dots refers to wavy model).

The Fig. 7.25 shows the comparison between experimental and numerical results obtained from the mathematical models corresponding to the energy input through the interface ($\dot{Q}_{abs,v}$). The maximum error associated to uncertainty analysis is ($\pm 11.5\%$). All the data corresponding to the wavy model are inside this range of error. The experimental data compared against the wavy mathematical model shows the following errors: maximum error 11.2%, minimum error 0.15% and average error 5.03%. In contrast the smooth shows the following errors: maximum error 25.4%, minimum error 6.9% and average error 16.94%.

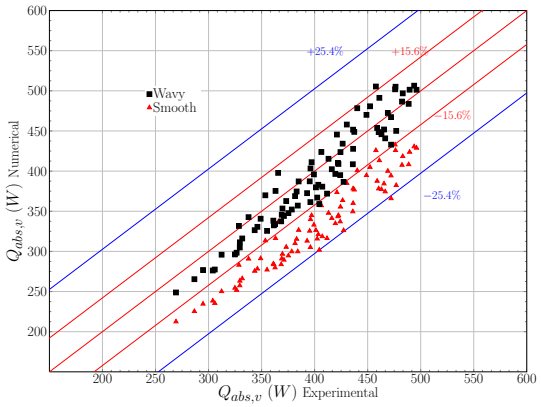

Figure 7.25: Comparison of the energy input through the interface ($\dot{Q}_{abs,v}$) between numerical and experimental results at different flow regimes and different inlet solution mass concentration ($c_{l,in}$) (red dots refers smooth model, black dots refers to wavy model).

The Fig. 7.26 shows the comparison between experimental and numerical results obtained from the mathematical models corresponding to the vapor water mass absorbed. The maximum error associated to uncertainty analysis is (±11.5%). Most of the wavy numerical data are inside this range of error.The experimental data compared against the wavy mathematical model shows the following errors: maximum error 15.15%, minimum error 0.05% and average error 5.43%. In contrast the smooth shows the following errors: maximum error 22.21%, minimum error 3.0% and average error 13.66%.

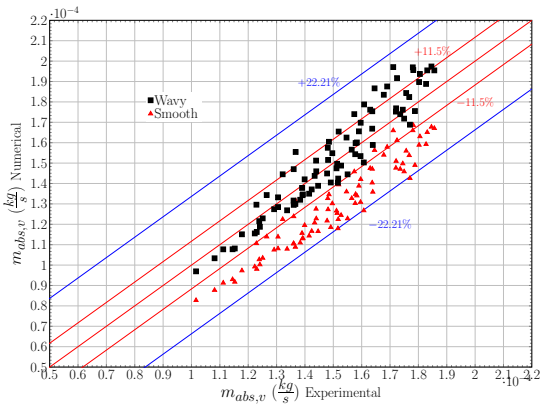

Figure 7.26: Comparison of the mass absorbed ($\dot{m}_{abs,v}$) between numerical and experimental results at different flow regimes and different inlet solution mass concentration ($c_{l,in}$) (red dots refers smooth model, black dots refers to wavy model).

7.2 Influence Non-absorbable gases

7.2.1 Baseline Test

Along this manuscript we have been highlighting the importance and complexity of the vacuum technology. Given the fact that there is no perfect vacuum it is necessary to establish the minimum quantity of air that the experimental setup allows. In order to determine the allowable minimum of air, the following tests were performed:

- A mass spectrometry measurements during a absorption experimental performance. The experimental unit was previously purged to obtain a quality vacuum. During the experiment the purge pumps keep turned off. The results were: $w_{air} = 1.851\%$ ($N_2 = 1.481\%$,$O_2 = 0.326\%$, $Ar = 0.042\%$).
- The same experiment was performed, but the purge pumps keep turned on during the whole test. The results are: $w_{air} = 1.857\%$ ($N_2 = 1.367\%$, $O_2 = 0.458\%$, $Ar = 0.029\%$).

From the tests performed it can be concluded: i) there are not leakages in the experimental setup; ii) the air that remains into the absorber is due to the vacuum pumps that are not able to remove it. The table 7.1 shows the nominal characteristics in which the baseline test were performed.

Geometry	
Outer Diameter Tube (m)	0.022
Inner Diameter Tube (m)	0.018
Length Tube (m)	1.0
Working Conditions (LiBr Aqueous solution)	
Inlet Re number	$Re \approx$ 80-120
Inlet temperature ($^\circ$ C)	Saturation conditions (T_{sat})
Inlet LiBr concentration ($\%LiBr$)	60.2
Absorption pressure (Pa)	1300
Working Conditions Coolant Side	
Inlet solution mass flow ($kg \cdot s^{-1}$)	$11.9e^{-1}$
Inlet temperature ($^\circ$ C)	29.914

Table 7.1: Geometry and working conditions for the reference case.

The same working conditions are used for different air concentrations in order to evaluate the effect of non-absorbable gases in absorption performance.

7.2.2 Influence of Non-Absorbable concentrations

Taking as reference the baseline case in the above section, a parametric study has been performed considering the influence of non-absorbable gases. The minimum air concentration achievable in the experimental setup is, $w_{air} \approx 1.85\%$. From this point, atmospheric air is introduced in steps of different concentrations until a maximum value of $w_{air} \approx 63\%$.

The Fig. 7.27 depicts the experimental results for the mass absorbed at different Re numbers and different air concentrations. As expected, the higher is the air concentration the more is the reduction of the rate of absorption. Same behavior is observed in Fig. 7.29 and Fig. 7.29 where the energy input through the interface and heat load are represented.

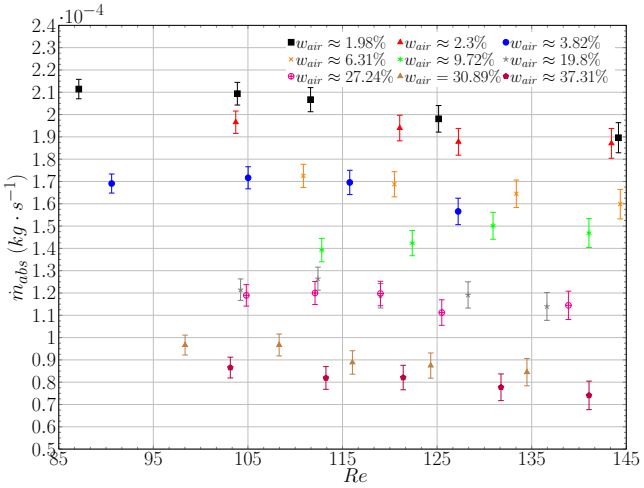

Figure 7.27: Experimental results of the mass absorbed ($\dot{m}_{abs}$) at different Re Number and under the influence of different air concentrations (w_{air})

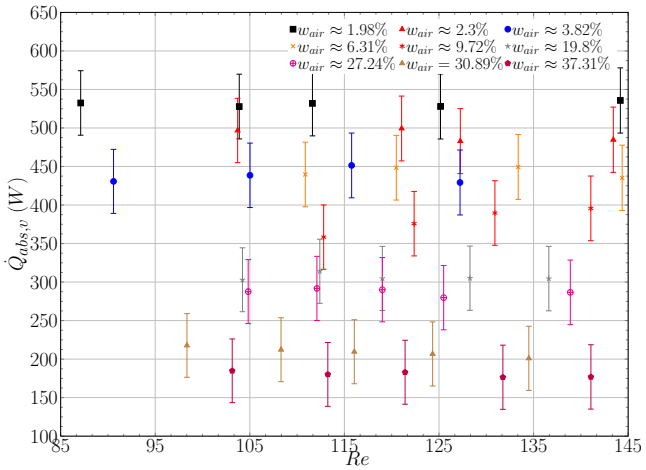

Figure 7.28: Experimental results of the energy input through the interface ($\dot{Q}_{abs,v}$) at different Re Number and under the influence of different air concentrations (w_{air}).

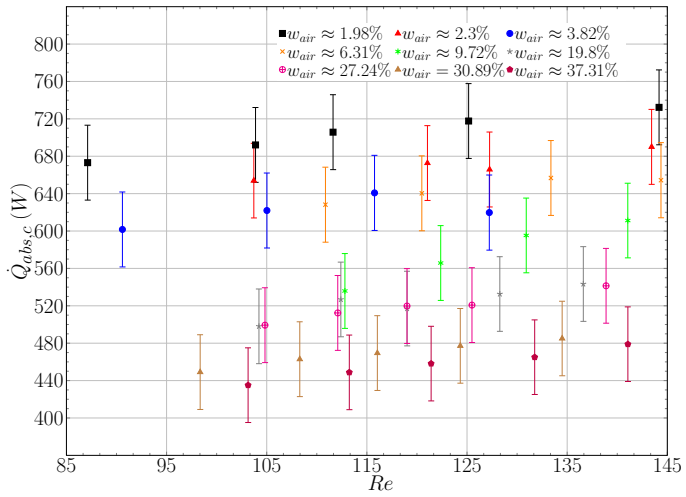

Figure 7.29: Experimental results of the heat load ($\dot{Q}_{abs,c}$) at different Re Number and under the influence of different air concentrations (w_{air}).

The table 7.2 summarizes the average percentages of rate absorption reduction (R) at different air concentrations for mass and heat absorbed.

w_{air}	$\dot{m}_{abs}\ (kg \cdot s^{-1})$	$(R)\%$	$\dot{Q}_{abs,v}\ (W)$	$(R)\%$
1.98	1.982-004		531.139	
2.3	1.913E-004	3.476	490.932	7.569
3.82	1.665E-004	15.999	439.863	17.184
6.31	1.663E-004	16.060	443.168	16.562
9.72	1.415E-004	28.576	377.139	28.994
19.8	1.199E-004	39.489	306.250	42.340
27.24	1.168E-004	41.044	287.181	45.931
30.89	9.083E-005	54.180	209.439	60.567
37.31	8.047E-005	59.404	180.252	66.063

Table 7.2: Comparison of average percentages of rate absorption reduction ($R\%$) for heat and mass absorbed at different air concentrations

When the air concentration value is $w_{air} \approx 1.98\%$ corresponds to a partial pressure of air of about $P_{air} \approx 16.2$ Pa when the total pressure value is $P_t = 1300$ Pa. The maximum value of $w_{air} \approx 37.31\%$ corresponds to a air partial pressure of about $P_{air} \approx$

351.09 Pa, at this point the percentage of reduction is near to 60%. As expected, absorption performance degrades as air concentration increases. The principal cause of such effect is due to reduction of the partial pressure of (H_2O). The higher is w_{air} the lower is P_{H_2O}, even worse given that $P_{H20,if} < P_{H20,b}$ (see Fig. 6.2).

7.2.3 Influence of Subcooling degree

An experimental study has been performed in order to evaluate the influence of subcooling degree ($T_{l,in} < T_{l,sat}$) when air concentrations are present, $w_{air} \approx 20.5\%$. The working conditions for this test are: $c_{l,in} \approx 60.15\%$, $Re \approx 78.25$, $P_t = 1300$, $T_{c,in} = 29.93°C$, $\dot{m}_c = 0.1199\ kg \cdot s^{-1}$.

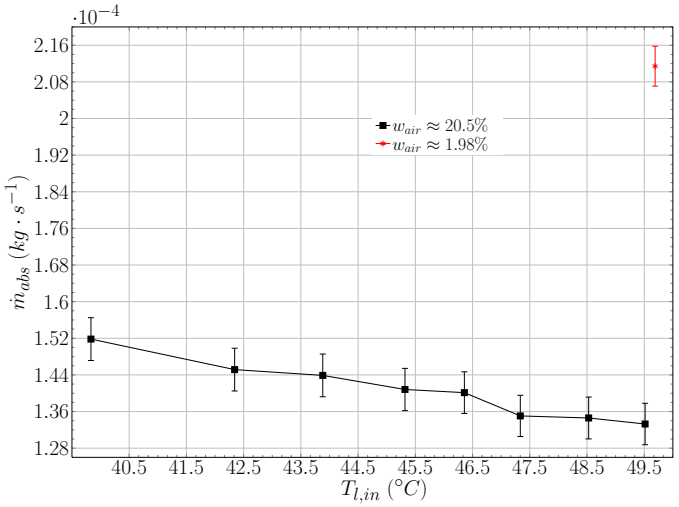

Figure 7.30: Experimental results of the mass absorbed ($\dot{m}_{abs}$) at different inlet solution temperature ($T_{l,in}$) and under the influence of air concentrations at $w_{air} \approx 20.5\%$

The Fig. 7.30 represents the experimental results for the mass absorbed ($\dot{m}_{abs}$), at different inlet solution temperature ($T_{l,in}$) and under the influence of non-absorbable gases when air concentration is about $w_{air} \approx 20.5\%$. The red dot represents the mass absorbed when the value of air concentration is about $w_{air} \approx 1.98\%$ and when the inlet solution temperature is about $T_{l,in} \approx T_{l,sat}$. At the same inlet solution temperature but with an air concentration about $w_{air} \approx 20.5\%$ the reduction in the mass absorbed

rate is about 36.9%. The mass absorbed present a maximum improvement of 13.9% as the subcooling degree increases from $T_{l,in} \approx 49.5$ to $T_{l,in} \approx 30.7$.

The Fig. 7.31 presents both the heat load ($\dot{Q}_{abs,c}$) and the energy input through the interface ($\dot{Q}_{abs,v}$), at different inlet solution temperature ($T_{l,in}$) and under the influence of non-absorbable gases when air concentration is about $w_{air} \approx 20.5\%$. It also shows the reference when the value $w_{air} \approx 1.98\%$ and when the inlet solution temperature is about $T_{l,in} \approx T_{l,sat}$. At the same inlet solution temperature the reduction is about 22.5% for the heat load and 40.1% for the energy input through the interface. Moreover, energy input through the interface shows a maximum improvement of 22.9% as the subcooling degree increases from $T_{l,in} \approx 49.5$ to $T_{l,in} \approx 30.7$. The heat load behaves in the opposite way, this is normal since heat load is sensible heat and it decreases as inlet solution temperature decreases.

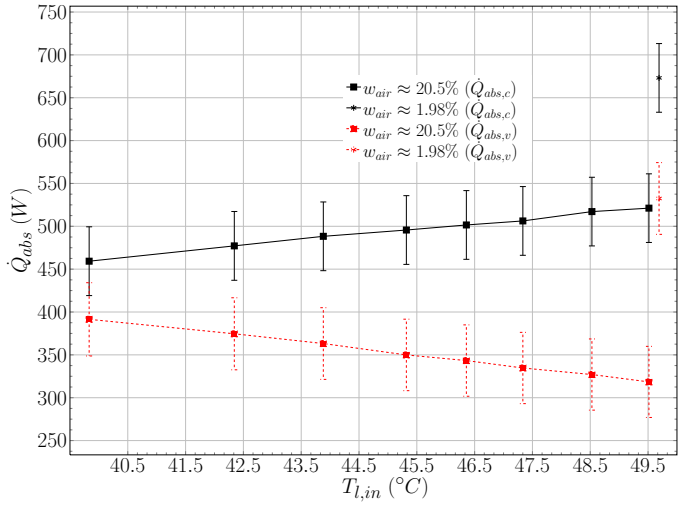

Figure 7.31: Experimental results of energy input through the interface ($\dot{Q}_{abs,v}$, red dots) and heat load ($\dot{Q}_c$, black dots) at different inlet solution temperature ($T_{l,in}$) and under the influence of air concentrations at $w_{air} \approx 20.5\%$

The augmentation of the absorption performance is due to the improvement of the pressure driving potential. The presence of air in the absorber reduces drastically the value of the partial pressure of H_2O in the interface ($P_{H_2O,if}$), therefore the pressure driving potential ($\Delta P_i = P_{H_2O,if} - P_{l,eq}(T_l, c_l)$) is also reduced. However when inlet solution temperature is greater than saturation temperature ($T_{l,in} < T_{l,sat}$) the value

of theoretical liquid solution pressure ($P_{l,eq}(T_l, c_l)$) (see the Fig. 2.3) is reduced, and then the value of ΔP_i increases.

7.2.4 Experimental Validation of the numerical model

In this section are compared the experimental data that were showed in section 7.2.2 against the numerical results of the mathematical model presented in chapter 6.

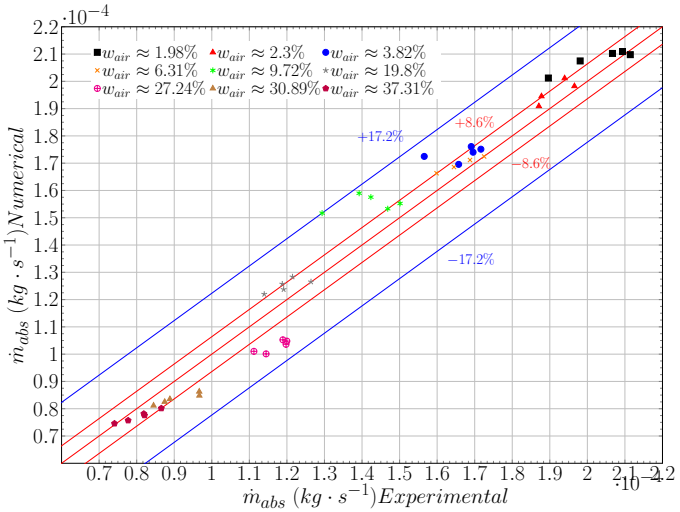

Figure 7.32: Comparison of the mass absorbed ($\dot{m}_{abs}$) between numerical and experimental results at different Re numbers ($Re = 85 \div 145$) and different air concentrations ($w_{air} = 1.98 \div 37.31\%$).

The Fig. 7.32 shows the comparison of the mass absorbed between numerical and experimental results at different Re numbers and different air concentrations ($w_{air} = 1.98 \div 37.31\%$) . The maximum error computed in uncertainty analysis is 8.6%. Most of the points are within the range of error. The experimental data compared against mathematical model shows the following errors: maximum error 17.2%, minimum error 3.71% and average error 5.69%.

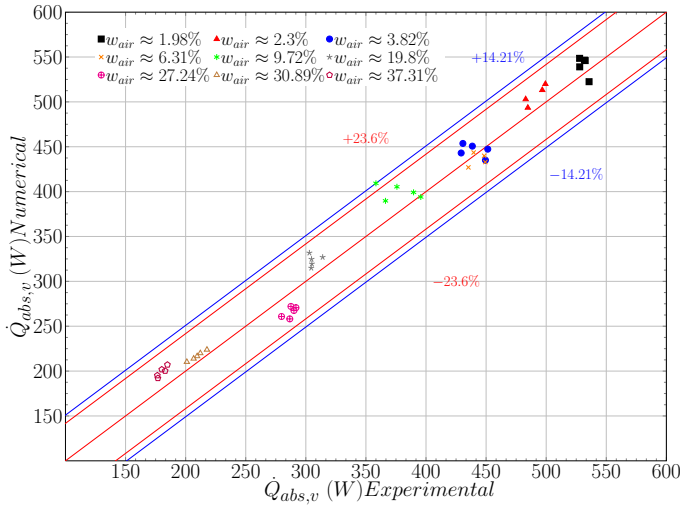

Figure 7.33: Comparison of the energy input through the interface ($\dot{Q}_{abs,v}$) between numerical and experimental results at different Re numbers ($Re = 85 \div 145$) and different air concentrations ($w_{air} = 1.98 \div 37.31\%$).

The Fig. 7.33 shows the comparison of the energy input through the interface ($\dot{Q}_{abs,v}$) between numerical and experimental results at different Re number and different air concentrations ($w_{air} = 1.98 \div 37.31\%$). The maximum error computed in uncertainty analysis 23.6%. The experimental data compared against the mathematical model shows the following errors: maximum error 14.21%, minimum error 0.41% and average error 5.07%. Notice that the maximum error of uncertainty analysis is higher than the maximum error between experimental and numerical results. This is because the low values of heat absorbed in at high air concentrations ($\dot{Q}_{abs,v} \approx 176\ W$ at $w_{air} = 37.32\%$). The uncertainty error associated to $\dot{Q}_{abs,v}$ keeps almost constant ($40.0 \div 42.4\ W$) but the error rate increases as $\dot{Q}_{abs,v}$ decreases.

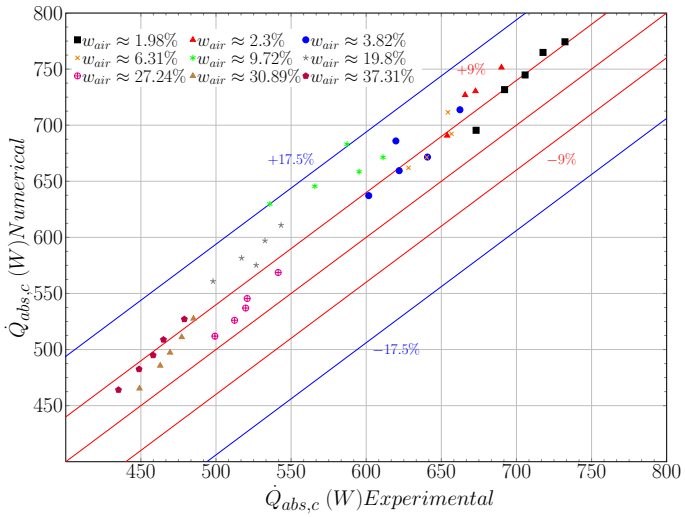

Figure 7.34: Comparison of the heat ($\dot{Q}_{abs,c}$) load between numerical and experimental results at different Re numbers ($Re = 85 \div 145$) and different air concentrations ($w_{air} = 1.98 \div 37.31\%$).

The Fig. 7.34 shows comparison of the heat load ($\dot{Q}_{abs,c}$) between numerical and experimental results at different Re numbers ($Re = 85 \div 145$) and different air concentrations ($w_{air} = 1.98 \div 37.31\%$). The maximum error computed in uncertainty analysis 9%. The experimental data compared against the mathematical model shows the following errors: maximum error 17.5%, minimum error 2.53% and average error 7.8%.

7.3 Conclusions

Along this chapter has been developed the experimental validation of two mathematical models: i) a semi-empirical, based on Navier Stokes equations together with energy and mass species simplified under the boundary layer hypotheses. Wavy profiles are implemented together with falling film formulation. In the mathematical model the Free Surface Deflection Equation is solved in each grid step for every Reynolds number. Presence of mist flow is considered by means of empirical information; ii) a second model which is an extension of the previous one. The same set of equations are implemented in the vapor side, wavy regime is also considered.

This chapter splits in two parts, here are enumerated the principal conclusions of each one:

1. Experimental validation of the falling film absorption in vertical tubes in presence of wavy regime (comparison against the smooth profile)

   (a) In the parametric study carried out has been discussed the variable evaluated. The influence of inlet mass solution, demonstrate that there is an Re number where the absorber performance is optimal ($Re \approx 100$), values either under or below results in a decrement of the absorber performance. The influence of $T_{l,in}$ is conditioned to the flow regime. For $Re < 140$ the subcooling has negative influence in the absorber, conversely subcooling degree seems to be a positive trending when $Re > 140$. From an academic perspective this is a topic of interest. However from the point of view of a technological aspect, typical configurations of absorption machines do not promote high differential values of subcooling.

   $T_{c,in}$ is an important factor in the performance of the absorber. The $T_{c,in}$ is directly proportional to the P_{abs} value. However, if $T_{c,in}$ decreases it is advantageous for the absorption rate as long as the value of P_{abs} is maintained. This only occurs if the heat source in the generator is augmented. Finally, the value of $c_{l,in}$ is directly proportional to the absorber performance.

   (b) The wavy model shows a better agreement than the smooth model against experimental results in mass transfer predictions. The smooth model underestimates the experimental values with a maximum error of 26%, on the other hand wavy model shows a better matching with an maximum error of 12%. In heat transfer predictions the performance of both models are comparable.

   (c) The mist flow is an phenomena that has been found during the experimental performance. It appears when $Re \geq 150$. The maximum value of mist flow is about $49PPM$. When $Re < 150$ the vapor is considered free of mist flow since its presence is less than $10PPM$

2. Experimental validation of the falling film absorption in vertical tubes in presence of wavy regime and presence of Non-absorbable gases

   (a) A set of experimental results at different Re number and different air mass concentrations w_{air} has been presented. A careful attention has been paid in order to obtain experimental results free of mist flow. The value of w_{air} is inversely proportional to the performance of the vertical absorber. The range of values of evaluation of are $w_{air} = 1.98\% - 37.31\%$. Where

the value $w_{air} = 1.98\%$ is the minimum value allowed in our experimental setup (see chapter 3.5). The maximum reduction in the heat and mass transfer rates of absorption are 66.06% and 59.40% respectively.

(b) An experimental study of the influence of the subcooling degree in presence of non-absorbable gases has been performed with an air concentration of $w_{air} \approx 20.5\%$. The reduction in the heat and mass transfer rates with the minimum allowable air concentration ($w_{air} \approx 1.98\%$) at saturation temperature are 36.94 and 40.11. When the subcooling degree is present there is an improvement in the heat and mass transfer rates with the maximum values of 22.9% and 13.9% respectively. In spite of the subcooling degree is advantageous for the absorption performance, it does not compensate the reduction caused by the air concentrations.

(c) An experimental validation of the mathematical model presented in chapter 6 has been performed. Numerical results considering laminar smooth model have been omitted. The experimental and numerical results show an acceptable agreement. The maximum, minimum and average errors are as follows: i) $\dot{m}_{abs}$, maximum error 17.2%, minimum error 3.71% and average error 5.69%; ii) $\dot{Q}_{abs,v}$, maximum error 14.21%, minimum error 0.41% and average error 5.07%; iii) $\dot{Q}_{abs,c}$, maximum error 17.50%, minimum error 2.53% and average error 7.80%.

(d) In spite of the discrepancies between numerical model and experimental results are acceptable, these numerical results have been considered as preliminaries. This is because of high values of the mass diffusivity in vapor mixture $air - H_2O$ (see section 6.2.2). It will be interesting to consider mass diffusion in streamwise direction in vapor side. It implies to add the term of second derivative of water concentration in flow direction, in the equation (6.11) and as a consequence, the dimensionless form applying the equation (B.14). In this way the set of equations become elliptic and the numerical resolution procedure has to be modified.

Nomenclature

c	concentration
$\dot{m}$	mass flow rate, $kg\ s^{-1}$
P	pressure, Pa
$\dot{Q}$	heat rate, W
T	temperature, K
w	vapor concentration
$y_{\delta c}$	distance from interface to the boundary layer concentration, m^{-1}

Greek symbols

δ_c	boundary layer concentration , m^{-1}
ρ	density, $m^3\ kg^{-1}$
ΔP	pressure driving potential, Pa
ΔC	concentration driving potential

Dimensionless Groups

Re	Reynolds falling film number, $Re = \frac{4\Gamma}{\mu}$

Subscripts

abs	absorption
air	air
b	bulk
c	coolant fluid
eq	equilibrium
H_2O	water
if	interface conditions
in	inlet conditions, inner
l	liquid phase in LiBr solution
out	outlet conditions, outer
sat	saturation
v	vapor phase
w	wall solid tube

Bibliography

[1] R. B. Bird, W. E. Stewart, and E. N. Lightfoot. *Fenómenos de Transporte.* REVERTÉ, 1973.

Chapter 8

General Conclusions and Future Work

ABSTRACT

The principal aspects and conclusions developed along this thesis are summarized in this chapter. In this work are presented both experimental and numerical studies. On the one hand, an experimental unit has been designed, built and started up. Experimental results have been obtained and discussed. On the other hand, numerical models has been developed with the objective of propose numerical tools for falling-film absorbers with special emphasis to air-cooled applications. Special attention has been paid to include into the models the consideration of both of wavy laminar regime profile of the falling film and the influence of non absorbable gases into the absorption performance. The influence of mist-flow in the vapor phase has been considered in the mathematical model by adding the corresponding empirical information. Experimental validation has been performed and discussed.

8.1 Conclusions

The main objectives of this thesis is double: On the one hand, provide quick calculation numerical tools for the design of air-cooled falling film vertical absorbers, and on the other hand, to develop an experimental infrastructure in order to validate such mathematical models. Special effort has been focused in obtain reliable experimental results that can be useful to validate not only the mathematical models proposed in this work, but also models proposed by other authors. The work of this thesis is distributed in three principal tasks: i) the experimental work: since the design of the experimental unit, going through the construction, start up, and verification of experimental results; ii) numerical work: development of the mathematical models,thermophysical properties, programing, etc.; iii) experimental comparison of the numerical results. The main conclusions are listed below.

8.1.1 Experimental work

In this thesis has been designed and built an experimental apparatus for reproducing absorption of H_2O vapor into falling film aqueous solution of $LiBr$ in vertical tubes. The experimental setup is oriented to obtain a wide range of data into different conditions. Those experimental data are useful tool for both the design of air-cooled vertical absorbers and the validation of mathematical models. In order to evaluate the presence of non-absorbale gases, an mass spectrometer for RGA has been set up and tested in order to assure high quality experimental data. The following conclusions during the experimental procedures are highlighted:

- An unexpected condition has been detected during the experimental performance, the presence of micro-droplets that are entrained by the water vapor during the generation process. The mist flow increases as Re number increases. We consider that the vapor mass flow is free of mist flow when $Re \leq 150$. In spite of the efforts to reduce such phenomena, it was not possible to obtain unpolluted water vapor from the generator. However, it has been possible to evaluate indirectly the quantity of mist-flow which leaks into the absorber in the form of global void fraction.

- The principal cause of mist flow generation is the way of heat is applied in the generator. In this experiment two ways have been used in order to apply the heat in the generator: i) a immersion electrical heater ($2kW$); ii) a set of flexible silicone rubber heaters placed directly on the outer surface of the generator with total capacity of $44kW$. It causes high heat fluxes per unit of area ($W \cdot m^{-2}$), and as a consequence high vapor velocities are provoked [2] and as a consequence a big amount of nucleated boiling is provoked. The high velocities in the vapor

conductions drags the drops produced and, consequently, this is the probably origin of the mist flow.

- An evaluation and start up of Mass Spectrometer for Residual Gas Analysis has been developed. The mass spectrometry is a tool that allows to evaluate the amount of air which absorber contains and its effect in absorption performance. The minimum allowed quantity of air in the absorber is $w_{air} \approx 1.98\%$ with an $P_t \approx 1300Pa$. A set of experimental results at different Re number and different mass concentrations w_{air} has been presented in order to evaluate the influence of non-absorbable gases in absorber's performance. Careful attention has been paid in order to obtain experimental results free of mist flow. The range of values of evaluation of are $c_a = 1.98\% - 37.31$. The maximum reduction in the heat and mass transfer rates of absorption are 66.06% and 59.40% respectively. In order to verify the reliability of the mass spectrometry data a second sensor was used. An optical sensor for dissolved oxygen (Hamilton ©) was used for this purpose. Thus the O_2 percentage can be evaluated by two different methods with good concordance.

8.1.2 Mathematical Formulation and Numerical Implementation

In chapter 4 a 1D-dimensional empirical model based in the resolution of ordinary differential equations is presented. This model solves temperature values for falling film (interfacial and bulk), wall solid and coolant fluid side, mass concentrations values (interfacial and bulk) and the heat and mass transfer rates in absorption phenomena. In chapter 5 a semi-empirical model based on Navier Stokes equations together with energy and mass species simplified under the boundary layer hypotheses is presented. The coupled equations are solved by means of finite difference method in a step by step procedure. Special attention have been paid in considering laminar wavy regime by including and solving the Free Surface Deflection Equation. The mathematical model has been adapted in order to consider the influence of mist flow described in chapter 3. Also the influence of Non-absorbable gases and its influence into the absorption phenomena has been modeled and in chapter 6, by applying the set of equations under boundary layer model in the vapor side. From this work, the following conclusions are addressed:

- The 1D-mathematical model has been used only for verification an comparison against boundary layer model, but this model has been omitted in the experimental validation. This because this mathematical model overpredicts the mass absorbed and the heat exchanged at high values of Re ($Re > 80$). This is mainly for the use of the empirical coefficients of heat and mass transfer.

- The boundary conditions of the mathematical model described in chapter 5 has been readapted in order to consider the influence of the mist flow.

- The same set of equations have been implemented in the vapor side. Special attention has been paid in the following aspects: i) detailed heat and mass transfer balances are applied at the interface to specify the boundary conditions between liquid and gas phases. The energy balance in the liquid-vapor interface based in $\dot{m}_{abs,v}$ is used as convergence criterion in the vapor side loop, and mass balance in the liquid vapor interface between both phases is used as convergence criterion in the liquid side loop; ii) the calculation of the mass diffusivity in the vapor side $D_{AB,v}$ at sub-atmospheric pressures is an important issue, since the value of $D_{AB,v}$ is inversely proportional to the value of P_t.

8.1.3 Validation of the Mathematical Models

The conclusions about the experimental validation of the numerical models are divided into two parts: i) Experimental validation of the mathematical model developed in chapter 4, where are focused mainly in the comparison between vertical falling film absorption with laminar wavy and smooth flow regimes; ii) experimental validation of the mathematical model developed in chapter 5, which includes the influence of non-absorbable gases in the absorption performance.

- A parametric study has been carried on in order to evaluate the principal working conditions that drives the absorption phenomena in vertical absorbers. The variables to be evaluated are:

  - The study of the influence of inlet mass flow solution demonstrate that there is an Re number where the absorber performance is optimal ($Re \approx 100$). The reason of that $Re > 100$ decreases the absorption performance is due to the reduction of the exposure time between liquid film and the gas phase. For instance, according with penetration theory [1, 4] the mass transfer coefficient is directly proportional to this exposure time. Numerical studies reproduces this condition, showing that driving potentials reduces when $Re > 100$.
  - As expected, the absorption pressure (P_{abs}) is the principal key of the absorption mechanisms. The more is the value of P_{abs}, the more is the and the better is the absorber performance. Experimental results show an improvement of up to 115% when the absorption pressure increases from $P_{abs} = 850$ Pa to $P_{abs} = 1300$ Pa. Both mathematical models (laminar smooth and laminar wavy) show same behavior.

- The influence of $T_{l,in}$ is conditioned to the flow regime. For $Re < 140$ the subcooling has negative influence in the absorber, conversely subcooling degree seems to be a positive trending when $Re > 140$. It shows an improvement of about 20% when the subcooling degree is about 5.6° C. The main conclusion is that subcooling degree in the inlet temperature is a secondary parameter in order to affect the absorber performance increment.
- As expected, coolant inlet temperature ($T_{c,in}$) is also an important factor in the performance of the absorber. The absorber performance shows an improvement: the heat and mass transfer rates 177% and 172% respectively, when the value of inlet coolant temperature decreases from $T_{c,in} \approx 42°C$ to $T_{c,in} \approx 30°C$.
- The mass fraction (c_{in}) affects favorably to the absorber performance. c_{in}. When c_{in} increases its value, the pressure driving potential increases. (see section 2.5). The absorption performance shows an improvement in the heat absorbed 25% and of mass transfer of 23%, when the value of inlet mass concentration increases from $c_{in} \approx 57.25\% wt$ to $c_{in} \approx 60.75\%$. Other aspect important to be highlighted is the fact that values higher than $c_{l,in} > 61\%$ causes crystallization problems.

- The laminar wavy model shows a better agreement than the laminar smooth model against experimental results in the mass transfer rates. Smooth model underestimates the experimental values with a maximum error of 25.4% in the case heat absorbed and 25.4%. On the other hand, wavy model shows a better matching with an maximum error of 11% in the case heat absorbed and 11.5% in the case of mass absorbed.

- An experimental study of the influence of the subcooling degree with presence of non-absorbable gases has been performed ($w_{air} \approx 20.5\%$). It is interesting to observe the positive influence of subcooling in the heat and mass transfer rates of the absorber. The reduction of the total heat ($\dot{Q}_{abs,v}$) and mass transfer rates ($\dot{m}_{abs}$) with the minimum allowable air concentration ($c_{air} \approx 1.98\%$) at saturation temperature are 36.9% for hand 40.1% respectively. When the subcooling degree is present there is an improvement in the heat and mass transfer rates with the maximum values of 22.9% and 13.9%, respectively. In spite of the subcooling degree is advantageous for the absorption performance, it does not compensate the reduction caused by the air concentrations.

- An experimental validation of the mathematical model presented in chapter 6 has been performed. Numerical results considering laminar smooth model have been omitted. The experimental and numerical results show an acceptable agreement. The maximum, minimum and average errors are as follows: i)

$\dot{m}_{abs}$, maximum error 17.12%, minimum error 3.71% and average error 5.04%; ii) $\dot{Q}_{abs,v}$, maximum error 14.21%, minimum error 0.41% and average error 5.07%; iii) $\dot{Q}_{abs,c}$, maximum error 7.50%, minimum error 2.53% and average error 7.80%.

8.1.4 Future Work

The future work is divided into the two mains lines of research.

8.1.5 Experimental

- A proposal for eradicating the mist flow involves the redesign of the generator. The main key lies in the quantity of heat per unit of area that is applied during the generation of the water vapor. According to [2] large heat fluxes lead with high vapor velocities, and this fact promotes the liquid aqueous solution entrainment. A falling film generator could be presented as a solution, since such configuration is the typical in a real absorption machine. An alternative solution would consist in a generator using a flooded finned-tube heat exchanger, operated by a secondary fluid as source of heat and endowed with an a recirculation system in order to avoid nucleation.

- An experimental unit free of mist flow would be useful for obtaining heat and mass transfer empirical correlations in a wide range of Re numbers, c_{in} and c_{air}. Such empirical information would be applied to the 1D-model.

8.1.6 Numerical

- The search and testing of new and improved empirical mass and heat transfer coefficients for vertical $LiBr - H_2O$ falling film absorbers for the 1D-model. In spite of the 1D-model has not been validated, it is still a useful tool for the prediction and design of vertical absorbers. This is due to mainly for the saving in CPU time that it offers.

- Inclusion of the diffusion term in the stream wise direction in the species conservation equation in vapor side. This mainly due to the high values of mass diffusivity in vapor side (see Fig. 6.6). It implies to add the second derivative term in x direction in equation (6.11), and as a consequence the dimensionless form applying equation (B.14). In this way the set of equations become elliptic and the step by step procedure has to be redefined.

- It will be useful to develop a multidimensional mathematical model (x, y, z) for the falling film for higher Re, advanced surfaces and surfactant. E.g. an

interesting proposal is given by Kalliadasis et al. [3], who developed a Three-Dimensional boundary layer equations for falling films in vertical plates. In order to consider wavy dynamics on a liquid film flow two boundary conditions are imposed in the free surface: i) kinematic boundary conditions; ii) stress balance in the interface. Other proposals based on Level Set methods, volume of fluid (VOF) method, moving boundaries, etc. could be other options to be explored in the future.

Bibliography

[1] R. B. Bird, W. E. Stewart, and E. N. Lightfoot. *Fenómenos de Transporte.* REVERTÉ, 1973.

[2] K. E. Herold, R. Radermacher, and S. A. Klein. *Absorption Chillers and Heat Pumps.* CRC Press, 1996.

[3] S. Kalliadasis, C. Ruyer-Quil, B. Scheid, and M. G. Velarde. *Falling Liquid Films.* Springer, 2012.

[4] J. R. Welty, C. E. Wicks, R. E. Wilson, and G. L. Rorrer. *Fundamentals of momentum, Heat and Mass Transfer.* Willey, 2008.

Appendices

Appendix A

1D Dimensional Empirical Model Deductions

A.1 Formulation of the Heat and Mass Balance

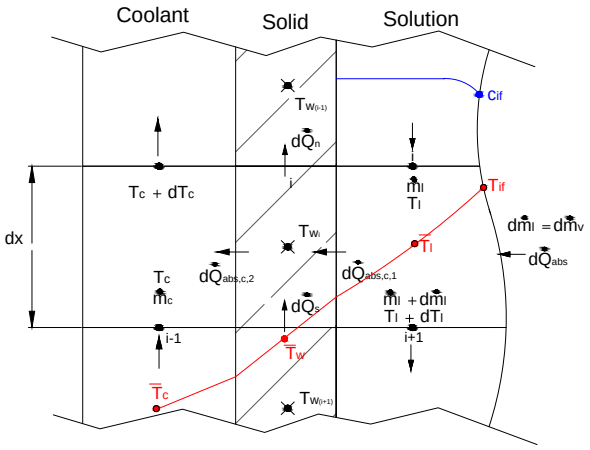

Figure A.1: Schematic control volume of the liquid film, solid and coolant domains. Typical temperature profiles

The mathematical model is similar of that one proposed by Patnaik [1] and Patnaik et al. [2], but with the difference that axial conduction heat is considered in wall tube. The formulation is based on two energy balances, and a mass balance on an

infinitesimally thin slice of the absorber tube, as illustrated in Fig. A.1.

We first consider balance into liquid solution, which yields as follows:

$$- d\dot{Q}_{abs,c,1} + \dot{m}_l c_{pl} T_l - (\dot{m}_l + d\dot{m}_l) c_{pl} (T_l + dT_l) + d\dot{m}_l h_v = 0 \tag{A.1}$$

Developing and rearranging:

$$-d\dot{Q}_{abs,c,1} = -c_{pl} dT_l (\dot{m}_l + d\dot{m}_l) + d\dot{m}_l (h_v - c_{pl} T_l) \tag{A.2}$$

The heat load ($d\dot{Q}_{abs,c,1}$) can be calculated as convection heat between the wall and the solution:

$$d\dot{Q}_{abs,c,1} \approx \alpha_l (T_l - T_w) dA_{out} \tag{A.3}$$

replacing in balance equation and rearranging:

$$-c_{pl}\ dT_l\ (\dot{m}_l + d\dot{m}_l) = -d\dot{m}_l (h_v - c_{pl} T_s) + \alpha_l (T_l - T_w) dA_{out} \tag{A.4}$$

The differential area is defined as, $dA_{out} = \pi d_{out} dx$, the dimensionless form of the variables is obtained by using coolant outlet properties, $(\dot{m}_c, c_{pc}, T_{c,out})$ as follows:

$$T^* = \frac{T}{T_{c,out}}, \qquad \dot{m}^* = \frac{\dot{m}}{\dot{m}_c}, \qquad c_p^* = \frac{c_p}{c_{pc}}$$
$$dx^* = \frac{dx}{L}, \qquad \alpha* = \frac{\alpha\ A}{\dot{m}_c c_{pc}}, \qquad h_v^* = \frac{h_v}{T_{c,out} c_{pc}}$$

introducing the above variables we obtain:

$$\frac{-c_{pl}\ dT_l\ (\dot{m}_l + d\dot{m}_l)}{\dot{m}_c c_{pc} T_{c,out}} = -\frac{d\dot{m}_l(h_v - c_{pl}T_s)}{\dot{m}_c c_{pc} T_{c,out}} + \frac{\alpha_l(T_l - T_w)\pi d_{out}dx}{\dot{m}_c c_{pc} T_{c,out}}\frac{L}{L}$$

$$-c^*_{pl}\ dT^*_l\ (\dot{m}^*_l + d\dot{m}^*_l) = -d\dot{m}^*_l(h^*_v - c^*_{pl}T^*_l) + \alpha^*(T^*_l - T^*_w)\ dx^* \tag{A.5}$$

The final equation is obtained considering $(\dot{m}_l + d\dot{m}_l) = \dot{m}_l$ due to that $d\dot{m}_l$ is smaller in order of magnitude compared with $\dot{m}_l$, and introducing heat capacity $M^*_l = c^*_{p,l}\dot{m}^*_l$ then:

$$\frac{dT^*_l}{dx^*} = \frac{1}{M^*_l}\left[-\frac{d\dot{m}^*_l}{dx^*}(h^*_v - c^*_{p_l}T^*_l) + \alpha^*_l(T^*_l - T^*_w)\right] \tag{A.6}$$

A second energy balance is considered in coolant fluid side:

$$d\dot{Q}_{abs,c,2} - \dot{m}_c c_{pc} T_c + \dot{m}_c c_{pc}(T_c + dT_c) = 0 \tag{A.7}$$

The convection heat in coolant fluid side is considered by:

$$d\dot{Q}_{abs,c,2} \approx \alpha_c(T_c - T_w)dA_{in} \tag{A.8}$$

replacing the previous equation in coolant energy balance and setting $dA_{in} = \pi d_{in}dx$ it yields:

$$\dot{m}_c c_{pc} dT_c = -\alpha_c(T_c - T_w)\pi d_{in}dx \tag{A.9}$$

Analogously the dimensionless form is obtained by reducing by means of outlet coolant variables.

$$\frac{\dot{m}_c c_{p_c} dT_c}{\dot{m}_c c_{pc} T_{c,out}} = -\frac{-\alpha_c(T_c - T_w)\pi d_{in}dx}{\dot{m}_c c_{pc} T_{c,out}} \cdot \frac{L}{L} \tag{A.10}$$

$$\frac{dT_c^*}{dx^*} = -\alpha_c^*(T_c^* - T_w^*) \tag{A.11}$$

Finally, a mass balance is considered in order to obtain the third differential equation:

$$d\dot{m}_l = d\dot{m}_v \tag{A.12}$$

As mentioned in chapter 2, both convective mass and heat transfer are analogous. Therefore forced and natural convection are distinguished. Taking up the equation (2.26) it yields in,

$$d\dot{m}_l \approx \kappa_l \rho_l (c_l - c_{if}) dA_{out} \tag{A.13}$$

Then if Sherwood number is introduced into mass balance equation it yields.

$$d\dot{m}_l = \frac{ShD_l}{\delta} \rho_l (c_l - c_{if}) 2\pi r_{out} dx$$

Introducing the corresponding variables to make the equation non dimensional we obtain,

$$\frac{d\dot{m}_l}{\dot{m}_c} = \frac{ShD_l}{\delta \dot{m}_c} \rho_l (c_l - c_{if}) 2\pi r_{out} dx \cdot \frac{L}{L} \tag{A.14}$$

$$\frac{d\dot{m}_l^*}{dx^*} = \frac{2\pi r_{out} L}{\dot{m}_c} \frac{ShD_l}{\delta} \rho_l (c_l - c_{if}) \tag{A.15}$$

The equations (A.6), (A.11) and (A.15) are three ordinary differential equations, if they are solved, liquid solution and coolant temperatures fields are obtained as well as

mass absorbed. In order to close the set of equations, an energy balance is performed in the liquid-vapor interface.

$$-\lambda_l \left(\frac{\partial T}{\partial y}\right) dA_{if} = d\dot{m}_l h_{abs} \tag{A.16}$$

Assuming linear profile between bulk and interface temperatures,

$$-\lambda_l \left(\frac{\partial T}{\partial y}\right) \approx -\lambda_l \left(\frac{T_{if} - T_l}{\delta/2}\right) \tag{A.17}$$

in the differential area the film thickness is taken into account,

$$dA_{if} = \pi(2r_{out} + 2\delta)dx \tag{A.18}$$

replacing ,

$$-\lambda_l \left(\frac{T_{if} - T_l}{\delta/2}\right) \pi(2r_{out} + 2\delta)dx = d\dot{m}_l h_{abs} \tag{A.19}$$

rearranging and converting into the dimensionless form,

$$\frac{\lambda_l}{\delta/2} \left(\frac{T_{if} - T_l}{T_{c,out}}\right) L\pi(2r_{out} + 2\delta)\frac{dx}{L} = \frac{d\dot{m}_l}{\dot{m}_c} \quad \frac{h_{abs}}{c_{pc}T_c} \quad \dot{m}_c c_{pc} \tag{A.20}$$

$$\frac{\lambda_l}{\delta/2} \quad (T^*_{if} - T^*_l)L\pi(2r_{out} + 2\delta)dx^* = d\dot{m}^*_l h^*_{abs} M_c \tag{A.21}$$

finally, the interface temperature is calculated by the following expression,

$$T^*_{if} \quad = \quad T^*_l + \frac{h^*_{abs} M_c}{\pi L \lambda} \quad \frac{\delta}{4(r_{out} + \delta)} \quad \frac{d\dot{m}^*_l}{dx^*} \tag{A.22}$$

It is interesting to remark the difference between the term h_v of equation (A.6) and the term h_{abs} of equation (A.22). The first term refers to the enthalpy vapor, it appears when a global energy balance is performed in the control volume. The second term is heat of absorption that is function of both temperature and concentration $h_{abs} = f(T_{if}, c_{if})$ it has to be applied when an energy balance is performed at the liquid-vapor interface.

Nomenclature

A	area, m^2
c_p	specific heat capacity, $J\ kg^{-1}\ K^{-1}$
c	$LiBr$ mass fraction concentration
D	mass diffusivity,$m^2\ s^{-1}$
d	tube diameter, m
h	specific enthalpy, $J\ kg^{-1}$
L	tube length, m
M	heat capacity, $W\ K^{-1}$
$\dot{m}$	mass flow, $kg\ s^{-1}$
$\dot{Q}$	heat rate, W
r	tube radius, m
T	temperature, K
x	coordinate, m
y	coordinate, m

Greek symbols

α	heat transfer coefficient, $W\ m^{-2}\ K^{-1}$
δ	film thickness, m
κ	mass transfer coefficient $m\ s^{-1}$
λ	thermal conductivity, $W\ m^{-1}\ K^{-1}$
ρ	density, $kg\ m^{-3}$

Dimensionless Groups

Sh	Sherwood Number, $Sh = \frac{\kappa\delta}{D}$

Subscripts

abs	absorption

c	coolant fluid
if	interface conditions
in	inlet conditions, inner
l	liquid phase in LiBr solution
out	outlet conditions, outer
v	vapor phase
w	wall solid tube

Superscripts

$*$	dimensionless quantity

Bibliography

[1] V. Patnaik. *Combined Heat and Mass Transfer in Wavy-Film Absorption.* PhD thesis, Pennsylvania State University, 1994.

[2] V. Patnaik, H. Pérez-Blanco, and W. A. Ryan. A Simple Analytical Model for the Design of Vertical Tube Absorbers. *ASHRAE Transactions*, 99(2):69–80, 1993.

Appendix B

Boundary Layer Model Dimensionless Governing Equations

B.1 Brief Description of the Boundary Layer Equations

The concept of Boundary Layer was first introduced by Ludwig Prandtl in 1904. He made a simplification of the conservation equations by estimating the order of magnitude of the various terms. The concept of boundary layer is defined as the zone (very thin layer) where there are gradients of velocity (the transition from zero velocity at the solid surface to the full magnitude). In the literature there are many authors which offer a detailed description of the Prandtl's analysis [1–3].

The mass and momentum conservation equations under boundary layer hypotheses for unsteady state and constant physical properties are:

$$\frac{\partial u}{\partial x} + \frac{\partial v}{\partial y} = 0 \tag{B.1}$$

$$\frac{\partial u}{\partial t} + u\frac{\partial u}{\partial x} + v\frac{\partial u}{\partial y} = -\frac{1}{\rho}\frac{\partial P}{\partial x} + \nu\frac{\partial^2 u}{\partial y^2} + g_x \tag{B.2}$$

Analogously, the energy and mass species conservation equations under boundary layer hypotheses are as follows,

$$\frac{\partial T}{\partial t} + u\frac{\partial T}{\partial x} + v\frac{\partial T}{\partial x} = -\frac{1}{\rho}\frac{\partial P}{\partial x} + a\frac{\partial^2 T}{\partial y^2} \tag{B.3}$$

$$\frac{\partial c}{\partial t} + u\frac{\partial c}{\partial x} + v\frac{\partial c}{\partial x} = -\frac{1}{\rho}\frac{\partial P}{\partial x} + D\frac{\partial^2 c}{\partial y^2} \tag{B.4}$$

One of the hypothesis assumed in the absorption mathematical model assumes constant vapor pressure inside the absorber and there are not pressure drops in vapor side. Since the pressure in the vapor-liquid interface is established by the vapor pressure, then:

$$-\frac{1}{\rho}\frac{\partial P}{\partial x} = 0 \tag{B.5}$$

Finally, assuming steady state and introducing hypotheses (B.5) in above equations we obtain,

$$\frac{\partial u}{\partial x} + \frac{\partial v}{\partial x} = 0 \tag{B.6}$$

$$u\frac{\partial u}{\partial x} + v\frac{\partial u}{\partial y} = \nu\frac{\partial^2 u}{\partial y^2} + g_x \tag{B.7}$$

$$u\frac{\partial T}{\partial x} + v\frac{\partial T}{\partial x} = a\frac{\partial^2 T}{\partial y^2} \tag{B.8}$$

$$u\frac{\partial c}{\partial x} + v\frac{\partial c}{\partial x} = D\frac{\partial^2 c}{\partial y^2} \tag{B.9}$$

B.2 Chain Rule for Partial Derivatives

The Navier Stokes equations, energy and mass species conservations equations under boundary layer hypothesis are transformed into dimensionless form. We will transform the variables in physical space (x, y) to a transformed space (ξ, ζ) where,

$$\xi = \xi(x,y) = \frac{x}{L} \tag{B.10}$$

$$\zeta = \zeta(x,y) = \frac{y}{\delta(x)} \tag{B.11}$$

Therefore, if the chain rule for the differential calculus is applied, we have,

$$\frac{\partial}{\partial x} = \xi_x \frac{\partial}{\partial \xi} + \zeta_x \frac{\partial}{\partial \zeta} \tag{B.12}$$

$$\frac{\partial}{\partial y} = \xi_y \frac{\partial}{\partial \xi} + \zeta_y \frac{\partial}{\partial \zeta} \tag{B.13}$$

$$\frac{\partial^2}{\partial y^2} = \xi_y^2 \frac{\partial^2}{\partial \xi^2} + \xi_{yy} \frac{\partial}{\partial \xi} + 2\xi_y \zeta_y \frac{\partial^2}{\partial \xi \partial \zeta} + \zeta_{yy} \frac{\partial}{\partial \zeta} + \zeta_y^2 \frac{\partial^2}{\partial \zeta^2} \tag{B.14}$$

where,

$$\xi_x = \frac{\partial \xi}{\partial x} = \frac{1}{L} \tag{B.15}$$

$$\xi_y = \frac{\partial \xi}{\partial y} = 0 \tag{B.16}$$

$$\zeta_x = \frac{\partial \zeta}{\partial x} = -\frac{y}{\delta^2} \frac{d\delta}{dx} \tag{B.17}$$

$$\zeta_y = \frac{\partial \zeta}{\partial y} = \frac{1}{\delta} \tag{B.18}$$

$$\xi_{yy} = \zeta_{yy} = 0 \tag{B.19}$$

Then replacing the equations (B.16)- (B.19) into (B.21) - (B.22) yields,

$$\frac{\partial}{\partial x} = \frac{1}{L} \frac{\partial}{\partial \xi} - \frac{y}{\delta^2} \frac{d\delta}{dx} \frac{\partial}{\partial \zeta} \tag{B.20}$$

$$\frac{\partial}{\partial y} = \frac{1}{\delta} \frac{\partial}{\partial \zeta} \tag{B.21}$$

$$\frac{\partial^2}{\partial y^2} = \frac{1}{\delta^2} \frac{\partial^2}{\partial \zeta^2} \tag{B.22}$$

The above equations contains terms that depicts the second partial derivative with respect to x in terms of first, second and mixed derivatives with respect to ζ and ξ, multiplied by various metric terms. The fully detailed deduction of such expressions can be consulted in [2].

B.3 Mass Conservation Equation in curvilinear coordinates

The equation (B.23) refers to bidimensional mass conservation equation for incompressible fluid.

$$\frac{\partial u}{\partial x} + \frac{\partial v}{\partial y} = 0 \tag{B.23}$$

replacing the equations (B.21) and (B.22) into the equation (B.23) it yields,

$$\left(\frac{1}{L}\frac{\partial u}{\partial \xi} - \frac{y}{\delta^2}\frac{d\delta}{dx}\frac{\partial u}{\partial \zeta}\right) + \frac{1}{\delta}\frac{\partial v}{\partial \zeta} = 0 \tag{B.24}$$

introducing the following terms, $\beta_1 = \frac{x}{\delta}\frac{d\delta}{dx}$ and $\epsilon = \frac{x}{\delta}$

$$\left(\frac{1}{L}\frac{\partial u}{\partial \xi} - \frac{y}{\delta^2}\frac{\beta_1}{\epsilon}\frac{\partial u}{\partial \zeta}\right) + \frac{\epsilon}{\xi L}\frac{\partial v}{\partial \zeta} = 0 \tag{B.25}$$

$$\left(\frac{\xi}{x}\frac{\partial u}{\partial \xi} - \frac{y}{\delta}\frac{\beta_1}{\epsilon\delta}\frac{\partial u}{\partial \zeta}\right) + \frac{\epsilon}{\xi}\frac{\xi}{x}\frac{\partial v}{\partial \zeta} = 0 \tag{B.26}$$

$$\left(\frac{\xi}{x}\frac{\partial u}{\partial \xi} - \zeta\frac{\beta_1}{x}\frac{\partial u}{\partial \zeta}\right) + \frac{\epsilon}{x}\frac{\partial v}{\partial \zeta} = 0 \tag{B.27}$$

finally, multiplying the equations (B.26)-(B.27) by x,

$$\xi\frac{\partial u}{\partial \xi} - \zeta\beta_1\frac{\partial u}{\partial \zeta} + \epsilon\frac{\partial v}{\partial \zeta} = 0 \tag{B.28}$$

B.4 Momentum Conservation Equation in curvilinear coordinates

The equation (B.29) refers to bidimensional momentum conservation equation for an incompressible fluid and constant physical properties,

$$u\frac{\partial u}{\partial x} + v\frac{\partial u}{\partial y} = gcos(\theta) + \nu\frac{\partial^2 u}{\partial y^2} \tag{B.29}$$

placing the terms (B.21) -(B.22) in the above equation yields the following expression,

$$u\left(\frac{1}{L}\frac{\partial u}{\partial \xi} - \frac{y}{\delta^2}\frac{d\delta}{dx}\frac{\partial u}{\partial \zeta}\right) + \frac{v}{\delta}\frac{\partial u}{\partial \zeta} = gcos(\theta) + \frac{\nu}{\delta^2}\frac{\partial^2 u}{\partial \zeta^2} \tag{B.30}$$

developing and rearranging terms,

$$\frac{u}{L}\frac{\partial u}{\partial \xi} - \frac{yu}{\delta^2}\frac{d\delta}{dx}\frac{\partial u}{\partial \zeta} + \frac{v}{\delta}\frac{\partial u}{\partial \zeta} = gcos(\theta) + \frac{\nu}{\delta^2}\frac{\partial^2 u}{\partial \zeta^2} \tag{B.31}$$

introducing ϵ, β_1 and $\frac{d\delta}{dx} = \frac{\xi}{x}\frac{d\delta}{d\xi}$,

$$u\frac{\xi}{x}\frac{\partial u}{\partial \xi} - \frac{\zeta u}{\delta}\frac{\xi}{x}\frac{\delta\beta_1}{\xi}\frac{\partial u}{\partial \zeta} + v\frac{\epsilon}{x}\frac{\partial u}{\partial \zeta} = gcos(\theta) + \frac{\nu}{\delta^2}\frac{\partial^2 u}{\partial \zeta^2} \tag{B.32}$$

finally, multiplying by x the equation (B.32) and introducing $\beta_2 = xgcos(\theta) = gL\xi cos(\theta)$, $\beta_3 = \frac{x}{\delta^2} = \frac{\xi L}{\delta^2}$

$$u\xi\frac{\partial u}{\partial \xi} - \zeta u\beta_1\frac{\partial u}{\partial \zeta} + v\epsilon\frac{\partial u}{\partial \zeta} = x \cdot gcos(\theta) + \frac{x}{\delta^2}\nu\frac{\partial^2 u}{\partial \zeta^2} \tag{B.33}$$

$$u\xi\frac{\partial u}{\partial \xi} - \zeta u\beta_1\frac{\partial u}{\partial \zeta} + v\epsilon\frac{\partial u}{\partial \zeta} = \beta_2 + \beta_3\nu\frac{\partial^2 u}{\partial \zeta^2} \tag{B.34}$$

B.5 Energy Conservation Equation in curvilinear coordinates

The equation (B.35) refers to bidimensional energy conservation equation for incompressible fluid and constant physical properties,

$$u\frac{\partial T}{\partial x} + v\frac{\partial T}{\partial y} = a\frac{\partial^2 T}{\partial y^2} \tag{B.35}$$

placing the terms (B.21) -(B.22) in the above equation yields the following expression,

$$u\left(\frac{1}{L}\frac{\partial T}{\partial \xi} - \frac{y}{\delta^2}\frac{d\delta}{dx}\frac{\partial T}{\partial \zeta}\right) + \frac{v}{\delta}\frac{\partial T}{\partial \zeta} = \frac{a}{\delta^2}\frac{\partial^2 T}{\partial \zeta^2} \tag{B.36}$$

introducing terms, developing and rearranging the following expressions it yields,

$$\frac{\partial T}{\partial \xi} = \left(\frac{\zeta}{\delta}\frac{\partial \delta}{\partial \xi} - \frac{v}{u}\frac{L}{\delta}\right)\frac{\partial T}{\partial \zeta} + \frac{a}{u}\frac{L}{\delta^2}\frac{\partial^2 T}{\partial \zeta^2} \tag{B.37}$$

B.6 Mass Species Conservation Equation

The equation (B.38) refers to bidimensional mass species conservation equation for incompressible fluid and constant physical properties,

$$u\frac{\partial c}{\partial x} + v\frac{\partial c}{\partial y} = D\frac{\partial^2 c}{\partial y^2} \tag{B.38}$$

Since the equations (B.38) and (B.35) are analogous the final form of the species equation yields,

$$\frac{\partial c}{\partial \xi} = \left(\frac{\zeta}{\delta} \frac{\partial \delta}{\partial \xi} - \frac{v}{u} \frac{L}{\delta} \right) \frac{\partial c}{\partial \zeta} + \frac{D}{u} \frac{L}{\delta^2} \frac{\partial^2 c}{\partial \zeta^2} \tag{B.39}$$

Nomenclature

a	thermal diffusivity, $m^2\ s^{-1}$
c	$LiBr$ mass fraction concentration
D	mass diffusivity, $m^2\ s^{-1}$
g	acceleration due to gravity, $m\ s^{-2}$
L	tube lenght, m
P	pressure, Pa
T	temperature, K
t	time, s
u	velocity profile x axis direction, $m\ s^{-1}$
v	velocity profile y axis direction, $m\ s^{-1}$
x	coordinate, m
y	coordinate, m

Greek symbols

δ	film thickness, m
ξ	dimensionless x coordinate
ζ	dimensionless y coordinate
θ	inclination angle, rad
ν	kinematic viscosity $m^2\ s^{-1}$
ρ	density, $kg\ m^{-3}$

Bibliography

[1] E. R. G. Eckert and R. M. Drake Jr. *Analysis of Heat and Mass Transfer*. McGraw-Hill, 1972.

[2] J. F. Wendt. *Computational Fluid Dynamics. An Introduction.* Springer, 2008.

[3] J.H. Ferziger and M. Peric. *Computational methods for fluid dynamics*. Springer-Berlag, 1996.

Appendix C

Mass Absorption in Presence of Mist Flow

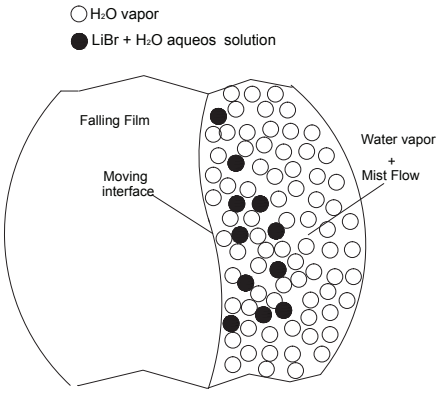

Figure C.1: Schematic description of mist flow in the liquid-vapor interface.

The Fig. (C.1) depicts the liquid-vapor interface between the liquid film and the vapor water in presence of mist flow. The total mass that cross the interface is given by,

$$\dot{m}_t = \dot{m}_{abs,v} + \dot{m}_{abs,l} \tag{C.1}$$

Since our interest is to evaluate the vapor water that is absorbed, it is more useful to evaluate the total mass of H_2O that is entering into the film,

$$\dot{m}_{abs_{H_2O,t}} = \dot{m}_{abs,v} + \dot{m}_{abs_{H_2O,l}} \tag{C.2}$$

The second term of the left side of the above equation represents the portion of water in the mist flow,

$$\dot{m}_{abs_{H_2O,l}} = \dot{m}_{abs,l}(1 - c_{l,in}) \tag{C.3}$$

where the concentration of mist flow is assumed to be the same as inlet concentration since the aqueous solution in the generator is homogeneous. In order to close the set equations an extra equation is still needed.

$$\dot{m}_{abs_{H_2O,t}} = c_{H_2O_{if}}(\dot{m}_{abs_{H_2O,t}} + \dot{m}_{abs_{LiBr,l}}) - D_l\rho_l\nabla c_{H_2O} \cdot \vec{n} \tag{C.4}$$

The above equation represents the Fick's law for two inmiscible moving fluids, the term $\dot{m}_{abs_{LiBr,l}}$ represents the portion of $LiBr$ contained in mist flow, such term can also be expressed as,

$$\dot{m}_{abs_{LiBr,l}} = \dot{m}_{abs,l}c_{l,in} \tag{C.5}$$

replacing the equation (C.5) into the equation (C.6) yields,

$$\dot{m}_{abs_{H_2O,t}} = c_{H_2O_{if}}(\dot{m}_{abs_{H_2O,t}} + \dot{m}_{abs,l}c_{in}) - D_l\rho_l\nabla c_{H_2O} \cdot \vec{n} \tag{C.6}$$

developing and regrouping,

$$\dot{m}_{abs_{H_2O,t}} = \frac{c_{H_2O_{if}}}{(1 - c_{H_2O_{if}})}\dot{m}_{abs,l}c_{l,in} - \frac{D_l\rho_l}{(1 - c_{H_2O_{if}})}\nabla c_{H_2O} \cdot \vec{n} \tag{C.7}$$

the equation (C.7) can also be expressed in terms of the $LiBr$ concentration since $c_{H_2O} = 1 - c$,

$$\dot{m}_{abs_{H_2O,t}} = \frac{(1 - c_{l,if})\dot{m}_{abs,l}c_{l,in}}{c_{l,if}} + \frac{D_l\rho_l}{c_{l,if}}\nabla c \cdot \vec{n} \tag{C.8}$$

The equations (C.2), (C.3) and (C.8) are solved simultaneously in order to evaluate the mass fluxes that enters in the liquid-vapor interface.

Nomenclature

c	$LiBr$ mass fraction concentration
D	mass diffusivity, $m^2\ s^{-1}$
$\dot{m}$	mass flow rate, $kg\ s^{-1}$
$\vec{n}$	outward directed unit normal vector, m
T	temperature, K

Greek symbols

ρ	density, $kg\ m^{-3}$

Subscripts

abs	absorption
H_2O	referent to the water component in aqueous solution
if	interface conditions
in	inlet conditions
l	liquid phase in LiBr solution
$LiBr$	referent to the LiBr component in aqueous solution
$LiBr$	referent to the LiBr component in aqueous solution
v	vapor
t	total